
Article:
Eveson, Simon Patrick orcid.org/0000-0002-1911-6113, Dudley Ward, Nicholas and Lähivaara, Timo (2017) A discontinuous Galerkin method for poroelastic wave propagation : the two-dimensional case. Journal of Computational Physics. pp. 690-727. ISSN 0021-9991

https://doi.org/10.1016/j.jcp.2017.08.070

Accepted Manuscript

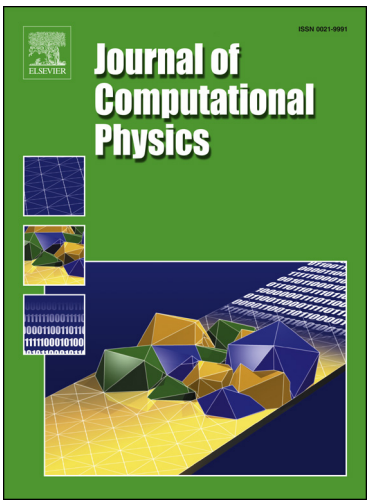

A discontinuous Galerkin method for poroelastic wave propagation I: the two-dimensional case

N.F. Dudley Ward, T. Lähivaara, S. Eveson

PII: S0021-9991(17)30658-7
DOI: http://dx.doi.org/10.1016/j.jcp.2017.08.070
Reference: YJCPH 7579

To appear in: *Journal of Computational Physics*

Received date: 25 January 2017
Revised date: 25 July 2017
Accepted date: 31 August 2017

Please cite this article in press as: N.F. Dudley Ward et al., A discontinuous Galerkin method for poroelastic wave propagation I: the two-dimensional case, *J. Comput. Phys.* (2017), http://dx.doi.org/10.1016/j.jcp.2017.08.070

A discontinuous Galerkin method for poroelastic wave propagation I: the two-dimensional case

N.F. Dudley Ward[a,*], T. Lähivaara[b], S. Eveson[c]

[a] *Department of Civil and Natural Resources Engineering, University of Canterbury, Christchurch, New Zealand*
[b] *Department of Applied Physics, University of Eastern Finland, Kuopio, Finland*
[c] *Department of Mathematics, University of York, York, United Kingdom*

Abstract

In this paper, we consider a high-order discontinuous Galerkin (DG) method for modelling wave propagation in coupled poroelastic-elastic media. The upwind numerical flux is derived as an exact solution for the Riemann problem including the poroelastic-elastic interface. Attenuation mechanisms in both Biot's low- and high-frequency regimes are considered. The current implementation supports non-uniform basis orders which can be used to control the numerical accuracy element by element. In the numerical examples, we study the convergence properties of the proposed DG scheme and provide experiments where the numerical accuracy of the scheme under consideration is compared to analytic and other numerical solutions.

Keywords: Discontinuous Galerkin method, Non-uniform basis order, Poroelastic waves

1. Introduction

The current work has grown out of the authors' interest in using ground motions to quantify aquifer features of interest. The motivation comes from groundwater engineering where (in the authors' experience) it is very often the case that detailed subterranean knowledge is lacking. We mention Canterbury, New Zealand, where, as well as supplying the province's capital city of 400,000, groundwater accounts for around 30% of the irrigation water. A naive picture of large and vaguely spatially homogeneous and isotropic aquifers is far from the truth [1]: collective drilling experience over many years suggests a more complicated network of subterranean flow paths, [2]. Conventional groundwater engineering is based on drilling and pumping tests to estimate potential yield and the rate at which water can be abstracted. Apart from cost considerations, interpreting pump test data will, at best, reveal only local information about an aquifer's state, [3, 4]. This motivates our interest in non-invasive subsurface imaging, where the intention is to build a more comprehensive map of an aquifer and its physical features. The impetus for our work arose from the Canterbury/Christchurch earthquakes of 2010-11 [5, 6], when lack of sufficiently resolved knowledge about the groundwater system became particularly poignant.

*Corresponding author
Email address: nick.dudleyward@canterbury.ac.nz (N.F. Dudley Ward)

Inverting ground motion data to reveal aquifer features of interest (e.g. dimensions, porosity and permeability) requires the modelling of poroelastic waves. The generally accepted theory is due to Biot [7, 8], who proposed an extension of the ordinary elastic theory (see below). The most notable aspect of the Biot theory is the existence of a (usually much slower) secondary P-wave. For example, when a seismic wave meets a fluid-saturated medium it scatters and, in addition to the usual S-wave, the transmitted wave splits into fast and slow P-waves. Biot also identified two regimes, depending on the frequency content of the propagating wave. In the low-frequency regime fluid flow is laminar and the wave is diffusive. In the high-frequency regime the viscodynamic effects are more complicated (see Section 4). In practice the existence of the slow P-wave puts a significant constraint on numerical schemes, making the task of solving related inverse problems very challenging, [9, 10]. In these preliminary papers we addressed some restricted inverse problems and dealt mainly with the computational challenges associated with poroelastic inverse problems. For the forward model we used the SPECFEM2D code based on the spectral element method due to Morency and Tromp, [11]. However issues with the SPECFEM2D code (discussed later in the paper) led us to developing the discontinuous Galerkin (DG) formulation discussed in this paper.

Methods for simulating poroelastic waves range from finite differences, spectral and pseudo-spectral methods to the more recent DG method. A broad ranging review of computational poroelasticity is given in [12]. We refer also to the recent papers [13, 19, 20] who work in a finite volume setting. DG methods have been implemented previously for poroelastic wave propagation; we mention [14, 15] who worked in the time domain, while the recent paper [16] considers frequency domain solutions. Wilcox et al. [17] consider three-dimensional coupled acoustic/elastic wave propagation. They note that the method of [18] uses a flux that takes into account material properties from only one side of an interface. Instead in this paper we solve an exact Riemann problem as in [17].

The DG method was originally proposed in 1973 by Reed and Hill to solve first-order scalar hyperbolic problems [21]. Since then the method has been extensively analysed [22, 23, 24, 25, 26, 27]. Furthermore, the DG method and many variants have been applied to many problems, including first- and second-order hyperbolic problems such as Maxwell's equations and the elastic and acoustic wave equations [28, 29, 30, 31, 32, 17, 33].

The first step in a DG method is to divide the computational domain into a set of elements. Polynomial basis functions are then defined for each element, where often a subclass of the Jacobi polynomials are used. One or two applications of Green's theorem give so-called weak or strong variational forms of the underlying hyperbolic system where, as usual, the solution and the test functions belong to the span of the basis functions, see [34] . The surface term that appears as a result of the local integration over an element is interpreted as a numerical flux at the interfaces between pairs of adjacent elements. Here, the DG method borrows heavily from the finite volume method and the theory of Riemann solvers, see [35, 34], to estimate

the numerical flux. In this work, time integration is carried out mainly using the low-storage Runge-Kutta (LSRK) method, see [36, 34], while in the Biot low frequency regime we also consider an IMEX implicit-explicit scheme [48]. However, there are many alternatives including the space-time DG method [33, 37] and the ADER approach using arbitrary high-order derivatives [38, 39, 40]. For example, the ADER scheme with the DG method has been successfully applied to model elastic, poroelastic, and electromagnetic wave propagation, see for example [30, 32, 15, 41]. Reviews of developments in the DG methods in are given in [42, 34].

The structure of this article is as follows. First, in Section 2, we outline formulations of Biot's equations. In Section 3, we describe the numerical scheme used in this study while Section 4 we consider poro-viscoelasticity. In Section 5, we discuss the coupling between elastic and poroelastic material. Then, in Section 6, we present a numerical experiments. Finally, a discussion and concluding remarks are given in Sections 7 and 8, respectively.

2. Formulations of Biot's equations of motion

2.1. Background

In [7] and [8] Biot proposed a theory of poroelastic wave propagation through a saturated medium, which may be regarded as an extension of the classical elastic theory. In this situation it is necessary to model the coupled mechanism of stress transmission through the solid and fluid parts. Assuming that the strain energy is a quadratic function of the solid matrix and fluid dilatations, one obtains a natural coupling between the pore pressure and the effective stress, in which the parameters may be interpreted as generalised stiffness parameters. Biot also postulated a quadratic form for the kinetic energy in terms of the solid and fluid displacements, where the coefficients are interpreted as generalised densities. For practical purposes this term is most satisfactorily written in terms of the fluid tortuosity, [43]. As noted above the most notable conclusion of the elementary Biot theory is the existence of a secondary slow P-wave, where the solid and fluid wave amplitudes have opposite phase. This has the undesirable feature that it may set an inconvenient restriction on a numerical scheme, since the grid refinement is controlled by the shortest wavelength, see [9, 10]. Biot also considered the situation of wave dissipation, which may occur when there is a relative motion between the solid and fluid, and identified a low-frequency (laminar) and high-frequency regime.

There are several formulations of the Biot equations of poroelastic wave propagation, which roughly track the evolution of Biot's work. For convenience we begin with the original Biot formulation and then give an account of the formulations commonly found in the literature.

Letting $\mathbf{u}_\mathrm{s}$ denote solid displacement and $\mathbf{u}_\mathrm{f}$ denote fluid displacement, and assuming laminar (Poiseuille)

flow, Biot's model as given in [7] may be stated as follows:

$$\rho_{11}\frac{\partial^2 \mathbf{u}_\mathrm{s}}{\partial t^2} + \rho_{12}\frac{\partial^2 \mathbf{u}_\mathrm{f}}{\partial t^2} + b\frac{\partial}{\partial t}(\mathbf{u}_\mathrm{s} - \mathbf{u}_\mathrm{f}) = \nabla \cdot (1-\phi)\mathbf{T}_\mathrm{s}, \tag{1}$$

$$\rho_{12}\frac{\partial^2 \mathbf{u}_\mathrm{s}}{\partial t^2} + \rho_{22}\frac{\partial^2 \mathbf{u}_\mathrm{f}}{\partial t^2} - b\frac{\partial}{\partial t}(\mathbf{u}_\mathrm{s} - \mathbf{u}_\mathrm{f}) = \nabla \cdot \phi\mathbf{T}_\mathrm{f}, \tag{2}$$

where ρ_{11}, ρ_{12} and ρ_{22} are generalised densities and the 'Biot coefficient' b is given in terms of the matrix permeability k, porosity ϕ and fluid viscosity η as follows:

$$b = \frac{\eta\phi^2}{k}.$$

The stress tensors $\mathbf{T}_\mathrm{s}$ and $\mathbf{T}_\mathrm{f}$ were given as generalised isotropic Hooke's laws and were later formulated in [44] in terms of theoretically measurable stiffness coefficients. These will be discussed in more detail below.

In [45], equation (8.21), Biot shows that the coupling coefficient ρ_{12} may be interpreted in terms of the fluid tortuosity τ:

$$\rho_{12} = \phi\rho_\mathrm{f}(1-\tau),$$

which permits the effective mass densities ρ_{12} and ρ_{22} to be expressed as

$$\rho_{11} = (1-\phi)\rho_\mathrm{s} - \phi(1-\tau)\rho_\mathrm{f} \tag{3}$$

$$\rho_{22} = \tau\phi\rho_\mathrm{f} \tag{4}$$

where ρ_s and ρ_f are the solid and fluid densities, respectively. For modern derivations see [43], Section 7.4, and [11].

The second notable aspects of Biot's early analysis [7, 8] is that he obtains a characteristic frequency f_c, below which the Pouiselle assumption is valid and inertial forces are negligible to viscous forces:

$$f_c = \frac{\eta\phi}{2\pi\tau\rho_\mathrm{f}k}. \tag{5}$$

See [43], Section 7.6.1. At higher frequencies, inertial forces are no longer negligible, and the viscous resistance to fluid flow given by b is frequency-dependent. In [8] Biot uses a frequency-dependent correction factor in b, while in [45] considers a viscodynamic operator.

In [45] Biot reformulates his equations in terms of $\mathbf{u}_\mathrm{s}$ and the relative displacement of fluid $\mathbf{w} = \phi(\mathbf{u}_\mathrm{f} - \mathbf{u}_\mathrm{s})$. This is the formulation normally found in the literature, and the one considered in this paper. Note that $\mathbf{w}$ is volumetric flow per unit area of the bulk medium. Adding equations (1) and (2) gives

$$\rho_\mathrm{a}\frac{\partial^2 \mathbf{u}_\mathrm{s}}{\partial t^2} + \rho_\mathrm{f}\frac{\partial^2 \mathbf{w}}{\partial t^2} = \nabla \cdot \mathbf{T} \tag{6}$$

where ρ_a is the average density

$$\rho_\mathrm{a} = (1-\phi)\rho_\mathrm{s} + \phi\rho_\mathrm{f}$$

and $\mathbf{T} = (1-\phi)\mathbf{T}_s + \phi\mathbf{T}_\mathrm{f}$ is total stress. Equation (2) can also be reformulated in terms of $\mathbf{u}_\mathrm{s}$ and $\mathbf{w}$ which gives Biot's revised system (equation (8.24), [45]):

$$\rho_\mathrm{a}\frac{\partial^2\mathbf{u}_\mathrm{s}}{\partial t^2} + \rho_\mathrm{f}\frac{\partial^2\mathbf{w}}{\partial t^2} = \nabla\cdot\mathbf{T}, \tag{7}$$

$$\rho_\mathrm{f}\frac{\partial^2\mathbf{u}_\mathrm{s}}{\partial t^2} + m\frac{\partial^2\mathbf{w}}{\partial t^2} + \frac{\eta}{k}\frac{\partial\mathbf{w}}{\partial t} = \nabla\cdot\mathbf{T}_\mathrm{f}, \tag{8}$$

where

$$m = \rho_\mathrm{f}\tau/\phi. \tag{9}$$

For a detailed derivation see [43]. Note that this formulation presumes a constant porosity. However, Morency and Tromp [11] and Carcione [43] show that the same equations hold for variable porosity. We note that our numerical implementation accurately resolves discontinuous porosities as well as material discontinuities in general, the former being a problem for the spectral element method; see Section 13.3.3 in [11]. At this point there are several options for reformulating and generalising the second equation to include the high-frequency regime. Carcione, for example, in [43], Section 7.6.1, introduces the low-frequency viscodynamic operator

$$Y(t) = m\partial_t\delta(t) + \frac{\eta}{k}\delta(t) \tag{10}$$

in which case the second equation can be written as

$$\rho_\mathrm{f}\frac{\partial^2\mathbf{u}_\mathrm{s}}{\partial t^2} + Y * \frac{\partial\mathbf{w}}{\partial t} = \nabla\cdot\mathbf{T}_\mathrm{f} \tag{11}$$

Morency and Tromp, [11], work with a second-order frequency-dependent symmetric tensor $b = b(t)$ and write the second equation in the form

$$m\frac{\partial^2\mathbf{w}}{\partial t^2} + \rho_\mathrm{f}\frac{\partial^2\mathbf{u}_\mathrm{s}}{\partial t^2} + b * \frac{\partial\mathbf{w}}{\partial t} = \nabla\cdot\mathbf{T}_\mathrm{f}. \tag{12}$$

This will be considered in more detail in Section 4.

With regards to generality we note that the original theory was developed for isotropic media, [7] and [8], whereas [45, 46] consider extensions to anisotropic media. In this paper we deal with the isotropic case, while [13] deals with the more general case of orthotropic media.

2.2. Poroelastic Hooke's laws

In [7] Biot proposed generalised Hooke's laws to describe the stress-strain coupling between solid and fluid. Letting $\mathbf{E}$ denote the solid strain tensor

$$\mathbf{E} = \frac{1}{2}(\nabla\mathbf{u}_\mathrm{s} + (\nabla\mathbf{u}_\mathrm{s})^\mathsf{T})$$

and $\epsilon = \nabla\cdot\mathbf{u}_\mathrm{f}$ the strain in the fluid, these may be stated in the form:

$$(1-\phi)\mathbf{T}_\mathrm{s} = 2\mu\mathbf{E} + \lambda\,\mathrm{trace}(\mathbf{E})\mathbf{I} + Q\epsilon\mathbf{I} \tag{13}$$

$$\phi\mathbf{T}_\mathrm{f} = Q\,\mathrm{trace}(\mathbf{E})\mathbf{I} + M\epsilon\mathbf{I} \tag{14}$$

where μ and λ correspond to the usual Lamé coefficients, Q and M are Biot's original notation defined in equations (18) and (19) below, and $\mathbf{I}$ denotes the identity tensor. As usual, under the assumption that the fluid does not support shear stress, one may interpret μ as the dry matrix shear modulus μ_{fr}.

Biot and Willis [44] showed that the elasticity coefficients postulated above may be written in terms of bulk moduli defined by idealised experiments, viz. the bulk frame modulus of the frame κ_{fr}, the bulk modulus of the solid κ_{s} and the bulk modulus of the fluid κ_{f}. Carcione gives a detailed account in [43]. Since we are interested in the system (7)–(8), we may write

$$\mathbf{T} = 2\mu_{\mathrm{fr}}\mathbf{E} + \left(B - \frac{2}{3}\mu_{\mathrm{fr}}\right)\mathrm{trace}(\mathbf{E})\mathbf{I} - C\zeta\mathbf{I} \tag{15}$$

$$\mathbf{T}_{\mathrm{f}} = C\,\mathrm{trace}(\mathbf{E})\mathbf{I} - M\zeta\mathbf{I} \tag{16}$$

where $\zeta = -\nabla\cdot\mathbf{w}$ is the variation of fluid content, and the moduli B, C, and M can be written as

$$B = \frac{\kappa_{\mathrm{s}} - (1+\phi)\kappa_{\mathrm{fr}} + \phi\kappa_{\mathrm{s}}\kappa_{\mathrm{fr}}/\kappa_{\mathrm{f}}}{(1-\kappa_{\mathrm{fr}}/\kappa_{\mathrm{s}}) - \phi(1-\kappa_{\mathrm{s}}/\kappa_{\mathrm{f}})}, \tag{17}$$

$$C = \frac{(1-\kappa_{\mathrm{fr}}/\kappa_{\mathrm{s}})\kappa_{\mathrm{s}}}{(1-\kappa_{\mathrm{fr}}/\kappa_{\mathrm{s}}) - \phi(1-\kappa_{\mathrm{s}}/\kappa_{\mathrm{f}})} = Q, \tag{18}$$

and

$$M = \frac{\kappa_{\mathrm{s}}}{(1-\kappa_{\mathrm{fr}}/\kappa_{\mathrm{s}}) - \phi(1-\kappa_{\mathrm{s}}/\kappa_{\mathrm{f}})}. \tag{19}$$

One of the less desirable aspects of poroelastic theory is the proliferation of constants. A neater formulation that is possibly better suited to estimation is to introduce the Biot effective stress constant α given by

$$\alpha = 1 - \frac{\kappa_{\mathrm{fr}}}{\kappa_{\mathrm{s}}}.$$

Then we can write the solid and fluid stress tensors as

$$\mathbf{T} = 2\mu_{\mathrm{fr}}\mathbf{E} + \left(\kappa_{\mathrm{fr}} + \alpha^2 M - \frac{2}{3}\mu_{\mathrm{fr}}\right)\mathrm{trace}(\mathbf{E})\mathbf{I} - \alpha M\zeta\mathbf{I} \tag{20}$$

$$\mathbf{T}_{\mathrm{f}} = M(\alpha\,\mathrm{trace}(\mathbf{E}) - \zeta)\mathbf{I}. \tag{21}$$

3. Numerical scheme for the inviscid case

3.1. Hyperbolic system

We use a velocity-strain formulation to express (7)–(8) as a first-order conservative hyperbolic system. Introducing the variable

$$\mathbf{q} = (\epsilon_{11}, \epsilon_{22}, \epsilon_{12}, \zeta, u_{\mathrm{s}}, v_{\mathrm{s}}, u_{\mathrm{f}}, v_{\mathrm{f}})^{\mathsf{T}} \tag{22}$$

where the ϵ_{ij} are components of the solid strain tensor, ζ is the variation of fluid content, $\mathbf{v}_\mathrm{s} = (u_\mathrm{s}, v_\mathrm{s})$ are the x and y components of the solid velocity $\dfrac{\partial \mathbf{u}_\mathrm{s}}{\partial t}$ and $\mathbf{v}_\mathrm{f} = (u_\mathrm{f}, v_\mathrm{f})$ the components of the relative fluid velocity $\dfrac{\partial \mathbf{w}}{\partial t}$, viz.

$$\mathbf{E} = \begin{pmatrix} \epsilon_{11} & \epsilon_{12} \\ \epsilon_{12} & \epsilon_{22} \end{pmatrix} \tag{23}$$

and

$$\zeta = -\nabla \cdot \mathbf{w} \tag{24}$$

$$(u_\mathrm{s}, v_\mathrm{s})^\mathsf{T} = \frac{\partial \mathbf{u}_\mathrm{s}}{\partial t} \tag{25}$$

$$(u_\mathrm{f}, v_\mathrm{f})^\mathsf{T} = \frac{\partial \mathbf{w}}{\partial t} \tag{26}$$

we obtain

$$Q\frac{\partial \mathbf{q}}{\partial t} + \nabla \cdot \mathcal{F} = Q\frac{\partial \mathbf{q}}{\partial t} + \frac{\partial (A\mathbf{q})}{\partial x} + \frac{\partial (B\mathbf{q})}{\partial y} = \mathbf{g} + \mathbf{g}_V \tag{27}$$

where

$$\mathcal{F} = [F_1, F_2] = [A\mathbf{q}, B\mathbf{q}]$$

and

$$Q = \begin{pmatrix} 1 & 0 & 0 & 0 & 0 & 0 & 0 & 0 \\ 0 & 1 & 0 & 0 & 0 & 0 & 0 & 0 \\ 0 & 0 & 1 & 0 & 0 & 0 & 0 & 0 \\ 0 & 0 & 0 & 1 & 0 & 0 & 0 & 0 \\ 0 & 0 & 0 & 0 & \rho_\mathrm{a} & 0 & \rho_\mathrm{f} & 0 \\ 0 & 0 & 0 & 0 & 0 & \rho_\mathrm{a} & 0 & \rho_\mathrm{f} \\ 0 & 0 & 0 & 0 & \rho_\mathrm{f} & 0 & m & 0 \\ 0 & 0 & 0 & 0 & 0 & \rho_\mathrm{f} & 0 & m \end{pmatrix}. \tag{28}$$

The Jacobian matrices A and B are given by

$$A = -\begin{pmatrix} 0 & 0 & 0 & 0 & 1 & 0 & 0 & 0 \\ 0 & 0 & 0 & 0 & 0 & 0 & 0 & 0 \\ 0 & 0 & 0 & 0 & 0 & 1/2 & 0 & 0 \\ 0 & 0 & 0 & 0 & 0 & 0 & -1 & 0 \\ 2\mu_\mathrm{fr} + \lambda & \lambda & 0 & -\alpha M & 0 & 0 & 0 & 0 \\ 0 & 0 & 2\mu_\mathrm{fr} & 0 & 0 & 0 & 0 & 0 \\ M\alpha & M\alpha & 0 & -M & 0 & 0 & 0 & 0 \\ 0 & 0 & 0 & 0 & 0 & 0 & 0 & 0 \end{pmatrix} \tag{29}$$

and

$$B = -\begin{pmatrix} 0 & 0 & 0 & 0 & 0 & 0 & 0 & 0 \\ 0 & 0 & 0 & 0 & 0 & 1 & 0 & 0 \\ 0 & 0 & 0 & 0 & 1/2 & 0 & 0 & 0 \\ 0 & 0 & 0 & 0 & 0 & 0 & 0 & -1 \\ 0 & 0 & 2\mu_{\rm fr} & 0 & 0 & 0 & 0 & 0 \\ \lambda & 2\mu_{\rm fr}+\lambda & 0 & -\alpha M & 0 & 0 & 0 & 0 \\ 0 & 0 & 0 & 0 & 0 & 0 & 0 & 0 \\ M\alpha & M\alpha & 0 & -M & 0 & 0 & 0 & 0 \end{pmatrix} \tag{30}$$

where $\lambda = \kappa_{\rm fr} + \alpha^2 M - \frac{2}{3}\mu_{\rm fr}$. For the low-frequency dissipative regime considered in Section 4 the source term $\mathbf{g}$ is given by

$$\mathbf{g} = (0,0,0,0,0,0,-\frac{\eta}{k}u_{\rm f}, -\frac{\eta}{k}v_{\rm f})^{\mathsf{T}} \tag{31}$$

while $\mathbf{g}_V$ is a volume source, which is defined later in Section 6.

The eigenstructure of $Q^{-1}A$ (and $Q^{-1}B$) parallels the elastic case given in [17]. See also [35], Chapter 22 for background material. The derivations are given in the appendix and are summarised below. Introducing the quantities

$$Z_1 = m\rho_{\rm a} - \rho_{\rm f}^2 \tag{32}$$

$$Z_2 = -2\rho_{\rm f}\alpha M + \rho_{\rm a} M + m\lambda + 2m\mu_{\rm fr} \tag{33}$$

$$Z_3 = \rho_{\rm a}(4\alpha^2 m - 4\alpha\rho_{\rm f} + \rho_{\rm a})M^2 - 2(2\alpha m\rho_{\rm f} + m\rho_{\rm a} - 2\rho_{\rm f}^2)M(2\mu_{\rm fr}+\lambda) + m^2(2\mu_{\rm fr}+\lambda)^2 \tag{34}$$

$$Z_4 = \rho_{\rm a} M - m\lambda - 2m\mu_{\rm fr} \tag{35}$$

$$Z_5 = 2(\alpha m - \rho_{\rm f})M \tag{36}$$

we have the following expressions for the wave speeds for the non-dissipative case:

$$c_p^{\rm I} = \pm\sqrt{\frac{Z_2 + \sqrt{Z_3}}{2Z_1}} \tag{37}$$

$$c_p^{\rm II} = \pm\sqrt{\frac{Z_2 - \sqrt{Z_3}}{2Z_1}} \tag{38}$$

$$c_s = \pm\sqrt{\frac{m\mu_{\rm fr}}{Z_1}}. \tag{39}$$

Here $c_p^{\rm I}$ is the speed of the fast P-wave corresponding to the P-wave of ordinary elasticity, $c_p^{\rm II}$ is Biot's slow P-wave, and c_s is the speed of the shear wave, where usually $c_p^{\rm I} < c_s < c_p^{\rm II}$. Writing $\Lambda = {\rm diag}(-c_p^{\rm I}, -c_s, -c_p^{\rm II}, 0, 0, c_p^{\rm II}, c_s, c_p^{\rm II})$

we show in the appendix that representative eigenvectors of $Q^{-1}A$ are given by the columns of

$$R = \begin{pmatrix} 1 & 0 & 1 & 0 & 2\mu_{\rm fr}/3 - \kappa_{\rm fr} & 1 & 0 & 1 \\ 0 & 0 & 0 & 0 & 4\mu_{\rm fr}/3 + \kappa_{\rm fr} & 0 & 0 & 0 \\ 0 & 1/2 & 0 & 0 & 0 & 0 & 1/2 & 0 \\ -\gamma_1 & 0 & -\gamma_2 & 0 & 2\mu_{\rm fr} & -\gamma_2 & 0 & -\gamma_1 \\ c_p^{\rm I} & 0 & c_p^{\rm II} & 0 & 0 & -c_p^{\rm II} & 0 & -c_p^{\rm I} \\ 0 & c_s & 0 & 0 & 0 & 0 & -c_s & 0 \\ \gamma_1 c_p^{\rm I} & 0 & \gamma_2 c_p^{\rm II} & 0 & 0 & -\gamma_2 c_p^{\rm II} & 0 & -\gamma_1 c_p^{\rm I} \\ 0 & -c_s\rho_{\rm f}/m & 0 & 1 & 0 & 0 & c_s\rho_{\rm f}/m & 0 \end{pmatrix} \tag{40}$$

where $\gamma_1 = (Z_4 + \sqrt{Z_3})/Z_5$ and $\gamma_2 = (Z_4 - \sqrt{Z_3})/Z_5$ and hence we obtain the spectral decomposition $A = R\Lambda R^{-1}$. Note that in the dissipative low-frequency regime wave speeds become frequency-dependent. Formulae are derived in the appendix.

3.2. Discontinuous Galerkin method

In this section we outline the DG method. Our formulation follows Hesthaven and Warburton, [34] where a detailed account of the DG method can be found. We first suppose that the computational domain $\Omega \subset \mathbb{R}^2$ is triangulated using K elements

$$\Omega = \bigcup_{k=1}^{K} D^k.$$

The boundary of element D^k is denoted by ∂D^k. We assume that the elements are aligned with material discontinuities. Furthermore, for any element D^k the superscript '$-$' refers to interior information while '$+$' refers to exterior information.

To obtain the strong form we multiply (27) by a local test function p^k and integrate by parts twice to obtain an elementwise variational formulation

$$\int_{D^k} \left(Q\frac{\partial \mathbf{q}^k}{\partial t} + \nabla \cdot \mathcal{F} - \mathbf{g} - \mathbf{g}_V \right) p^k d\mathbf{x} = \oint_{\partial D^k} \hat{\mathbf{n}} \cdot (\mathcal{F}^- - \mathcal{F}^*) p^k d\Gamma, \tag{41}$$

where $\hat{\mathbf{n}}$ is an outward pointing unit normal, $\mathbf{q}^k$ is the restriction of $\mathbf{q}$ to the element D^k and $\mathcal{F}^*$ is the numerical flux across neighbouring element interfaces. In the discrete form, the test functions p^k are assumed be multivariate Lagrange polynomials resulting from the nodal DG method (we refer to [15] for a detailed discussion of the nodal spatial discretization).

To approximate the numerical flux $\mathcal{F}^*$ along the normal $\hat{\mathbf{n}}$ we solve the Riemann problem at an interface. With this in mind we define

$$\Pi = \hat{n}_x A + \hat{n}_y B$$

so that

$$\hat{\mathbf{n}} \cdot \mathcal{F} = \Pi \mathbf{q}$$

3.3. Boundary conditions

The ground surface of the porous medium is modelled as a free surface by assuming that the strain components and the variation of fluid content vanish, [43]:

$$\epsilon_{11} = \epsilon_{22} = \epsilon_{12} = 0, \quad \zeta = 0. \tag{42}$$

The other boundaries are modelling as absorbing boundaries. We implement these boundaries as outflow boundaries by setting the flux equal to zero. This is only exact for one-dimensional problems and may introduce boundary artefacts. This is discussed in Section 7.

3.4. Riemann problem

Now that the eigenstructure of $Q^{-1}A$ has been established we proceed to solve the Riemann problem for (22) using essentially the same calculations carried out in [17] with a modest loss in elegance and simplicity.

In the following calculations it is convenient to work with a local interface basis $\{\hat{\mathbf{n}}, \hat{\mathbf{s}}\}$ where $\hat{\mathbf{s}}$ is a unit tangent vector. Using a prime to denote vectors with respect to the interface basis, we write $\mathbf{q} = L\mathbf{q}'$ where L is the change of basis map from $\{\hat{\mathbf{n}}, \hat{\mathbf{s}}\}$ to the physical Euclidean basis $\{\hat{\mathbf{e}}_1, \hat{\mathbf{e}}_2\}$. It is straightforward to show that

$$\mathbf{q}' = L^{-1}\mathbf{q} = (\hat{\mathbf{n}}^{\mathsf{T}}\mathbf{E}\hat{\mathbf{n}}, \hat{\mathbf{s}}^{\mathsf{T}}\mathbf{E}\hat{\mathbf{s}}, \hat{\mathbf{s}}^{\mathsf{T}}\mathbf{E}\hat{\mathbf{n}}, \zeta, \hat{\mathbf{n}} \cdot \mathbf{v}_{\mathrm{s}}, \hat{\mathbf{s}} \cdot \mathbf{v}_{\mathrm{s}}, \hat{\mathbf{n}} \cdot \mathbf{v}_{\mathrm{f}}, \hat{\mathbf{s}} \cdot \mathbf{v}_{\mathrm{f}})^{\mathsf{T}}. \tag{43}$$

Letting $P = [\hat{\mathbf{n}}\ \hat{\mathbf{s}}]$ the first three terms follow from the change of basis formula for a matrix $\mathbf{E}' = P^{\mathsf{T}}\mathbf{E}P$, and the last four terms follow from $\mathbf{v}' = P^{\mathsf{T}}\mathbf{v}$. We also have

$$L^{-1}\Pi L = A \text{ and } L^{-1}Q^{-1}\Pi L = Q^{-1}A \tag{44}$$

To compute an upwind numerical flux across an interface for the two-dimensional locally isotropic poroelastic system (22) we solve a Riemann problem at an interface. This consists of solving the system (22) with initial data

$$\mathbf{q}_0(\mathbf{x}) = \begin{cases} \mathbf{q}^- & \text{if } \hat{\mathbf{n}} \cdot (\mathbf{x} - \mathbf{x}_0) < 0 \\ \mathbf{q}^+ & \text{if } \hat{\mathbf{n}} \cdot (\mathbf{x} - \mathbf{x}_0) > 0 \end{cases}$$

where $\mathbf{x}_0$ is a point on the interface.

For each wave speed c, the Rankine-Hugoniot jump condition, [34, 35]

$$-cQ[\mathbf{q}^- - \mathbf{q}^+] + [(\Pi\mathbf{q})^- - (\Pi\mathbf{q})^+] = 0$$

holds across each wave, where the superscripts $-$ and $+$ refer respectively to the interior and exterior information on an element. We have six unknown states $(\mathbf{q}^a, \mathbf{q}^b, \mathbf{q}^c, \mathbf{q}^d, \mathbf{q}^e, \mathbf{q}^f)$ shown in Figure 1, with the

following jump conditions:

$$(c_p^{\mathrm{I}})^- Q^- (\mathbf{q}^- - \mathbf{q}^a) + \Pi^- (\mathbf{q}^- - \mathbf{q}^a) = 0 \tag{45}$$

$$(c_s)^- Q^- (\mathbf{q}^a - \mathbf{q}^b) + \Pi^- (\mathbf{q}^a - \mathbf{q}^b) = 0 \tag{46}$$

$$(c_p^{\mathrm{II}})^- Q^- (\mathbf{q}^b - \mathbf{q}^c) + \Pi^- (\mathbf{q}^b - \mathbf{q}^c) = 0 \tag{47}$$

$$\Pi^- \mathbf{q}^c - \Pi^+ \mathbf{q}^d = 0 \tag{48}$$

$$-(c_p^{\mathrm{II}})^+ Q^+ (\mathbf{q}^d - \mathbf{q}^e) + \Pi^+ (\mathbf{q}^d - \mathbf{q}^e) = 0 \tag{49}$$

$$-(c_s)^+ Q^+ (\mathbf{q}^e - \mathbf{q}^f) + \Pi^+ (\mathbf{q}^e - \mathbf{q}^f) = 0 \tag{50}$$

$$-(c_p^{\mathrm{I}})^+ Q^+ (\mathbf{q}^f - \mathbf{q}^+) + \Pi^+ (\mathbf{q}^f - \mathbf{q}^+) = 0 \tag{51}$$

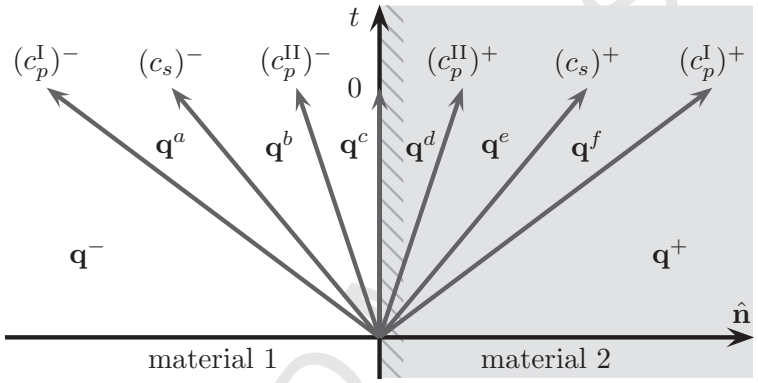

Figure 1: Schematic showing characteristic wave speeds at a poroelastic interface between two states $\mathbf{q}^-$ and $\mathbf{q}^+$. $\mathbf{q}^a$– $\mathbf{q}^f$ denote the intermediate states.

Thus:

$$\mathbf{q}^- - \mathbf{q}^a = \beta_1 \mathbf{r}_1^- \tag{52}$$

$$\mathbf{q}^a - \mathbf{q}^b = \beta_2 \mathbf{r}_2^- \tag{53}$$

$$\mathbf{q}^b - \mathbf{q}^c = \beta_3 \mathbf{r}_3^- \tag{54}$$

$$\mathbf{q}^d - \mathbf{q}^e = \beta_6 \mathbf{r}_6^+ \tag{55}$$

$$\mathbf{q}^e - \mathbf{q}^f = \beta_7 \mathbf{r}_7^+ \tag{56}$$

$$\mathbf{q}^f - \mathbf{q}^- = \beta_8 \mathbf{r}_8^+ \tag{57}$$

where $\mathbf{r}_j^\pm$ is an eigenvector of $(Q^\pm)^{-1}\Pi^\pm$ corresponding to wave speed $c_j^\pm$ and hence

$$\mathbf{q}^- - \mathbf{q}^c = \beta_1 \mathbf{r}_1^- + \beta_2 \mathbf{r}_2^- + \beta_3 \mathbf{r}_3^- \tag{58}$$

$$\mathbf{q}^d - \mathbf{q}^+ = \beta_6 \mathbf{r}_6^+ + \beta_7 \mathbf{r}_7^+ + \beta_8 \mathbf{r}_8^+ \tag{59}$$

We now make use of the orthogonality of the P-wave and the S-wave eigenvectors to uncouple the system (58) and (59). Recall that the eigenvectors $\mathbf{r}_1^-, \mathbf{r}_6^+$ correspond to fast P-waves, $\mathbf{r}_3^-, \mathbf{r}_8^+$ to slow P-waves, and $\mathbf{r}_2^-, \mathbf{r}_7^+$ to S-waves. First we deal with the P-wave coefficients $\beta_1, \beta_3, \beta_6, \beta_8$.

From the interface condition (48) we have

$$\Pi^- \mathbf{q}^c = \Pi^+ \mathbf{q}^d$$

and so

$$L^{-1}\Pi^- \mathbf{q}^c = L^{-1}\Pi^+ \mathbf{q}^d.$$

Using the first equality in (44) this gives

$$A^-(L^{-1}\mathbf{q}^c) = A^+(L^{-1}\mathbf{q}^d),$$

that is

$$A^-(\mathbf{q}^c)' = A^+(\mathbf{q}^d)'. \tag{60}$$

Recalling that

$$\mathbf{T}^\pm = 2\mu_{\rm fr}^\pm \mathbf{E} + \lambda^\pm \operatorname{trace}(\mathbf{E})\mathbf{I} - \alpha^\pm M^\pm \zeta^\pm \mathbf{I}$$

where $\lambda^\pm = \kappa_{\rm fr}^\pm + \alpha^{2\pm} M^\pm - \dfrac{2}{3}\mu_{\rm fr}^\pm$ and the $\pm$ indicates whether $\mathbf{T}$ is evaluated on the interior or exterior of the interface, it follows that

$$\begin{aligned}
\hat{\mathbf{n}}^{\mathsf T}\mathbf{T}^\pm\hat{\mathbf{n}} &= 2\mu_{\rm fr}^\pm \hat{\mathbf{n}}^{\mathsf T}\mathbf{E}^\pm\hat{\mathbf{n}} + \lambda^\pm \operatorname{trace}(\mathbf{E}^\pm)\hat{\mathbf{n}}^{\mathsf T}\mathbf{I}\hat{\mathbf{n}} - \alpha^\pm M^\pm\zeta^\pm \hat{\mathbf{n}}^{\mathsf T}\mathbf{I}\hat{\mathbf{n}} \\
&= 2\mu_{\rm fr}^\pm \hat{\mathbf{n}}^{\mathsf T}\mathbf{E}^\pm\hat{\mathbf{n}} + \lambda^\pm \operatorname{trace}(\mathbf{E}^\pm) - \alpha^\pm M^\pm\zeta^\pm \\
&= 2\mu_{\rm fr}^\pm \hat{\mathbf{n}}^{\mathsf T}\mathbf{E}^\pm\hat{\mathbf{n}} + \lambda^\pm (\hat{\mathbf{n}}^{\mathsf T}\mathbf{E}^\pm\hat{\mathbf{n}} + \hat{\mathbf{s}}^{\mathsf T}\mathbf{E}^\pm\hat{\mathbf{s}}) - \alpha^\pm M^\pm\zeta^\pm
\end{aligned} \tag{61}$$

since the trace is invariant under orthogonal transformations. We also have

$$\hat{\mathbf{s}}^{\mathsf T}\mathbf{T}^\pm\hat{\mathbf{n}} = 2\mu_{\rm fr}\hat{\mathbf{s}}^{\mathsf T}\mathbf{E}^\pm\hat{\mathbf{n}}. \tag{62}$$

We obtain similarly for

$$\mathbf{T}_{\rm f}^\pm = M^\pm(\alpha^\pm \operatorname{trace}(\mathbf{E}^\pm) - \zeta^\pm)\mathbf{I}$$

the following identity:

$$\begin{aligned}
\hat{\mathbf{n}}^{\mathsf T}\mathbf{T}_{\rm f}^\pm\hat{\mathbf{n}} &= M^\pm\alpha^\pm \operatorname{trace}(\mathbf{E}^\pm) - M^\pm\zeta^\pm \\
&= M^\pm\alpha^\pm(\hat{\mathbf{n}}^{\mathsf T}\mathbf{E}^\pm\hat{\mathbf{n}} + \hat{\mathbf{s}}^{\mathsf T}\mathbf{E}^\pm\hat{\mathbf{s}}) - M^\pm\zeta^\pm.
\end{aligned} \tag{63}$$

Also

$$\hat{\mathbf{s}}^{\mathsf T}\mathbf{T}_{\rm f}^\pm\hat{\mathbf{n}} = 0. \tag{64}$$

From (60) we obtain the following flux continuity relations

$$\hat{\mathbf{n}} \cdot \mathbf{v}_{\mathrm{s}}^{c} = \hat{\mathbf{n}} \cdot \mathbf{v}_{\mathrm{s}}^{d} \tag{65}$$

$$\hat{\mathbf{s}} \cdot \mathbf{v}_{\mathrm{s}}^{c} = \hat{\mathbf{s}} \cdot \mathbf{v}_{\mathrm{s}}^{d} \tag{66}$$

$$\hat{\mathbf{n}} \cdot \mathbf{v}_{\mathrm{f}}^{c} = \hat{\mathbf{n}} \cdot \mathbf{v}_{\mathrm{f}}^{d} \tag{67}$$

$$\hat{\mathbf{n}}^{\mathsf{T}} \mathbf{T}^{c} \hat{\mathbf{n}} = \hat{\mathbf{n}}^{\mathsf{T}} \mathbf{T}^{d} \hat{\mathbf{n}} \tag{68}$$

$$\hat{\mathbf{s}}^{\mathsf{T}} \mathbf{T}^{c} \hat{\mathbf{n}} = \hat{\mathbf{s}}^{\mathsf{T}} \mathbf{T}^{d} \hat{\mathbf{n}} \tag{69}$$

$$\hat{\mathbf{n}}^{\mathsf{T}} \mathbf{T}_{\mathrm{f}}^{c} \hat{\mathbf{n}} = \hat{\mathbf{n}}^{\mathsf{T}} \mathbf{T}_{\mathrm{f}}^{d} \hat{\mathbf{n}} \tag{70}$$

where we have used (61), (62) and (63).

We now proceed with the evaluation of the β terms. From (58) we have

$$L^{-1}\mathbf{q}^{-} - L^{-1}\mathbf{q}^{c} = \beta_1(\mathbf{r}_1')^{-} + \beta_2(\mathbf{r}_2')^{-} + \beta_3(\mathbf{r}_3')^{-}$$

where the $(\mathbf{r}_j')^{-}$ are the j'th columns of the eigenvector matrix R given by equation (40) evaluated in the interior of an element. Unwrapping, and using (43), we obtain the relationships

$$\hat{\mathbf{n}}^{\mathsf{T}} \mathbf{E}^{-} \hat{\mathbf{n}} - \hat{\mathbf{n}}^{\mathsf{T}} \mathbf{E}^{c} \hat{\mathbf{n}} = \beta_1 + \beta_3 \tag{71}$$

$$\hat{\mathbf{s}}^{\mathsf{T}} \mathbf{E}^{-} \hat{\mathbf{s}} = \hat{\mathbf{s}}^{\mathsf{T}} \mathbf{E}^{c} \hat{\mathbf{s}} \tag{72}$$

$$\hat{\mathbf{s}}^{\mathsf{T}} \mathbf{E}^{-} \hat{\mathbf{n}} - \hat{\mathbf{s}}^{\mathsf{T}} \mathbf{E}^{c} \hat{\mathbf{n}} = \beta_2/2 \tag{73}$$

$$\zeta^{-} - \zeta^{c} = -\gamma_1^{-}\beta_1 - \gamma_2^{-}\beta_3 \tag{74}$$

$$\hat{\mathbf{n}} \cdot \mathbf{v}_{\mathrm{s}}^{-} - \hat{\mathbf{n}} \cdot \mathbf{v}_{\mathrm{s}}^{c} = (c_p^{\mathrm{I}})^{-}\beta_1 + (c_p^{\mathrm{II}})^{-}\beta_3 \tag{75}$$

$$\hat{\mathbf{s}} \cdot \mathbf{v}_{\mathrm{s}}^{-} - \hat{\mathbf{s}} \cdot \mathbf{v}_{\mathrm{s}}^{c} = (c_s)^{-}\beta_2 \tag{76}$$

$$\hat{\mathbf{n}} \cdot \mathbf{v}_{\mathrm{f}}^{-} - \hat{\mathbf{n}} \cdot \mathbf{v}_{\mathrm{f}}^{c} = (\gamma_1 c_p^{\mathrm{I}})^{-}\beta_1 + (\gamma_2 c_p^{\mathrm{II}})^{-}\beta_3 \tag{77}$$

$$\hat{\mathbf{s}} \cdot \mathbf{v}_{\mathrm{f}}^{-} - \hat{\mathbf{s}} \cdot \mathbf{v}_{\mathrm{f}}^{c} = -(c_s \rho_{\mathrm{f}}/m)^{-}\beta_2. \tag{78}$$

We derive similar relations on the right-hand side. From (59) we have

$$L^{-1}\mathbf{q}^{d} - L^{-1}\mathbf{q}^{+} = \beta_6(\mathbf{r}_6')^{+} + \beta_7(\mathbf{r}_7')^{+} + \beta_8(\mathbf{r}_8')^{+}$$

Thus:

$$\hat{\mathbf{n}}^{\mathsf{T}}\mathbf{E}^d\hat{\mathbf{n}} - \hat{\mathbf{n}}^{\mathsf{T}}\mathbf{E}^+\hat{\mathbf{n}} = \beta_6 + \beta_8 \tag{79}$$

$$\hat{\mathbf{s}}^{\mathsf{T}}\mathbf{E}^d\hat{\mathbf{s}} = \hat{\mathbf{s}}^{\mathsf{T}}\mathbf{E}^+\hat{\mathbf{s}} \tag{80}$$

$$\hat{\mathbf{s}}^{\mathsf{T}}\mathbf{E}^d\hat{\mathbf{n}} - \hat{\mathbf{s}}^{\mathsf{T}}\mathbf{E}^+\hat{\mathbf{n}} = \beta_7/2 \tag{81}$$

$$\zeta^d - \zeta^+ = -\gamma_2^+\beta_6 - \gamma_1^+\beta_8 \tag{82}$$

$$\hat{\mathbf{n}}\cdot\mathbf{v}_{\mathrm{s}}^d - \hat{\mathbf{n}}\cdot\mathbf{v}_{\mathrm{s}}^+ = -(c_p^{\mathrm{II}})^+\beta_6 - (c_p^{\mathrm{I}})^+\beta_8 \tag{83}$$

$$\hat{\mathbf{s}}\cdot\mathbf{v}_{\mathrm{s}}^d - \hat{\mathbf{s}}\cdot\mathbf{v}_{\mathrm{s}}^+ = -c_s^+\beta_7 \tag{84}$$

$$\hat{\mathbf{n}}\cdot\mathbf{v}_{\mathrm{f}}^d - \hat{\mathbf{n}}\cdot\mathbf{v}_{\mathrm{f}}^+ = -(\gamma_2 c_p^{\mathrm{II}})^+\beta_6 - (\gamma_1 c_p^{\mathrm{I}})^+\beta_8 \tag{85}$$

$$\hat{\mathbf{s}}\cdot\mathbf{v}_{\mathrm{f}}^d - \hat{\mathbf{s}}\cdot\mathbf{v}_{\mathrm{f}}^+ = (c_s\rho_{\mathrm{f}}/m)^+\beta_7. \tag{86}$$

Using the continuity condition (65), (75) and (83) we obtain

$$(c_p^{\mathrm{I}})^-\beta_1 + (c_p^{\mathrm{II}})^-\beta_3 - (c_p^{\mathrm{II}})^+\beta_6 - (c_p^{\mathrm{I}})^+\beta_8 = \hat{\mathbf{n}}\cdot(\mathbf{v}_{\mathrm{s}}^- - \mathbf{v}_{\mathrm{s}}^+). \tag{87}$$

Next from (67), (77) and (85) we obtain

$$(\gamma_1 c_p^{\mathrm{I}})^-\beta_1 + (\gamma_2 c_p^{\mathrm{II}})^-\beta_3 - (\gamma_2 c_p^{\mathrm{II}})^+\beta_6 - (\gamma_1 c_p^{\mathrm{I}})^+\beta_8 = \hat{\mathbf{n}}\cdot(\mathbf{v}_{\mathrm{f}}^- - \mathbf{v}_{\mathrm{f}}^+). \tag{88}$$

Using the continuity condition (68) and the identity (61) we obtain

$$2\mu_{\mathrm{fr}}^-\hat{\mathbf{n}}^{\mathsf{T}}\mathbf{E}^c\hat{\mathbf{n}} + \lambda^-(\hat{\mathbf{n}}^{\mathsf{T}}\mathbf{E}^c\hat{\mathbf{n}} + \hat{\mathbf{s}}^{\mathsf{T}}\mathbf{E}^c\hat{\mathbf{s}}) - \alpha^- M^-\zeta^c = 2\mu_{\mathrm{fr}}^+\hat{\mathbf{n}}^{\mathsf{T}}\mathbf{E}^d\hat{\mathbf{n}} + \lambda^+(\hat{\mathbf{n}}^{\mathsf{T}}\mathbf{E}^d\hat{\mathbf{n}} + \hat{\mathbf{s}}^{\mathsf{T}}\mathbf{E}^d\hat{\mathbf{s}}) - \alpha^+ M^+\zeta^d \tag{89}$$

We now substitute for $\mathbf{E}^c$ and $\mathbf{E}^d$ using (71), (72), (74), (79), (80) and (82)

$$\begin{aligned}(2\mu_{\mathrm{fr}}^- + \lambda^- + \alpha^- M^-\gamma_1^-)\beta_1 + (2\mu_{\mathrm{fr}}^- + \lambda^- + \alpha^- M^-\gamma_2^-)\beta_3 + (2\mu_{\mathrm{fr}}^+ + \lambda^+ + \alpha^+ M^+\gamma_2^+)\beta_6 \\ + (2\mu_{\mathrm{fr}}^+ + \lambda^+ + \alpha^+ M^+\gamma_1^+)\beta_8 = \hat{\mathbf{n}}^{\mathsf{T}}(\mathbf{T}^- - \mathbf{T}^+)\hat{\mathbf{n}}.\end{aligned} \tag{90}$$

Finally using the continuity condition (70) and the identity (63) we obtain

$$M^-\alpha^-(\hat{\mathbf{n}}^{\mathsf{T}}\mathbf{E}^c\hat{\mathbf{n}} + \hat{\mathbf{s}}^{\mathsf{T}}\mathbf{E}^c\hat{\mathbf{s}}) - M^-\zeta^c = M^+\alpha^+(\hat{\mathbf{n}}^{\mathsf{T}}\mathbf{E}^d\hat{\mathbf{n}} + \hat{\mathbf{s}}^{\mathsf{T}}\mathbf{E}^d\hat{\mathbf{s}}) - M^+\zeta^d.$$

Substituting again for $\mathbf{E}^c$ and $\mathbf{E}^d$ gives

$$M^-(\alpha^- + \gamma_1^-)\beta_1 + M^-(\alpha^- + \gamma_2^-)\beta_3 + M^+(\alpha^+ + \gamma_2^+)\beta_6 + M^+(\alpha^+ + \gamma_1^+)\beta_8 = \hat{\mathbf{n}}^{\mathsf{T}}(\mathbf{T}_{\mathrm{f}}^- - \mathbf{T}_{\mathrm{f}}^+)\hat{\mathbf{n}}. \tag{91}$$

There is no straightforward solution to the system (87)–(91). Inverting the coefficient matrix

$$\begin{pmatrix} 2\mu_{\mathrm{fr}}^- + \lambda^- + \alpha^- M^-\gamma_1^- & 2\mu_{\mathrm{fr}}^- + \lambda^- + \alpha^- M^-\gamma_2^- & 2\mu_{\mathrm{fr}}^+ + \lambda^+ + \alpha^+ M^+\gamma_2^+ & 2\mu_{\mathrm{fr}}^+ + \lambda^+ + \alpha^+ M^+\gamma_1^+ \\ M^-(\alpha^- + \gamma_1^-) & M^-(\alpha^- + \gamma_2^-) & M^+(\alpha^+ + \gamma_2^+) & M^+(\alpha^+ + \gamma_1^+) \\ (c_p^{\mathrm{I}})^- & (c_p^{\mathrm{II}})^- & -(c_p^{\mathrm{II}})^+ & -(c_p^{\mathrm{I}})^+ \\ (\gamma_1 c_p^{\mathrm{I}})^- & (\gamma_2 c_p^{\mathrm{II}})^- & -(\gamma_2 c_p^{\mathrm{II}})^+ & -(\gamma_1 c_p^{\mathrm{I}})^+ \end{pmatrix}$$

we obtain the following expressions:

$$\beta_1 = d_{11}\hat{\mathbf{n}}^{\mathsf{T}}(\mathbf{T}^- - \mathbf{T}^+)\hat{\mathbf{n}} + d_{12}\hat{\mathbf{n}}^{\mathsf{T}}(\mathbf{T}_{\mathrm{f}}^- - \mathbf{T}_{\mathrm{f}}^+)\hat{\mathbf{n}} + d_{13}\hat{\mathbf{n}}\cdot(\mathbf{v}_{\mathrm{s}}^- - \mathbf{v}_{\mathrm{s}}^+) + d_{14}\hat{\mathbf{n}}\cdot(\mathbf{v}_{\mathrm{f}}^- - \mathbf{v}_{\mathrm{f}}^+) \tag{92}$$

$$\beta_3 = d_{21}\hat{\mathbf{n}}^{\mathsf{T}}(\mathbf{T}^- - \mathbf{T}^+)\hat{\mathbf{n}} + d_{22}\hat{\mathbf{n}}^{\mathsf{T}}(\mathbf{T}_{\mathrm{f}}^- - \mathbf{T}_{\mathrm{f}}^+)\hat{\mathbf{n}} + d_{23}\hat{\mathbf{n}}\cdot(\mathbf{v}_{\mathrm{s}}^- - \mathbf{v}_{\mathrm{s}}^+) + d_{24}\hat{\mathbf{n}}\cdot(\mathbf{v}_{\mathrm{f}}^- - \mathbf{v}_{\mathrm{f}}^+) \tag{93}$$

$$\beta_6 = d_{31}\hat{\mathbf{n}}^{\mathsf{T}}(\mathbf{T}^- - \mathbf{T}^+)\hat{\mathbf{n}} + d_{32}\hat{\mathbf{n}}^{\mathsf{T}}(\mathbf{T}_{\mathrm{f}}^- - \mathbf{T}_{\mathrm{f}}^+)\hat{\mathbf{n}} + d_{33}\hat{\mathbf{n}}\cdot(\mathbf{v}_{\mathrm{s}}^- - \mathbf{v}_{\mathrm{s}}^+) + d_{34}\hat{\mathbf{n}}\cdot(\mathbf{v}_{\mathrm{f}}^- - \mathbf{v}_{\mathrm{f}}^+) \tag{94}$$

$$\beta_8 = d_{41}\hat{\mathbf{n}}^{\mathsf{T}}(\mathbf{T}^- - \mathbf{T}^+)\hat{\mathbf{n}} + d_{42}\hat{\mathbf{n}}^{\mathsf{T}}(\mathbf{T}_{\mathrm{f}}^- - \mathbf{T}_{\mathrm{f}}^+)\hat{\mathbf{n}} + d_{43}\hat{\mathbf{n}}\cdot(\mathbf{v}_{\mathrm{s}}^- - \mathbf{v}_{\mathrm{s}}^+) + d_{44}\hat{\mathbf{n}}\cdot(\mathbf{v}_{\mathrm{f}}^- - \mathbf{v}_{\mathrm{f}}^+) \tag{95}$$

Here the d_{ij} are the entries of the inverse of the coefficient matrix above.

Now we deal with the shear waves. Using the continuity condition (69) with the identity (62)

$$2\mu_{\mathrm{fr}}^-\hat{\mathbf{s}}^{\mathsf{T}}\mathbf{E}^c\hat{\mathbf{n}} = 2\mu_{\mathrm{fr}}^+\hat{\mathbf{s}}^{\mathsf{T}}\mathbf{E}^d\hat{\mathbf{n}}. \tag{96}$$

Substituting for $\mathbf{E}^c$ and $\mathbf{E}^d$ using (73) and (81)

$$(\mu_{\mathrm{fr}})^-\beta_2 + (\mu_{\mathrm{fr}})^+\beta_7 = \hat{\mathbf{s}}^{\mathsf{T}}(\mathbf{T}^- - \mathbf{T}^+)\hat{\mathbf{n}}. \tag{97}$$

Finally using (66), (76) and (84) gives

$$(c_s)^-\beta_2 - (c_s)^+\beta_7 = \hat{\mathbf{s}}\cdot(\mathbf{v}_{\mathrm{s}}^- - \mathbf{v}_{\mathrm{s}}^+). \tag{98}$$

Therefore,

$$\beta_2 = \frac{(c_s)^+\hat{\mathbf{s}}^{\mathsf{T}}(\mathbf{T}^- - \mathbf{T}^+)\hat{\mathbf{n}} + \mu_{\mathrm{fr}}^+\hat{\mathbf{s}}\cdot(\mathbf{v}_{\mathrm{s}}^- - \mathbf{v}_{\mathrm{s}}^+)}{(c_s)^+(\mu_{\mathrm{fr}})^- + (c_s)^-(\mu_{\mathrm{fr}})^+} \tag{99}$$

$$\beta_7 = \frac{(c_s)^-\hat{\mathbf{s}}^{\mathsf{T}}(\mathbf{T}^- - \mathbf{T}^+)\hat{\mathbf{n}} - \mu_{\mathrm{fr}}^-\hat{\mathbf{s}}\cdot(\mathbf{v}_{\mathrm{s}}^- - \mathbf{v}_{\mathrm{s}}^+)}{(c_s)^+(\mu_{\mathrm{fr}})^- + (c_s)^-(\mu_{\mathrm{fr}})^+}. \tag{100}$$

3.5. Upwind numerical flux

We define an upwind numerical flux $(\Pi\mathbf{q})^*$ along $\hat{\mathbf{n}}$ by

$$(\Pi\mathbf{q})^* = \Pi^-\mathbf{q}^- + Q^-(\beta_1(c_p^{\mathrm{I}})^-\mathbf{r}_1^- + \beta_2(c_s)^-\mathbf{r}_2^- + \beta_3(c_p^{\mathrm{II}})^-\mathbf{r}_3^-). \tag{101}$$

We now compute the $\beta_i\mathbf{r}_i$ terms. First, noting that $\mathbf{r}_i = L\mathbf{r}_i'$, a simple computation gives

$$\mathbf{r}_1^- = \begin{pmatrix} \hat{n}_1^2 \\ \hat{n}_2^2 \\ \hat{n}_1\hat{n}_2 \\ -\gamma_1^- \\ (c_p^{\mathrm{I}})^-\hat{n}_1 \\ (c_p^{\mathrm{I}})^-\hat{n}_2 \\ \gamma_1^-(c_p^{\mathrm{I}})^-\hat{n}_1 \\ \gamma_1^-(c_p^{\mathrm{I}})^-\hat{n}_2 \end{pmatrix}, \quad \mathbf{r}_2^- = \begin{pmatrix} \hat{n}_1\hat{s}_1 \\ \hat{n}_2\hat{s}_2 \\ \frac{1}{2}(\hat{n}_1\hat{s}_2 + \hat{n}_2\hat{s}_1) \\ 0 \\ (c_s)^-\hat{s}_1 \\ (c_s)^-\hat{s}_2 \\ -\frac{(c_s)^-\rho_{\mathrm{f}}^-}{m^-}\hat{s}_1 \\ -\frac{(c_s)^-\rho_{\mathrm{f}}^-}{m^-}\hat{s}_2 \end{pmatrix}, \quad \mathbf{r}_3^- = \begin{pmatrix} \hat{n}_1^2 \\ \hat{n}_2^2 \\ \hat{n}_1\hat{n}_2 \\ -\gamma_2^- \\ (c_p^{\mathrm{II}})^-\hat{n}_1 \\ (c_p^{\mathrm{II}})^-\hat{n}_2 \\ \gamma_2^-(c_p^{\mathrm{II}})^-\hat{n}_1 \\ \gamma_2^-(c_p^{\mathrm{II}})^-\hat{n}_2 \end{pmatrix}$$

where $\hat{\mathbf{n}} = (\hat{n}_1, \hat{n}_2)^\mathsf{T}$ and $\hat{\mathbf{s}} = (\hat{s}_1, \hat{s}_2)^\mathsf{T}$. In what follows, we make multiple use of the simple vector identity

$$\mathbf{a} = (\hat{\mathbf{s}}^\mathsf{T}\mathbf{a})\hat{\mathbf{s}} + (\hat{\mathbf{n}}^\mathsf{T}\mathbf{a})\hat{\mathbf{n}}.$$

We define

$$\begin{aligned}
[\![\mathbf{T}]\!] &= \mathbf{T}^-\hat{\mathbf{n}}^- + \mathbf{T}^+\hat{\mathbf{n}}^+ \\
[\![\mathbf{T}_\mathrm{f}]\!] &= \mathbf{T}_\mathrm{f}^-\hat{\mathbf{n}}^- + \mathbf{T}_\mathrm{f}^+\hat{\mathbf{n}}^+ \\
[\![\mathbf{v}]\!] &= \hat{\mathbf{n}}^{-\mathsf{T}}\mathbf{v}^- + \hat{\mathbf{n}}^{+\mathsf{T}}\mathbf{v}^+ \\
[\mathbf{v}] &= \mathbf{v}^- - \mathbf{v}^+
\end{aligned}$$

For the fast P-wave term we have

$$\beta_1(c_p^\mathrm{I})^-\mathbf{r}_1^- = (c_p^\mathrm{I})^-(d_{11}\hat{\mathbf{n}}^\mathsf{T}[\![\mathbf{T}]\!] + d_{12}\hat{\mathbf{n}}^\mathsf{T}[\![\mathbf{T}_\mathrm{f}]\!] + d_{13}[\![\mathbf{v}_\mathrm{s}]\!] + d_{14}[\![\mathbf{v}_\mathrm{f}]\!]) \times \begin{pmatrix} \hat{n}_1^2 \\ \hat{n}_2^2 \\ \hat{n}_1\hat{n}_2 \\ -\gamma_1^- \\ (c_p^\mathrm{I})^-\hat{n}_1 \\ (c_p^\mathrm{I})^-\hat{n}_2 \\ (\gamma_1 c_p^\mathrm{I})^-\hat{n}_1 \\ (\gamma_1 c_p^\mathrm{I})^-\hat{n}_2 \end{pmatrix}. \tag{102}$$

For the S-wave term we have

$$\beta_2 c_s^- \mathbf{r}_2^- = \frac{1}{(c_s)^+(\mu_{\rm fr})^- + (c_s)^-(\mu_{\rm fr})^+} \times \left\{ (c_s)^-(c_s)^+ \begin{pmatrix} \hat{n}_1([\![\mathbf{T}]\!]_1 - \hat{\mathbf{n}}^{\mathsf{T}}[\![\mathbf{T}]\!]\hat{n}_1) \\ \hat{n}_2([\![\mathbf{T}]\!]_2 - \hat{\mathbf{n}}^{\mathsf{T}}[\![\mathbf{T}]\!]\hat{n}_2) \\ \frac{\hat{n}_1}{2}([\![\mathbf{T}]\!]_2 - \hat{\mathbf{n}}^{\mathsf{T}}[\![\mathbf{T}]\!]\hat{n}_2) + \frac{\hat{n}_2}{2}([\![\mathbf{T}]\!]_1 - \hat{\mathbf{n}}^{\mathsf{T}}[\![\mathbf{T}]\!]\hat{n}_1) \\ 0 \\ (c_s)^-([\![\mathbf{T}]\!]_1 - \hat{\mathbf{n}}^{\mathsf{T}}[\![\mathbf{T}]\!]\hat{n}_1) \\ (c_s)^-([\![\mathbf{T}]\!]_2 - \hat{\mathbf{n}}^{\mathsf{T}}[\![\mathbf{T}]\!]\hat{n}_2) \\ -\frac{(c_s)^-\rho_{\rm f}^-}{m^-}([\![\mathbf{T}]\!]_1 - \hat{\mathbf{n}}^{\mathsf{T}}[\![\mathbf{T}]\!]\hat{n}_1) \\ -\frac{(c_s)^-\rho_{\rm f}^-}{m^-}([\![\mathbf{T}]\!]_2 - \hat{\mathbf{n}}^{\mathsf{T}}[\![\mathbf{T}]\!]\hat{n}_2) \end{pmatrix} \right. \\ \left. + (c_s)^-\mu_{\rm fr}^+ \begin{pmatrix} \hat{n}_1([\mathbf{v}_{\rm s}]_1 - [\![\mathbf{v}_{\rm s}]\!]\hat{n}_1) \\ \hat{n}_2[\mathbf{v}_{\rm s}]_2 - [\![\mathbf{v}_{\rm s}]\!]\hat{n}_2) \\ \frac{\hat{n}_1}{2}([\mathbf{v}_{\rm s}]_2 - [\![\mathbf{v}_{\rm s}]\!]\hat{n}_2) + \frac{\hat{n}_2}{2}([\mathbf{v}_{\rm s}]_1 - [\![\mathbf{v}_{\rm s}]\!]\hat{n}_1) \\ 0 \\ (c_s)^-([\mathbf{v}_{\rm s}]_1 - [\![\mathbf{v}_{\rm s}]\!]\hat{n}_1) \\ (c_s)^-([\mathbf{v}_{\rm s}]_2 - [\![\mathbf{v}_{\rm s}]\!]\hat{n}_2) \\ -\frac{(c_s)^-\rho_{\rm f}^-}{m^-}([\mathbf{v}_{\rm s}]_1 - [\![\mathbf{v}_{\rm s}]\!]\hat{n}_1) \\ -\frac{(c_s)^-\rho_{\rm f}^-}{m^-}([\mathbf{v}_{\rm s}]_2 - [\![\mathbf{v}_{\rm s}]\!]\hat{n}_2) \end{pmatrix} \right\} \quad (103)$$

Finally for the slow P-wave we have

$$\beta_3 (c_p^{\rm II})^- \mathbf{r}_1^- = (c_p^{\rm II})^-(d_{21}\hat{\mathbf{n}}^{\mathsf{T}}[\![\mathbf{T}]\!] + d_{22}\hat{\mathbf{n}}^{\mathsf{T}}[\![\mathbf{T}_{\rm f}]\!] + d_{23}[\![\mathbf{v}_{\rm s}]\!] + d_{24}[\![\mathbf{v}_{\rm f}]\!]) \times \begin{pmatrix} \hat{n}_1^2 \\ \hat{n}_2^2 \\ \hat{n}_1\hat{n}_2 \\ -\gamma_2^- \\ (c_p^{\rm II})^-\hat{n}_1 \\ (c_p^{\rm II})^-\hat{n}_2 \\ (\gamma_2 c_p^{\rm II})^-\hat{n}_1 \\ (\gamma_2 c_p^{\rm II})^-\hat{n}_2 \end{pmatrix}. \quad (104)$$

4. Consideration of poro-viscoelasticity

4.1. Introduction

The low-frequency regime is straightforward and follows Biot's 1956 paper [7]. Using the conventions of equations (7) and (8), the low-frequency dissipative regime is modelled by the term $\frac{\eta}{k}\frac{\partial \mathbf{w}}{\partial t}$. For the hyperbolic system (27) we simply add the source term (31). We note that in certain physical situations (when the permeability of the solid matrix is very small and the frequency content of the propagating

wave very low) the second P-wave can be essentially static and highly diffusive (so has a characteristic timescale much smaller than the time step of the non-dissipative hyperbolic system), rendering the system stiff and requiring extremely small time steps in an explicit scheme to capture the dissipative effects. This is considered by Carcione and Quiroga-Goode in [47] who used an operator splitting approach to avoid this issue and treated the viscous dissipation term analytically. In a more recent paper Lemoine et al. [13] work in a finite volume setting and again implement an operator splitting on the dissipative part. We refer to Section 3 of their paper for a detailed discussion. In this paper we use an implicit-explict (IMEX) scheme to deal with an extreme case of very small permeability, see 6.1.1.

We have had trouble understanding the various treatments of the viscous high-frequency dissipative regime [14, 11, 43]. Since, in applications to groundwater tomography, due to the relatively large permeabilities of aquifers, one often has to work in the high-frequency regime, this takes on a particular significance for us. On the one hand there appears to be a lack of consistency with the modelling of the high frequency viscodynamic operator. Morency and Tromp [11] state that they consider a high-frequency viscodynamic operator of the form $b * \dfrac{\partial \mathbf{w}}{\partial t}$ where b is given in terms of a relaxation function (see below), although we have been unable to follow the derivations in Section 8.3.2 of their paper, nor the implementation in the SPECFEM2D code, which we have used extensively; whereas de la Puente [14] considers the convolution with acceleration $\dfrac{\eta}{k}\dfrac{\partial^2 \mathbf{w}}{\partial t^2}$, which has the merit of being dimensionally consistent, and is the convention we adopt here. However, as Carcione points out in [43] the modelling of the high-frequency regime is purely phenomenological. In a personal communication Professor Carcione confirmed that his development is based on $\dfrac{\eta}{k}\dfrac{\partial^2 \mathbf{w}}{\partial t^2}$; see Section (7.17) in [43].

4.2. High-frequency case

In the high-frequency case the term $\dfrac{\eta}{k}\dfrac{\partial \mathbf{w}}{\partial t}$ in equation (8) is replaced by a convolution $b * \dfrac{\partial^2 \mathbf{w}}{\partial t^2}$ where $b(t) = \frac{\eta}{k}\Psi(t)H(t)$, $\Psi(t)$ is a relaxation function of the form

$$\Psi(t) = 1 + \sum_{l=1}^{L} \left(\frac{\tau_\epsilon^l}{\tau_\sigma^l} - 1 \right) e^{-t/\tau_\sigma^l} \tag{105}$$

with relaxation times τ_ϵ and τ_σ, and $H(t)$ is a Heaviside function. Thus the relaxation mechanism corresponds to a generalised Zener model; see [43]. In practice it is common to deal with a single Zener model, which is the case we deal with here. We have

$$b * \frac{\partial \mathbf{v}_\mathrm{f}}{\partial t} = \frac{\eta}{k} \int_{-\infty}^{t} \Psi(t-\tau) \frac{\partial \mathbf{v}_\mathrm{f}}{\partial \tau} d\tau \tag{106}$$

$$= \frac{\eta}{k} \int_{-\infty}^{t} \frac{\partial \mathbf{v}_\mathrm{f}}{\partial \tau} d\tau + \frac{\eta}{k} \sum_{l=1}^{L} \left(\frac{\tau_\epsilon^l}{\tau_\sigma^l} - 1 \right) \int_{-\infty}^{t} e^{-(t-\tau)/\tau_\sigma^l} \frac{\partial \mathbf{v}_\mathrm{f}}{\partial \tau} d\tau \tag{107}$$

$$= \frac{\eta}{k} \mathbf{v}_\mathrm{f} + \frac{\eta}{k} \sum_{l=1}^{L} \left(\frac{\tau_\epsilon^l}{\tau_\sigma^l} - 1 \right) \int_{-\infty}^{t} e^{-(t-\tau)/\tau_\sigma^l} \frac{\partial \mathbf{v}_\mathrm{f}}{\partial \tau} d\tau \tag{108}$$

We now introduce memory variables

$$\mathbf{e}^l = \left(\frac{\tau_\epsilon^l}{\tau_\sigma^l} - 1\right) \int_{-\infty}^{t} e^{-(t-\tau)/\tau_\sigma^l} \frac{\partial \mathbf{v}_\mathrm{f}}{\partial \tau} d\tau. \tag{109}$$

A straightforward calculation show that we have an additional $2L$ differential equations:

$$\frac{\partial \mathbf{e}^l}{\partial t} = \left(\frac{\tau_\epsilon^l}{\tau_\sigma^l} - 1\right) \frac{\partial \mathbf{v}_\mathrm{f}}{\partial t} - \frac{\mathbf{e}^l}{\tau_\sigma^l} \tag{110}$$

and

$$b * \frac{\partial \mathbf{v}_\mathrm{f}}{\partial t} = \frac{\eta}{k} \mathbf{v}_\mathrm{f} + \frac{\eta}{k} \sum_{l=1}^{L} \mathbf{e}^l. \tag{111}$$

It is customary to express the relaxation times in terms of a quality factor Q_0 and a reference frequency f_0 as

$$\tau_\epsilon = (\sqrt{Q_0^2 + 1} + 1)/(2\pi f_0 Q_0) \tag{112}$$

$$\tau_\sigma = (\sqrt{Q_0^2 + 1} - 1)/(2\pi f_0 Q_0). \tag{113}$$

For $L = 1$ the variable $\mathbf{q}$ defined in (22) must now be augmented with two additional variables e_x^1, e_y^1:

$$\mathbf{q} = (\epsilon_{11}, \epsilon_{22}, \epsilon_{12}, \zeta, u_\mathrm{s}, v_\mathrm{s}, u_\mathrm{f}, v_\mathrm{f}, e_x^1, e_y^1)^\mathsf{T} \tag{114}$$

and the various coefficient matrices inflated in an obvious manner.

Implementation of the high-frequency case needs to be carried out some care. Solving the ten-variable system as an inflated hyperbolic system results in a memory variable that converges to zero very quickly. An accurate scheme is obtained by treating the memory equations (110) as an uncoupled system of ordinary differential equations and evaluating $\dfrac{\partial \mathbf{v}_\mathrm{f}}{\partial t}$ from its gradient and flux terms.

5. Elastic/poroelastic coupling

In many applications to geophysics, one is interested in coupling elastic and poroelastic wave propagation; see [9, 10]. In this section we outline the DG discretisation for two-dimensional elastic waves, again for a velocity/strain formulation. The derivation is essentially the same as the poroelastic case except that the details are somewhat more straightforward since one does not have to deal with the splitting into fast and slow P-waves. For three-dimensional waves a complete account has been given in [17]. In the two-dimensional setting the only difference is one in detail in the final assembly of the numerical flux. To avoid unnecessary repetition our derivations in this section are given with brevity.

Expressed as a second-order system the elastic wave equation takes the form

$$\rho_\mathrm{e} \frac{\partial^2 \mathbf{u}_\mathrm{e}}{\partial t^2} = \nabla \cdot \mathbf{S} \tag{115}$$

where ρ_e is density and $\mathbf{S}$ is a stress tensor. In the isotropic case we consider here $\mathbf{S}$ may be written in the usual form

$$\mathbf{S} = 2\mu_e \mathbf{E} + \lambda_e \,\mathrm{trace}(\mathbf{E})\mathbf{I} \tag{116}$$

where $\mathbf{E}$ is the solid strain tensor and μ_e and λ_e are Lamé coefficients. Expressed as a first-order hyperbolic system with variable

$$\mathbf{q}_e = (\epsilon_{11}, \epsilon_{22}, \epsilon_{12}, u_e, v_e)^\mathsf{T} \tag{117}$$

where $\mathbf{v}_e = (u_e, v_e)$ are the x and y components of the velocity $\dfrac{\partial \mathbf{u}_e}{\partial t}$ gives

$$Q_e \frac{\partial \mathbf{q}}{\partial t} + \nabla \cdot \mathcal{F}_e = Q_e \frac{\partial \mathbf{q}}{\partial t} + \frac{\partial (A_e \mathbf{q})}{\partial x} + \frac{\partial (B_e \mathbf{q})}{\partial y} = 0 \tag{118}$$

where

$$\mathcal{F}_e = [F_1, F_2] = [A_e \mathbf{q}, B_e \mathbf{q}],$$

and

$$Q_e = \begin{pmatrix} 1 & 0 & 0 & 0 & 0 \\ 0 & 1 & 0 & 0 & 0 \\ 0 & 0 & 1 & 0 & 0 \\ 0 & 0 & 0 & \rho_e & 0 \\ 0 & 0 & 0 & 0 & \rho_e \end{pmatrix}. \tag{119}$$

The Jacobian matrices A and B are given by

$$A_e = -\begin{pmatrix} 0 & 0 & 0 & 1 & 0 \\ 0 & 0 & 0 & 0 & 0 \\ 0 & 0 & 0 & 0 & 1/2 \\ 2\mu_e + \lambda_e & \lambda_e & 0 & 0 & 0 \\ 0 & 0 & 2\mu_e & 0 & 0 \end{pmatrix}, \tag{120}$$

and

$$B_e = -\begin{pmatrix} 0 & 0 & 0 & 0 & 0 \\ 0 & 0 & 0 & 0 & 1 \\ 0 & 0 & 0 & 1/2 & 0 \\ 0 & 0 & 2\mu_e & 0 & 0 \\ \lambda_e & 2\mu_e + \lambda_e & 0 & 0 & 0 \end{pmatrix}. \tag{121}$$

Writing $\Lambda_e = \mathrm{diag}(-c_p, -c_s, 0, c_s, c_p)$ we have the well-known expressions for elastic wave speeds

$$c_p = \sqrt{\frac{\lambda_e + 2\mu_e}{\rho_e}} \quad \text{and} \quad c_s = \sqrt{\frac{\mu_e}{\rho_e}}. \tag{122}$$

Moreover, we have the spectral decomposition $A_e = R_e \Lambda R_e^{-1}$ where R_e is a matrix of representative eigenvectors

$$R_e = \begin{pmatrix} 1 & 0 & -\lambda_{\mathrm{e}} & 0 & 1 \\ 0 & 0 & 2\mu_{\mathrm{e}} + \lambda_{\mathrm{e}} & 0 & 0 \\ 0 & 1/2 & 0 & 1/2 & 0 \\ c_p & 0 & 0 & 0 & -c_p \\ 0 & c_s & 0 & -c_s & 0 \end{pmatrix}. \tag{123}$$

Solving the Riemann problem as before we obtain the following coefficients corresponding to the non-zero wave speeds

$$\beta_1 = \frac{(c_p)^+ \hat{\mathbf{n}}^{\mathsf{T}} (\mathbf{S}^- - \mathbf{S}^+) \hat{\mathbf{n}} + (\lambda_{\mathrm{e}}^+ + 2\mu_{\mathrm{e}}^+) \hat{\mathbf{n}} \cdot (\mathbf{v}_{\mathrm{e}}^- - \mathbf{v}_{\mathrm{e}}^+)}{(c_p)^+ (\lambda_{\mathrm{e}}^- + 2\mu_{\mathrm{e}}^-) + (c_p)^- (\lambda_{\mathrm{e}}^+ + 2\mu_{\mathrm{e}}^+)} \tag{124}$$

$$\beta_2 = \frac{(c_s)^+ \hat{\mathbf{s}}^{\mathsf{T}} (\mathbf{S}^- - \mathbf{S}^+) \hat{\mathbf{n}} + \mu_{\mathrm{e}}^+ \hat{\mathbf{s}} \cdot (\mathbf{v}_{\mathrm{e}}^- - \mathbf{v}_{\mathrm{e}}^+)}{(c_s)^+ (\mu_{\mathrm{e}})^- + (c_s)^- (\mu_{\mathrm{e}})^+} \tag{125}$$

$$\beta_4 = \frac{(c_s)^- \hat{\mathbf{s}}^{\mathsf{T}} (\mathbf{S}^- - \mathbf{S}^+) \hat{\mathbf{n}} - \mu_{\mathrm{e}}^- \hat{\mathbf{s}} \cdot (\mathbf{v}_{\mathrm{e}}^- - \mathbf{v}_{\mathrm{e}}^+)}{(c_s)^+ (\mu_{\mathrm{e}})^- + (c_s)^- (\mu_{\mathrm{e}})^+} \tag{126}$$

$$\beta_5 = \frac{(c_p)^- \hat{\mathbf{n}}^{\mathsf{T}} (\mathbf{S}^- - \mathbf{S}^+) \hat{\mathbf{n}} - (\lambda_{\mathrm{e}}^- + 2\mu_{\mathrm{e}}^-) \hat{\mathbf{n}} \cdot (\mathbf{v}_{\mathrm{e}}^- - \mathbf{v}_{\mathrm{e}}^+)}{(c_p)^+ (\lambda_{\mathrm{e}}^- + 2\mu_{\mathrm{e}}^-) + (c_p)^- (\lambda_{\mathrm{e}}^+ + 2\mu_{\mathrm{e}}^+)}. \tag{127}$$

Defining an upwind numerical flux $(\Pi \mathbf{q})^*$ along $\hat{\mathbf{n}}$ by

$$(\Pi \mathbf{q})^* = \Pi^- \mathbf{q}^- + Q^- (\beta_1 (c_p)^- \mathbf{r}_1^- + \beta_2 (c_s)^- \mathbf{r}_2^-) \tag{128}$$

where

$$\mathbf{r}_1^- = \begin{pmatrix} \hat{n}_1^2 \\ \hat{n}_2^2 \\ \hat{n}_1 \hat{n}_2 \\ (c_p)^- \hat{n}_1 \\ (c_p)^- \hat{n}_2 \end{pmatrix}, \quad \mathbf{r}_2^- = \begin{pmatrix} \hat{n}_1 \hat{s}_1 \\ \hat{n}_2 \hat{s}_2 \\ \frac{1}{2}(\hat{n}_1 \hat{s}_2 + \hat{n}_2 \hat{s}_1) \\ (c_s)^- \hat{s}_1 \\ (c_s)^- \hat{s}_2 \end{pmatrix},$$

and $\hat{\mathbf{n}} = (\hat{n}_1, \hat{n}_2)^{\mathsf{T}}$ and $\hat{\mathbf{s}} = (\hat{s}_1, \hat{s}_2)^{\mathsf{T}}$. We define

$$[\![\mathbf{S}]\!] = \mathbf{S}^- \hat{\mathbf{n}}^- + \mathbf{S}^+ \hat{\mathbf{n}}^+$$
$$[\![\mathbf{v}_{\mathrm{e}}]\!] = \hat{\mathbf{n}}^{-\mathsf{T}} \mathbf{v}_{\mathrm{e}}^- + \hat{\mathbf{n}}^{+\mathsf{T}} \mathbf{v}_{\mathrm{e}}^+$$
$$[\mathbf{v}_{\mathrm{e}}] = \mathbf{v}_{\mathrm{e}}^- - \mathbf{v}_{\mathrm{e}}^+.$$

Assembling the flux terms corresponding to P- and S- waves we obtain respectively

$$\beta_1 (c_p)^- \mathbf{r}_1^- = \frac{(c_p)^- c_p^+ \hat{\mathbf{n}}^\mathsf{T} [\![\mathbf{S}]\!] + (c_p)^- (\lambda_\mathrm{e}^+ + 2\mu_\mathrm{e}^+) [\![\mathbf{v}_\mathrm{e}]\!]}{c_p^+ (\lambda_\mathrm{e}^- + 2\mu_\mathrm{e}^-) + c_p^- (\lambda_\mathrm{e}^+ + 2\mu_\mathrm{e}^+)} \times \begin{pmatrix} \hat{n}_1^2 \\ \hat{n}_2^2 \\ \hat{n}_1 \hat{n}_2 \\ (c_p)^- \hat{n}_1 \\ (c_p)^- \hat{n}_2 \end{pmatrix} \tag{129}$$

and

$$\beta_2 c_s^- \mathbf{r}_2^- = \frac{1}{(c_s)^+ (\mu_\mathrm{e})^- + (c_s)^- (\mu_\mathrm{e})^+} \times \left\{ (c_s)^- (c_s)^+ \begin{pmatrix} \hat{n}_1 ([\![\mathbf{S}]\!]_1 - \hat{\mathbf{n}}^\mathsf{T} [\![\mathbf{S}]\!] \hat{n}_1) \\ \hat{n}_2 ([\![\mathbf{S}]\!]_2 - \hat{\mathbf{n}}^\mathsf{T} [\![\mathbf{S}]\!] \hat{n}_2) \\ \frac{\hat{n}_1}{2} ([\![\mathbf{S}]\!]_2 - \hat{\mathbf{n}}^\mathsf{T} [\![\mathbf{S}]\!] \hat{n}_2) + \frac{\hat{n}_2}{2} ([\![\mathbf{S}]\!]_1 - \hat{\mathbf{n}}^\mathsf{T} [\![\mathbf{S}]\!] \hat{n}_1) \\ (c_s)^- ([\![\mathbf{S}]\!]_1 - \hat{\mathbf{n}}^\mathsf{T} [\![\mathbf{S}]\!] \hat{n}_1) \\ (c_s)^- ([\![\mathbf{S}]\!]_2 - \hat{\mathbf{n}}^\mathsf{T} [\![\mathbf{S}]\!] \hat{n}_2) \end{pmatrix} \right. \\ \left. + (c_s)^- \mu_\mathrm{e}^+ \begin{pmatrix} \hat{n}_1 ([\mathbf{v}_\mathrm{e}]_1 - [\![\mathbf{v}_\mathrm{e}]\!] \hat{n}_1) \\ \hat{n}_2 ([\mathbf{v}_\mathrm{e}]_2 - [\![\mathbf{v}_\mathrm{e}]\!] \hat{n}_2) \\ \frac{\hat{n}_1}{2} ([\mathbf{v}_\mathrm{e}]_2 - [\![\mathbf{v}_\mathrm{e}]\!] \hat{n}_2) + \frac{\hat{n}_2}{2} ([\mathbf{v}_\mathrm{e}]_1 - [\![\mathbf{v}_\mathrm{e}]\!] \hat{n}_1) \\ (c_s)^- ([\mathbf{v}_\mathrm{e}]_1 - [\![\mathbf{v}_\mathrm{e}]\!] \hat{n}_1) \\ (c_s)^- ([\mathbf{v}_\mathrm{e}]_2 - [\![\mathbf{v}_\mathrm{e}]\!] \hat{n}_2) \end{pmatrix} \right\} \tag{130}$$

5.1. Elastic/poroelastic interface

The interface between an elastic and poroelastic medium needs to be treated with some care. In principle, it is possible to work entirely within a poroelastic framework and take the limit as $\phi \to 0$ but this is somewhat cumbersome. We prefer here to solve a Riemann problem at the interface subject to the following flux continuity conditions at the interface:

$$\hat{\mathbf{n}} \cdot \mathbf{v}_\mathrm{e}^b = \hat{\mathbf{n}} \cdot \mathbf{v}_\mathrm{s}^c \tag{131}$$

$$\hat{\mathbf{s}} \cdot \mathbf{v}_\mathrm{e}^b = \hat{\mathbf{s}} \cdot \mathbf{v}_\mathrm{s}^c \tag{132}$$

$$0 = \hat{\mathbf{n}} \cdot \mathbf{v}_\mathrm{f}^c \tag{133}$$

$$\hat{\mathbf{n}}^\mathsf{T} \mathbf{S}^b \hat{\mathbf{n}} = \hat{\mathbf{n}}^\mathsf{T} \mathbf{T}^c \hat{\mathbf{n}} \tag{134}$$

$$\hat{\mathbf{s}}^\mathsf{T} \mathbf{S}^b \hat{\mathbf{n}} = \hat{\mathbf{s}}^\mathsf{T} \mathbf{T}^c \hat{\mathbf{n}} \tag{135}$$

where we now have 7 unknown states shown in Figure 2.

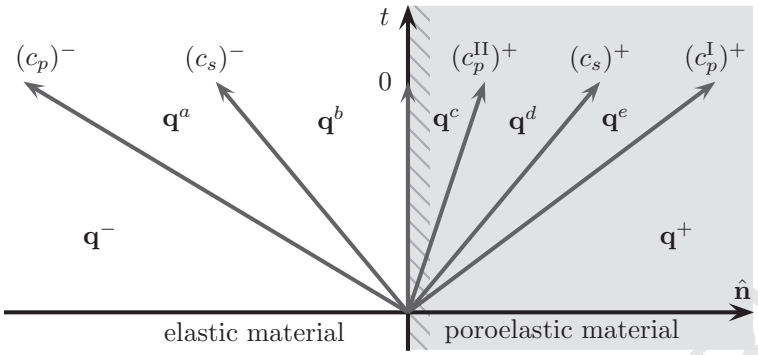

Figure 2: Schematic showing characteristic wave speeds at an elastic/poroelastic interface between two states $\mathbf{q}^-$ (elastic) and $\mathbf{q}^+$ (poroelastic). $\mathbf{q}^a$– $\mathbf{q}^e$ denote the intermediate states.

195 Note that the normal fluid and solid velocities in the poroelastic medium are assumed to be the same as the solid velocity in the elastic medium at the interface. From the Rankine-Hugoniot conditions we obtain

$$\mathbf{q}^- - \mathbf{q}^a = \beta_1^e \mathbf{r}_1^e \tag{136}$$

$$\mathbf{q}^a - \mathbf{q}^b = \beta_2^e \mathbf{r}_2^e \tag{137}$$

$$\mathbf{q}^c - \mathbf{q}^d = \beta_6^p \mathbf{r}_6^p \tag{138}$$

$$\mathbf{q}^d - \mathbf{q}^e = \beta_7^p \mathbf{r}_7^p \tag{139}$$

$$\mathbf{q}^e - \mathbf{q}^- = \beta_8^p \mathbf{r}_8^p \tag{140}$$

where $\mathbf{r}_j^e$ is an eigenvector for the elastic domain and $\mathbf{r}_j^p$ is an eigenvector for the poroelastic domain corresponding to wave speeds $c_j^{\pm}$ and hence

$$\mathbf{q}^- - \mathbf{q}^c = \beta_1^e \mathbf{r}_1^e + \beta_2^e \mathbf{r}_2^e \tag{141}$$

$$\mathbf{q}^c - \mathbf{q}^+ = \beta_6^p \mathbf{r}_6^p + \beta_7^p \mathbf{r}_7^p + \beta_8^p \mathbf{r}_8^p. \tag{142}$$

Using (131), (133) and (134) we obtain

$$(c_p^e)^- \beta_1^e - (c_p^{\mathrm{II}})^+ \beta_6^p - (c_p^{\mathrm{I}})^+ \beta_8^p = \hat{\mathbf{n}} \cdot (\mathbf{v}_{\mathrm{e}}^- - \mathbf{v}_{\mathrm{s}}^+) \tag{143}$$

$$(\gamma_2 c_p^{\mathrm{II}})^+ \beta_6^p + (\gamma_1 c_p^{\mathrm{I}})^+ \beta_8^p = \hat{\mathbf{n}} \cdot \mathbf{v}_{\mathrm{f}}^+ \tag{144}$$

$$(2\mu_{\mathrm{e}}^- + \lambda_{\mathrm{e}}^-)\beta_1^e + (2\mu_{\mathrm{fr}}^+ + \lambda^+ + \alpha^+ M^+ \gamma_2^+)\beta_6 + (2\mu_{\mathrm{fr}}^+ + \lambda^+ + \alpha^+ M^+ \gamma_1^+)\beta_8 = \hat{\mathbf{n}}^{\mathsf{T}}(\mathbf{S}^- - \mathbf{T}^+)\hat{\mathbf{n}}. \tag{145}$$

As in the poroelastic case, we invert the coefficient matrix

$$\begin{pmatrix} 2\mu_{\rm e}^- + \lambda_{\rm e}^- & 2\mu_{\rm fr}^+ + \lambda^+ + \alpha^+ M^+ \gamma_2^+ & 2\mu_{\rm fr}^+ + \lambda^+ + \alpha^+ M^+ \gamma_1^+ \\ (c_p^e)^- & -(c_p^{\rm II})^+ & -(c_p^{\rm I})^+ \\ 0 & (\gamma_2 c_p^{\rm II})^+ & (\gamma_1 c_p^{\rm I})^+ \end{pmatrix}$$

to solve for β_1^e, β_6^p and β_6^p and obtain coefficients $\tilde{d}_{ij}$ such that

$$\beta_1^e = \tilde{d}_{11}\hat{\mathbf{n}}^{\mathsf{T}}(\mathbf{S}^- - \mathbf{T}^+)\hat{\mathbf{n}} + \tilde{d}_{12}\hat{\mathbf{n}} \cdot (\mathbf{v}_{\rm e}^- - \mathbf{v}_{\rm s}^+) \ + \tilde{d}_{13}\hat{\mathbf{n}} \cdot \mathbf{v}_{\rm f}^+ \tag{146}$$

$$\beta_6^p = \tilde{d}_{21}\hat{\mathbf{n}}^{\mathsf{T}}(\mathbf{S}^- - \mathbf{T}^+)\hat{\mathbf{n}} + \tilde{d}_{22}\hat{\mathbf{n}} \cdot (\mathbf{v}_{\rm e}^- - \mathbf{v}_{\rm s}^+) \ + \tilde{d}_{23}\hat{\mathbf{n}} \cdot \mathbf{v}_{\rm f}^+ \tag{147}$$

$$\beta_8^p = \tilde{d}_{31}\hat{\mathbf{n}}^{\mathsf{T}}(\mathbf{S}^- - \mathbf{T}^+)\hat{\mathbf{n}} + \tilde{d}_{32}\hat{\mathbf{n}} \cdot (\mathbf{v}_{\rm e}^- - \mathbf{v}_{\rm s}^+) \ + \tilde{d}_{33}\hat{\mathbf{n}} \cdot \mathbf{v}_{\rm f}^+. \tag{148}$$

Finally, we deal with the shear waves. Using (132) and (135) we obtain

$$\mu_{\rm e}\beta_2^e + \mu_{\rm fr}^p \beta_7^p = \hat{\mathbf{s}}^{\mathsf{T}}(\mathbf{S}^- - \mathbf{T}^+)\hat{\mathbf{n}} \tag{149}$$

$$(c_s^e)^-\beta_2^e - (c_s^p)^+\beta_7^p = \hat{\mathbf{s}} \cdot (\mathbf{v}_{\rm e}^- - \mathbf{v}_{\rm s}^+). \tag{150}$$

Therefore,

$$\beta_2^e = \frac{(c_s^p)^+\hat{\mathbf{s}}^{\mathsf{T}}(\mathbf{S}^- - \mathbf{T}^+)\hat{\mathbf{n}} + \mu_{\rm fr}^+\hat{\mathbf{s}} \cdot (\mathbf{v}_{\rm e}^- - \mathbf{v}_{\rm f}^+)}{(c_s^p)^+(\mu_{\rm e})^- + (c_s^e)^-(\mu_{\rm fr})^+} \tag{151}$$

$$\beta_7^p = \frac{(c_s^e)^-\hat{\mathbf{s}}^{\mathsf{T}}(\mathbf{S}^- - \mathbf{T}^+)\hat{\mathbf{n}} - \mu_{\rm e}^-\hat{\mathbf{s}} \cdot (\mathbf{v}_{\rm e}^- - \mathbf{v}_{\rm s}^+)}{(c_s^p)^+(\mu_{\rm e})^- + (c_s^e)^-(\mu_{\rm fr})^+}. \tag{152}$$

5.2. Upwind numerical flux

For the interface element on the elastic domain, we define an upwind numerical flux $(\Pi\mathbf{q})^*$ along $\hat{\mathbf{n}}$ by

$$(\Pi\mathbf{q}^e)^* = \Pi^-\mathbf{q}^- + Q^-(\beta_1^e(c_p^e)^-\mathbf{r}_1^- + \beta_2^e(c_s^e)^-\mathbf{r}_2^-) \tag{153}$$

while, for the poroelastic domain, we define an upwind numerical flux $(\Pi\mathbf{q})^*$ along $\hat{\mathbf{n}}$ by

$$(\Pi\mathbf{q}^p)^* = \Pi^+\mathbf{q}^+ - Q^+(\beta_6^p(c_p^{\rm II})^+\mathbf{r}_6^+ + \beta_7^p(c_s)^+\mathbf{r}_7^+ + \beta_8^p(c_p^{\rm I})^+\mathbf{r}_8^+). \tag{154}$$

We define

$$[\![\mathbf{S}, \mathbf{T}]\!] = \mathbf{S}^-\hat{\mathbf{n}}^- + \mathbf{T}^+\hat{\mathbf{n}}^+$$

$$[\![\mathbf{v}_{\rm e}, \mathbf{v}_{\rm s}]\!] = \hat{\mathbf{n}}^{-\mathsf{T}}\mathbf{v}_{\rm e}^- + \hat{\mathbf{n}}^{+\mathsf{T}}\mathbf{v}_{\rm s}^+$$

$$[\![\mathbf{v}_{\rm f}]\!] = \hat{\mathbf{n}}^{+\mathsf{T}}\mathbf{v}_{\rm f}^+$$

$$[\mathbf{v}_{\rm e}, \mathbf{v}_{\rm s}] = \mathbf{v}_{\rm e}^- - \mathbf{v}_{\rm s}^+$$

We now assemble the flux terms for the elastic element:

$$\beta_1^e (c_p^e)^- \mathbf{r}_1^{-,e} = (c_p^e)^- (d_{11}\hat{\mathbf{n}}^\mathsf{T}[\![\mathbf{S},\mathbf{T}]\!] + d_{12}[\![\mathbf{v}_\mathrm{e},\mathbf{v}_\mathrm{s}]\!] + d_{13}[\![\mathbf{v}_\mathrm{f}]\!]) \times \begin{pmatrix} \hat{n}_1^2 \\ \hat{n}_2^2 \\ \hat{n}_1\hat{n}_2 \\ (c_p^e)^-\hat{n}_1 \\ (c_p^e)^-\hat{n}_2 \end{pmatrix} \tag{155}$$

and

$$\beta_2 c_s^- \mathbf{r}_2^- = \frac{1}{(c_s^p)^+(\mu_\mathrm{e})^- + (c_s^e)^-(\mu_\mathrm{fr})^+} \times \left\{ (c_s^e)^-(c_s)^+ \begin{pmatrix} \hat{n}_1([\![\mathbf{S},\mathbf{T}]\!]_1 - \hat{\mathbf{n}}^\mathsf{T}[\![\mathbf{S},\mathbf{T}]\!]\hat{n}_1) \\ \hat{n}_2([\![\mathbf{S},\mathbf{T}]\!]_2 - \hat{\mathbf{n}}^\mathsf{T}[\![\mathbf{S},\mathbf{T}]\!]\hat{n}_2) \\ \frac{\hat{n}_1}{2}([\![\mathbf{S},\mathbf{T}]\!]_2 - \hat{\mathbf{n}}^\mathsf{T}[\![\mathbf{S},\mathbf{T}]\!]\hat{n}_2) + \frac{\hat{n}_2}{2}([\![\mathbf{S},\mathbf{T}]\!]_1 - \hat{\mathbf{n}}^\mathsf{T}[\![\mathbf{S},\mathbf{T}]\!]\hat{n}_1) \\ (c_s)^-([\![\mathbf{S},\mathbf{T}]\!]_1 - \hat{\mathbf{n}}^\mathsf{T}[\![\mathbf{S},\mathbf{T}]\!]\hat{n}_1) \\ (c_s)^-([\![\mathbf{S},\mathbf{T}]\!]_2 - \hat{\mathbf{n}}^\mathsf{T}[\![\mathbf{S},\mathbf{T}]\!]\hat{n}_2) \end{pmatrix} \right.$$
$$\left. + (c_s^e)^-\mu_\mathrm{fr}^+ \begin{pmatrix} \hat{n}_1([\mathbf{v}_\mathrm{e},\mathbf{v}_\mathrm{s}]_1 - [\![\mathbf{v}_\mathrm{e},\mathbf{v}_\mathrm{s}]\!]\hat{n}_1) \\ \hat{n}_2([\mathbf{v}_\mathrm{e},\mathbf{v}_\mathrm{s}]_2 - [\![\mathbf{v}_\mathrm{e},\mathbf{v}_\mathrm{s}]\!]\hat{n}_2) \\ \frac{\hat{n}_1}{2}([\mathbf{v}_\mathrm{e},\mathbf{v}_\mathrm{s}]_2 - [\![\mathbf{v}_\mathrm{e},\mathbf{v}_\mathrm{s}]\!]\hat{n}_2) + \frac{\hat{n}_2}{2}([\mathbf{v}_\mathrm{e},\mathbf{v}_\mathrm{s}]_1 - [\![\mathbf{v}_\mathrm{e},\mathbf{v}_\mathrm{s}]\!]\hat{n}_1) \\ (c_s)^-([\mathbf{v}_\mathrm{e},\mathbf{v}_\mathrm{s}]_1 - [\![\mathbf{v}_\mathrm{e},\mathbf{v}_\mathrm{s}]\!]\hat{n}_1) \\ (c_s)^-([\mathbf{v}_\mathrm{e},\mathbf{v}_\mathrm{s}]_2 - [\![\mathbf{v}_\mathrm{e},\mathbf{v}_\mathrm{s}]\!]\hat{n}_2) \end{pmatrix} \right\}. \tag{156}$$

Finally, we assemble the flux terms for the poroelastic element. For the slow P-wave we have

$$\beta_6^p (c_p^\mathrm{II})^+ \mathbf{r}_6^+ = (c_p^\mathrm{II})^+ (\tilde{d}_{21}\hat{\mathbf{n}}^\mathsf{T}[\![\mathbf{S},\mathbf{T}]\!] + \tilde{d}_{22}[\![\mathbf{v}_\mathrm{e},\mathbf{v}_\mathrm{s}]\!] + \tilde{d}_{23}[\![\mathbf{v}_\mathrm{f}]\!]) \times \begin{pmatrix} \hat{n}_1^2 \\ \hat{n}_2^2 \\ \hat{n}_1\hat{n}_2 \\ -\gamma_2^+ \\ -(c_p^\mathrm{II})^+\hat{n}_1 \\ -(c_p^\mathrm{II})^+\hat{n}_2 \\ -(\gamma_2 c_p^\mathrm{II})^+\hat{n}_1 \\ -(\gamma_2 c_p^\mathrm{II})^+\hat{n}_2 \end{pmatrix}. \tag{157}$$

For the S-wave, we have

$$\beta_7^p (c_s^p)^+ \mathbf{r}_7^+ = \frac{1}{(c_s^p)^+(\mu_{\rm e})^- + (c_s^e)^-(\mu_{\rm fr})^+} \times \left\{ (c_s^e)^-(c_s^p)^+ \begin{pmatrix} \hat{n}_1([\![\mathbf{S},\mathbf{T}]\!]_1 - \hat{\mathbf{n}}^{\mathsf{T}}[\![\mathbf{S},\mathbf{T}]\!]\hat{n}_1) \\ \hat{n}_2([\![\mathbf{S},\mathbf{T}]\!]_2 - \hat{\mathbf{n}}^{\mathsf{T}}[\![\mathbf{S},\mathbf{T}]\!]\hat{n}_2) \\ \frac{\hat{n}_1}{2}([\![\mathbf{S},\mathbf{T}]\!]_2 - \hat{\mathbf{n}}^{\mathsf{T}}[\![\mathbf{S},\mathbf{T}]\!]\hat{n}_2) + \frac{\hat{n}_2}{2}([\![\mathbf{S},\mathbf{T}]\!]_1 - \hat{\mathbf{n}}^{\mathsf{T}}[\![\mathbf{S},\mathbf{T}]\!]\hat{n}_1) \\ 0 \\ -(c_s)^+([\![\mathbf{S},\mathbf{T}]\!]_1 - \hat{\mathbf{n}}^{\mathsf{T}}[\![\mathbf{S},\mathbf{T}]\!]\hat{n}_1) \\ -(c_s)^+([\![\mathbf{S},\mathbf{T}]\!]_2 - \hat{\mathbf{n}}^{\mathsf{T}}[\![\mathbf{S},\mathbf{T}]\!]\hat{n}_2) \\ \frac{(c_s)^+\rho_{\rm f}^+}{m^+}([\![\mathbf{S},\mathbf{T}]\!]_1 - \hat{\mathbf{n}}^{\mathsf{T}}[\![\mathbf{S},\mathbf{T}]\!]\hat{n}_1) \\ \frac{(c_s)^+\rho_{\rm f}^+}{m^+}([\![\mathbf{S},\mathbf{T}]\!]_2 - \hat{\mathbf{n}}^{\mathsf{T}}[\![\mathbf{S},\mathbf{T}]\!]\hat{n}_2) \end{pmatrix} \right. \\ \left. -\mu_{\rm e}^-(c_s^p)^+ \begin{pmatrix} \hat{n}_1([\mathbf{v}_{\rm e},\mathbf{v}_{\rm s}]_1 - [\![\mathbf{v}_{\rm e},\mathbf{v}_{\rm s}]\!]\hat{n}_1) \\ \hat{n}_2([\mathbf{v}_{\rm e},\mathbf{v}_{\rm s}]_2 - [\![\mathbf{v}_{\rm e},\mathbf{v}_{\rm s}]\!]\hat{n}_2) \\ \frac{\hat{n}_1}{2}([\mathbf{v}_{\rm e},\mathbf{v}_{\rm s}]_2 - [\![\mathbf{v}_{\rm e},\mathbf{v}_{\rm s}]\!]\hat{n}_2) + \frac{\hat{n}_2}{2}([\mathbf{v}_{\rm e},\mathbf{v}_{\rm s}]_1 - [\![\mathbf{v}_{\rm e},\mathbf{v}_{\rm s}]\!]\hat{n}_1) \\ 0 \\ -(c_s)^+([\mathbf{v}_{\rm e},\mathbf{v}_{\rm s}]_1 - [\![\mathbf{v}_{\rm e},\mathbf{v}_{\rm s}]\!]\hat{n}_1) \\ -(c_s)^+([\mathbf{v}_{\rm e},\mathbf{v}_{\rm s}]_2 - [\![\mathbf{v}_{\rm e},\mathbf{v}_{\rm s}]\!]\hat{n}_2) \\ \frac{(c_s)^+\rho_{\rm f}^+}{m^+}([\mathbf{v}_{\rm e},\mathbf{v}_{\rm s}]_1 - [\![\mathbf{v}_{\rm e},\mathbf{v}_{\rm s}]\!]\hat{n}_1) \\ \frac{(c_s)^+\rho_{\rm f}^+}{m^+}([\mathbf{v}_{\rm e},\mathbf{v}_{\rm s}]_2 - [\![\mathbf{v}_{\rm e},\mathbf{v}_{\rm s}]\!]\hat{n}_2) \end{pmatrix} \right\}. \quad (158)$$

Finally, for the fast P-wave, we have

$$\beta_8^p (c_p^{\rm I})^+ \mathbf{r}_8^+ = (c_p^{\rm I})^+ (\tilde{d}_{31}\hat{\mathbf{n}}^{\mathsf{T}}[\![\mathbf{S},\mathbf{T}]\!] + \tilde{d}_{32}[\![\mathbf{v}_{\rm e},\mathbf{v}_{\rm s}]\!] + \tilde{d}_{33}[\![\mathbf{v}_{\rm f}]\!]) \times \begin{pmatrix} \hat{n}_1^2 \\ \hat{n}_2^2 \\ \hat{n}_1\hat{n}_2 \\ -\gamma_1^+ \\ -(c_p^{\rm I})^+\hat{n}_1 \\ -(c_p^{\rm I})^+\hat{n}_2 \\ -(\gamma_1 c_p^{\rm I})^+\hat{n}_1 \\ -(\gamma_1 c_p^{\rm I})^+\hat{n}_2 \end{pmatrix} \quad (159)$$

6. Numerical experiments

In this section, we consider several numerical experiments. First, we consider the convergence properties of the numerical scheme, and verify that our code produces the reported convergence behaviour of the DG method (see discussion in [34] and references therein). Next, we consider several examples of heterogeneous poroelastic material and coupled poroelastic/elastic materials in Biot's low- and high-frequency regimes. We use the SPECFEM2D code as reference code (version 7.0, date: Wed Dec 10 02:43:39 2014) and show

that our code naturally handles material discontinuities, a necessary feature in applications to groundwater tomography. Another merit of our DG framework is that it permits non-uniform basis functions, so the basis order can be specified element by element. One can therefore control the accuracy both locally and globally. In the examples we specify a region of interest where we set the numerical accuracy to be at an error level 0.1%, while over the rest of the domain it is set at a 10% level. The larger domain is to avoid spurious reflections at the absorbing boundaries.

In the following simulations, the length of the time step Δt is computed from

$$\Delta t = C \left(\frac{h^\ell_{\min}}{c^\ell_{\max}(N^\ell)^2} \right)_{\min}, \quad \ell = 1, \cdots, K \tag{160}$$

where C is constant, $c^\ell_{\max}$ is the maximum wave speed, N^ℓ is the basis order, $h^\ell_{\min}$ is the smallest distance between two vertices in the element ℓ, and K is the number of elements. In the simulations, we set $C = 0.5$ except in Section 6.1.1.

6.1. Convergence analysis

Convergence tests were carried out on a square domain $\Omega = [-5,\ 5] \times [-5,\ 5]$ metres with regularly refined grids and inhomogeneous Dirichlet boundary conditions. The material parameters are given in Table 1. We consider three cases. In the first case we consider wave propagation in an inviscid setting, while the other two involve viscous flow in Biot's low- and high-frequency settings respectively. In Table 2, we list the assumed frequencies, viscosities, permeabilities, and the derived wave velocities. The frequency was set at 2,000 Hz so that the test domain captured around five wavelengths of the fast P-wave. Note that with the high-frequency case we also need to define the quality factor (see Section 4.2).

Analytic plane wave solutions consisting of fast and slow P-waves and S-waves were constructed from plane wave solutions of the form

$$\mathbf{q} = \mathbf{q}_0 e^{\mathrm{i}(k_x x + k_y y - \omega t)}$$

where $\mathrm{i} = \sqrt{-1}$, ω are frequencies, and k_x and k_y are complex wave numbers in the x- and y-directions, respectively. In the inviscid case, we consider dissipating waves of the form

$$\mathbf{q} = \mathrm{Re}\left(\sum_{p=1}^{8} \alpha_p \mathbf{r}_p e^{\mathrm{i}(k_{x,p} + k_{y,p} - \omega t)} \right)$$

where $\mathbf{r}_p$ is an eigenvector of the 8×8 matrix

$$Q^{-1}(n_x A + n_y B)$$

where n_x and n_y are direction cosines. In the reported examples, we set $k_x = k_y = 1$. For the viscous low- and high-frequency cases the wave speeds and dissipation are frequency-dependent. Formulae for the respective wave speeds and eigenvectors are given in the appendix.

Table 1: Material parameters used in the convergence analysis.

variable name	**symbol**	
solid density	ρ_{s} (kg/m^3)	2650
fluid density	ρ_{f} (kg/m^3)	900
fluid bulk modulus	κ_{f} (GPa)	2.0
frame bulk modulus	κ_{fr} (GPa)	10.0
solid bulk modulus	κ_{s} (GPa)	12.0
frame shear modulus	μ_{fr} (GPa)	5.0
tortuosity	τ	1.2
porosity	ϕ	0.3

Table 2: This table lists the plane wave frequency f_0, viscosity η, permeability k, quality factor Q_0, Biot's characteristic frequency f_c, and wave velocities $(c_p^{\mathrm{I}}, c_p^{\mathrm{II}}, c_s)$ for the three cases studied.

case	f_0 (Hz)	η (Pa·s)	k (m^2)	Q_0	f_c (Hz)	c_p^{I} (m/s)	c_p^{II} (m/s)	c_s (m/s)
inviscid	2000	0	-	-	-	2967	1411	1622
low-frequency	2000	0.001	10^{-12}	-	44209.71	2817	414	1534
high-frequency	2000	0.001	10^{-8}	30	4.42	2967	1411	1622

The numerical solver was initialised with the analytic plane wave solution at time $t = 0$, and the boundary values were set with the values of the analytic plane wave. The tests were carried out using plane waves with a fixed frequency f_0 (see Table 2). The total simulation time was taken to be $1/f_0$. The analytic and numerical solutions were compared at the final simulation time over the whole computational domain Ω using the discrete L^2 norm. Errors are reported only for the solid velocity component u_{s} in all cases.

The convergence rate is defined by

$$\text{rate} = \log\left(\frac{\|e^{\ell}\|_2}{\|e^{\ell-1}\|_2}\right) / \log\left(\frac{h^{\ell}_{\min}}{h^{\ell-1}_{\min}}\right) \tag{161}$$

where $\|e^{\ell}\|_2$ is the discrete L^2 norm of the error e^{ℓ} and $h^{\ell}_{\min}$ is the shortest distance between vertices at the ℓ'th refinement.

Table 3 shows the convergence rate for the inviscid, viscous (low-frequency), and viscous (high-frequency) cases. The results shows that method provides convergence rate of $N + 1$.

Table 3: The convergence rate as a function of the grid parameter $h_{\min}$ for three basis orders starting from order 3 (top), order 5 (middle), and ending with order 6 (bottom). Convergence rates together with the L^2-error values are reported for the inviscid (columns 2 and 3), viscous (low-frequency, columns 4 and 5), and viscous (high-frequency, columns 6 and 7) cases.

	inviscid		**low-frequency**		**high-frequency**	
$h_{\min}$ (m)	L^2-error	rate	L^2-error	rate	L^2-error	rate
0.32	5.02e-01	-	4.27e-01	-	5.00e-01	-
0.26	2.56e-01	3.93	2.09e-01	4.10	2.55e-01	3.93
0.21	1.46e-01	4.01	1.17e-01	4.13	1.46e-01	4.00
0.18	8.90e-02	4.16	7.38e-02	3.93	8.86e-02	4.16
0.32	5.08e-03	-	5.07e-03	-	5.07e-03	-
0.26	1.65e-03	5.90	1.66e-03	5.87	1.64e-03	5.90
0.21	6.59e-04	5.91	6.44e-04	6.07	6.58e-04	5.91
0.18	3.00e-04	6.01	2.94e-04	5.99	2.99e-04	6.01
0.32	4.04e-04	-	4.11e-04	-	4.04e-04	-
0.26	1.03e-04	6.97	1.06e-04	6.90	1.03e-04	6.97
0.21	3.29e-05	7.10	3.48e-05	6.98	3.29e-05	7.10
0.18	1.30e-05	6.91	1.36e-05	6.96	1.30e-05	6.90

6.1.1. The low frequency case: very small permeability

As noted above the accuracy of the low-storage Runge-Kutta (LSRK) scheme falls off as the permeability decreases to zero in the low frequency regime. In this section we give convergence results for an example in which the permeability is $k = 10^{-14}$ m^2, which may be regarded as a fairly extreme test of a time integration scheme, on both physical and numerical grounds. For comparison we give results for both LSRK and implicit-explicit Runge-Kutta (IMEX) time integration schemes in which the constant C in equation (160) is allowed to vary from 0.1 to 1.

In implicit-explicit Runge-Kutta schemes the idea is to solve the nonstiff terms using an explicit method while the stiff terms are solved using an implicit scheme. In practice, for the system considered in this paper, this means for solving the stiff source terms defined in (31) by using an implicit scheme. In this paper, we use the fourth-order additive Runge-Kutta scheme ARK4(3) developed in [48]. The scheme consists of two coupled Runge-Kutta schemes, namely the fourth-order explicit Runge-Kutta (ERK) and fourth-order explicit singly diagonally implicit Runge-Kutta (ESDIRK) scheme. The method has also been used in the context of DG schemes in [49, 50]. We note that IMEX schemes have been widely studied see, for example, [51, 52, 53].

In this second part of the convergence analysis, the computational domain Ω is set to $\Omega = [-1,\ 1]\times[-1,\ 1]$ metres. Here we set for the permeability $k = 10^{-14}$ m^2 while the other material parameters remained

unchanged. These parameter choices lead to wave speeds $c_p^{\mathrm{I}} = 2817$ m/s, $c_p^{\mathrm{II}} = 42$ m/s, and $c_s = 1534$ m/s with a Biot characteristic frequency $f_c = 4,420,970$ Hz.

Table 4 shows L^2-error values and corresponding convergence orders for the ARK4(3) time stepping scheme for three values of C in (160). Similarly in Table 5, corresponding results for the LSRK time stepping are shown. It is evident that the ARK4(3) scheme gives acceptable results in all cases, whereas it is necessary to make a substantial reduction in the time step for the LSRK scheme to work. We note that the convergence orders are suboptimal in that the orders are of order $N - 1$.

Table 4: The convergence rate as a function of the grid parameter $h_{\min}$ and constant C (see Eq. 160) for three basis orders starting from order 3 (top), order 5 (middle), and ending with order 6 (bottom) for the ARK4(3) time stepping scheme.

	$C = 0.1$		$C = 0.5$		$C = 1.0$	
$h_{\min}$ (cm)	L^2-error	rate	L^2-error	rate	L^2-error	rate
2.86	1.88e-02	-	1.88e-02	-	1.88e-02	-
2.67	1.80e-02	1.59	1.80e-02	1.59	1.80e-02	1.56
2.50	1.72e-02	1.75	1.72e-02	1.73	1.72e-02	1.73
2.35	1.63e-02	1.89	1.63e-02	1.90	1.63e-02	1.91
3.70	5.49e-03	-	5.50e-03	-	5.51e-03	-
3.39	4.35e-03	3.63	4.36e-03	3.63	4.37e-03	3.62
3.12	3.39e-03	4.08	3.39e-03	4.08	3.40e-03	4.07
2.90	2.60e-03	4.54	2.60e-03	4.54	2.61e-03	4.53
5.00	4.18e-03	-	4.19e-03	-	4.19e-03	-
4.44	2.91e-03	4.09	2.91e-03	4.10	2.91e-03	4.10
4.00	1.92e-03	4.93	1.92e-03	4.92	1.93e-03	4.89
3.64	1.20e-03	5.91	1.20e-03	5.92	1.21e-03	5.91

6.2. Heterogeneous models

In this section we show results for two heterogeneous cases. In Section 6.2.1 we consider two poroelastic subdomains while in Section 6.2.2 the model consists of one poroelastic and one elastic subdomain.

As a reference solution, we use the spectral element method code SPECFEM2D [54, 55, 11]. With this code we select the basis order equal to four for each quadrilateral element and the grid density is chosen to be seven elements per wavelength. As a time stepping scheme we use the Newmark time integration scheme. All material and geometrical definitions are the same as those used with the DG scheme.

Table 5: The convergence rate as a function of the grid parameter $h_{\min}$ and constant C (see Eq. 160) for three basis orders starting from order 3 (top), order 5 (middle), and ending with order 6 (bottom) for the LSRK time stepping scheme.

	$C = 0.1$		$C = 0.5$		$C = 1.0$	
$h_{\min}$ (cm)	L^2-error	rate	L^2-error	rate	L^2-error	rate
2.86	1.88e-02	-	fail	-	fail	-
2.67	1.80e-02	1.59	fail	-	fail	-
2.50	1.72e-02	1.75	fail	-	fail	-
2.35	1.63e-02	1.89	fail	-	fail	-
3.70	5.49e-03	-	fail	-	fail	-
3.39	4.35e-03	3.63	fail	-	fail	-
3.12	3.39e-03	4.08	fail	-	fail	-
2.90	2.60e-03	4.54	fail	-	fail	-
5.00	4.18e-03	-	fail	-	fail	-
4.44	2.91e-03	4.09	fail	-	fail	-
4.00	1.92e-03	4.93	fail	-	fail	-
3.64	1.20e-03	5.91	fail	-	fail	-

6.2.1. Poroelastic-poroelastic

In this first heterogeneous experiment, the computational domain is a rectangle $\Omega = [0,\ 4.8] \times [0,\ 4.8]$ km. Here the interface between subdomains is at $y = 2.4$ km. Material details for both subdomains are given in Table 6 while the derived wave speeds are given in Table 7. On the top surface, we use the free boundary condition (42) while other parts of the exterior boundary are modelled as outflow boundaries. In this experiment, the model setup is chosen so that we do not get any unwanted reflections from the outflow boundaries within the studied time window.

We note that the two subdomains have a jump in porosity. This presents a problem for the spectral element method as discussed in Section 13.3.3 [11] where the authors write that 'the SEM discretization naturally accounts for porosity gradients, but not for discontinuities in porosity', as shown in their Figure 12. To overcome this problem they implement a 'domain decomposition', although it would appear that this has not been implemented in version 7.0 (date: Wed Dec 10 02:43:39 2014) that we used in the following examples. In this example we set the viscosity equal to zero to permit comparison with the analytic solution in [56]. While the spectral element method can evidentally deal with this situation, one merit of the DG method is that it can resolve discontinuities on an element by element basis.

The seismic source is introduced using the seismic moment tensor M via

$$\mathbf{g}_s = (g_x, g_y)^{\mathsf{T}} = -M \cdot \nabla \delta(x_s, y_s) g(t) \tag{162}$$

where δ is the Dirac delta function and g is the time-dependent source function. The source is a Ricker wavelet with peak frequency $f_0 = 15$ Hz, time delay $t_0 = 1.2/f_0$, and location $(x_s,\ y_s) = (2.0,\ 2.8)$ km. In the simulation, we set the components $M_{xx} = M_{yy} = 1$, off-diagonal component $M_{xy} = 0$, and magnitude $M_0 = 10^{10}$ N·m. The volume source term $\mathbf{g}_V$ is then introduced in to model (27) by

$$\mathbf{g}_V = (0, 0, 0, 0, g_x, g_y, g_x, g_y)^{\mathsf{T}}. \tag{163}$$

Table 6: Material parameters used with the poroelastic-poroelastic case in Section 6.2.1.

variable name	**symbol**	**upper**	**lower**
solid density	ρ_{s} (kg/m^3)	2200	2700
fluid density	ρ_{f} (kg/m^3)	900	600
fluid bulk modulus	κ_{f} (GPa)	1.0	2.0
frame bulk modulus	κ_{fr} (GPa)	3.0	2.0
solid bulk modulus	κ_{s} (GPa)	5.0	40.0
frame shear modulus	μ_{fr} (GPa)	1.0	8.0
tortuosity	τ	2.0	2.5
porosity	ϕ	0.4	0.2
viscosity	η (Pa·s)	0	0

Table 7: Derived wave speeds for upper and lower subdomains for the poroelastic-poroelastic case in Section 6.2.1.

material	c_p^{I} (m/s)	c_p^{II} (m/s)	c_s (m/s)
upper	1724	735	816
lower	2990	844	1893

As noted above, non-uniform basis orders are used. The order N_ℓ of the basis function in element ℓ is defined by

$$N_\ell = \left\lceil \frac{2\pi a h^\ell_{\max}}{\lambda^w_\ell} + b \right\rceil \tag{164}$$

where $\lambda^w_\ell = c^\ell_{\min}/f$ is the wavelength, $c^\ell_{\min}$ is the minimum wave speed, and $\lceil\cdot\rceil$ is the ceiling function, see [26, 57, 58]. The parameters a and b control the local accuracy on each element. In the simulations we set $(a,\ b) = (1.2768,\ 1.4384)$ (this corresponds to 0.1% numerical accuracy), if the centre point (cp) of the ℓ'th triangle is in bounds $1.9 \le x^\ell_{\mathrm{cp}} \le 2.5$ km and $1.7 \le y^\ell_{\mathrm{cp}} \le 3.1$ km, otherwise $(a,\ b) = (0.7775,\ 0.2505)$ (this corresponds to 10% numerical accuracy). These parameter choices mean that we obtain a more accurate solution in a neighbourhood of the source and receivers. Values for parameters a and b are taken from [57].

The domain Ω is partitioned by an irregular triangular grid of 53,401 elements and 26,991 vertices ($h_{\min} = 19.6$ m and $h_{\max} = 81.0$ m) shown in Figure 3. In this experiment, the element size is chosen to be coarser in the lower subdomain which has one element per shortest wavelength while the upper domain has two elements per the shortest wavelength. The accuracy is then controlled using the basis order selection method described above.

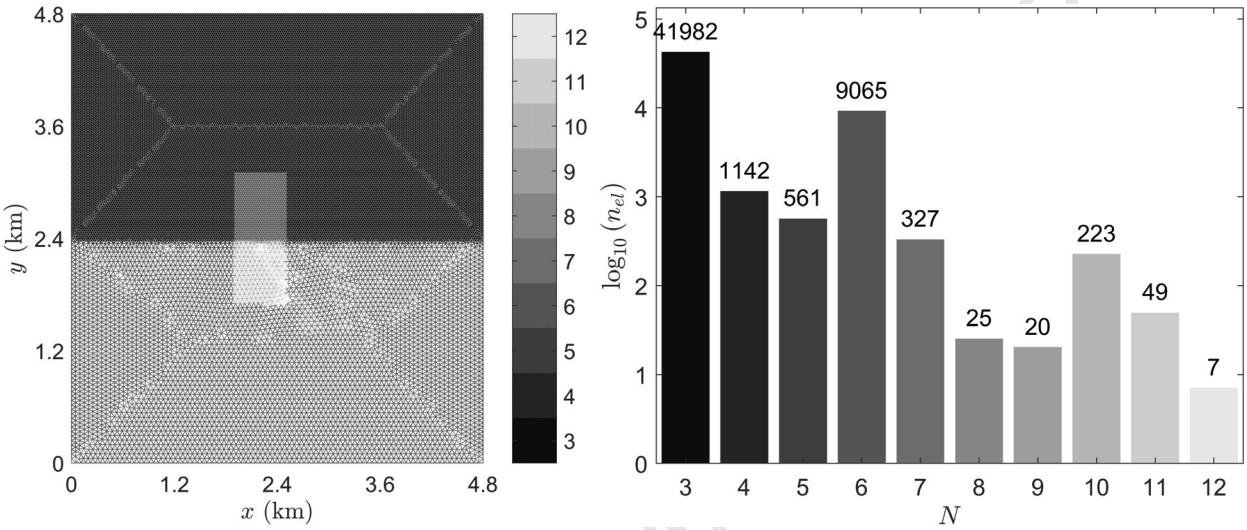

Figure 3: Discretisation of the computational domain Ω via irregularly refined triangular grid for the heterogeneous poroelastic-poroelastic case in Section 6.2.1. The colour bar shows the order of the basis functions for each element. Right: The number of elements as a function of basis order.

The use of non-uniform basis order can have a major effect on the degrees of freedom (DOF) and hence potentially speed-up the overall computation. The DOF (for each field component) can be computed as

$$\text{DOF} = \sum_{\ell=1}^{K} \frac{(N^\ell + 1)(N^\ell + 2)}{2}.$$

The basis order distribution given in Figure 3 gives a DOF = 735,725 while with the constant basis order (for example, $N = 6$) we get a DOF = 1,495,228 and hence the DOF reduction is evident.

The snapshot of the norm $\|\mathbf{v}_s\|$ of the solid velocity $\mathbf{v}_s$ in Figure 4 shows scattering at the material interface. The detail of the computational grid in the bottom graph shows the disparity in scales between the two poroelastic subdomains. This does not affect the accuracy of the solution as we now show.

Seismograms for the solid velocity are shown in Figure 5 at $(x,\ y) = (2.4,\ 3.0)$ km (top) and $(x, y) = (2.4,\ 1.8)$ km (bottom). The DG seismograms show good agreement with the analytic solution "Gar6more2D", [56] while the SPECFEM2D seismograms show some divergence. Furthermore, the seismograms show that the numerical accuracy is well-controlled using the non-uniform basis order selection described above. We note that we also carried out same experiment but constant porosity across the two subdomains and obtained very good agreement between SPECFEM2D, the analytic solution, and our code.

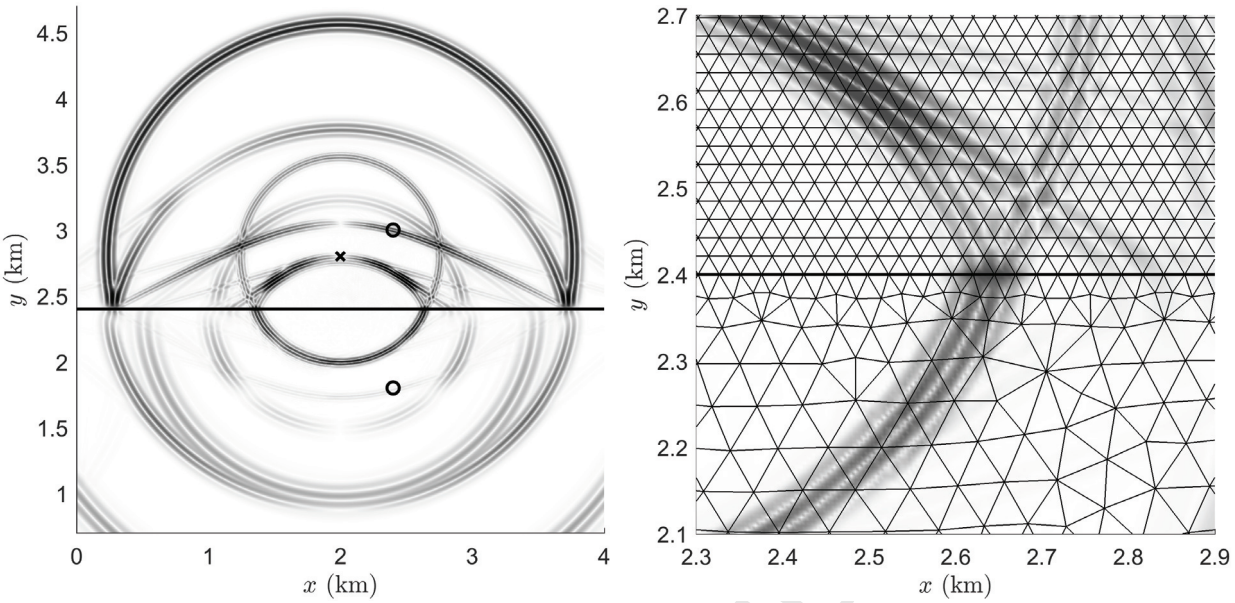

Figure 4: Snapshot of the solid velocity component $\|\mathbf{v}_s\|$ at time instant 1.11 s for the poroelastic-poroelastic simulation in Section 6.2.1. The figure on the left shows the full structure of the wave field while the figure on the right shows more detailed structure of the grid and one wave component at the material interface. The cross denotes the source location while circles are the receiver locations.

6.2.2. Poroelastic-elastic

In this second heterogeneous experiment, we consider a model consisting of one poroelastic and one elastic layer. The computational domain is a rectangle $\Omega = [0,\ 6] \times [0,\ 4.2]$ km, with the interface between the subdomains at $y = 3.2$ km. As in Section 6.2.1, we set the free boundary condition (42) on the top surface while the other boundaries are modelled using the outflow condition.

Detailed material description of the poroelastic material is given in Table 8 while in the elastic medium we set $\lambda_e = 63$ GPa, $\mu_e = 31.5$ GPa, and $\rho_e = 3500$ kg/m^3. Wave speeds for both domains are listed in Table 9.

The source is a Ricker wavelet with peak frequency $f_0 = 15$ Hz, time delay $t_0 = 1.2/f_0$, and location $(x_s,\ y_s) = (2.25,\ 3.70)$ km. The source is introduced using the point source defined in (162) with the same moment tensor values as used in Section 6.2.1. From Table 9 we see that we operate in Biot's low-frequency regime since $f < f_c$.

The computational domain Ω is partitioned by an irregular triangular grid of 60,117 elements and 30,402 vertices ($h_{\min} = 13.7$ m and $h_{\max} = 97.4$ m) as shown in Figure 6. As in the previous experiment, the element size is chosen to be coarser in the lower subdomain. The global numerical accuracy is then controlled using the basis order selection method explained above. It is evident from Figure 6 that the coarser grid in the lower subdomain forces the basis orders to be higher than in the more finely resolved upper subdomain. The

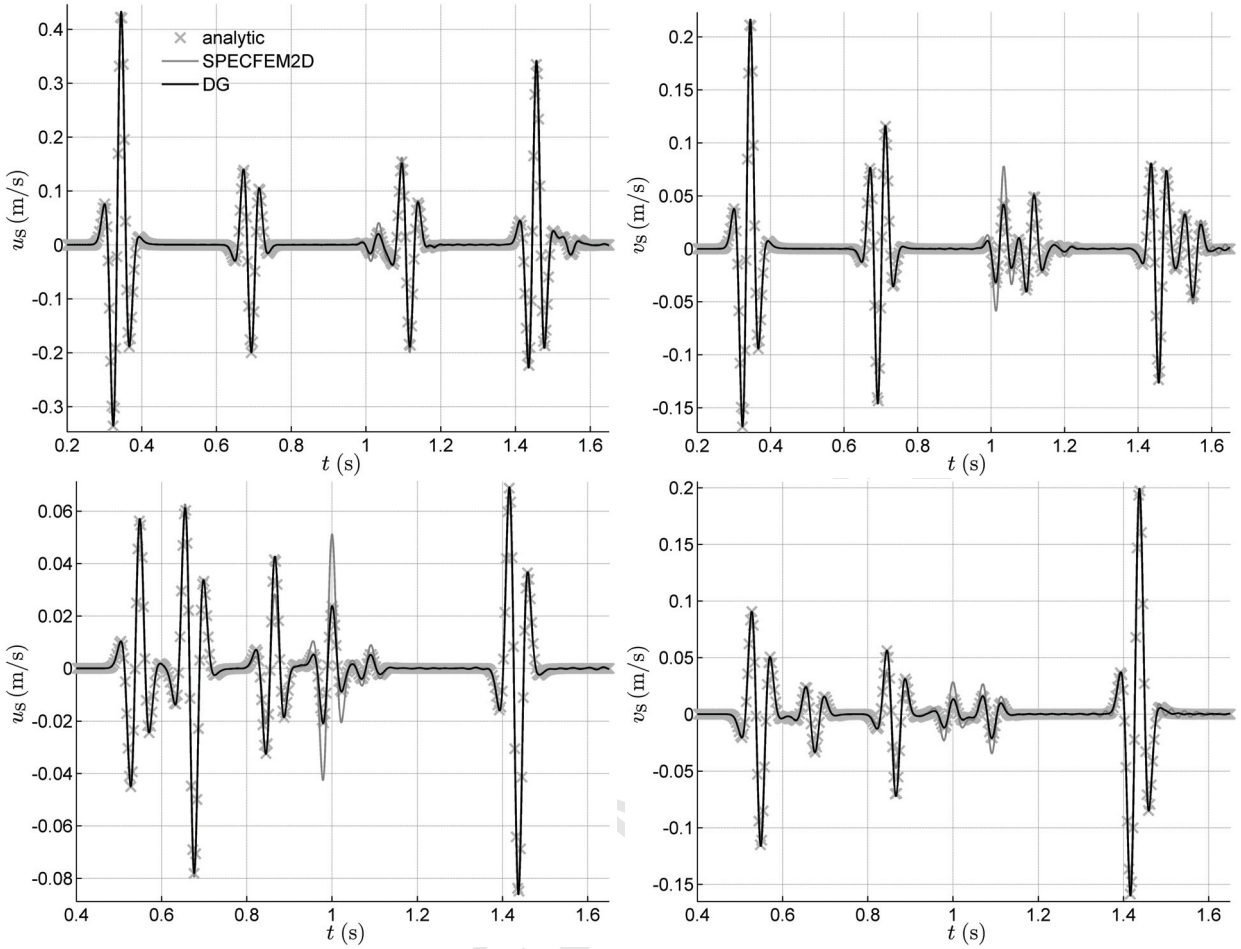

Figure 5: Poroelastic-poroelastic simulation of wave propagation in the two layered model of Section 6.2.1. Time history of velocity component u_s (Left) and v_s (Right) at two locations. In the top row receiver location is $(x,\ y) = (2.4,\ 3.0)$ km and in bottom row $(x,\ y) = (2.4,\ 1.8)$ km, respectively. Seismograms are visualised for two numerical solutions (DG and SPECFEM2D) and for analytic solution.

region of interest is defined by the rectangle with opposite corners $(x_1,\ y_1) = (2.15,\ 0)$ km and $(x_2,\ y_2) = (3.60,\ 2.65)$ km as shown in Figure 6.

The snapshot of the norm $\|\mathbf{v}_s\|$ of the solid velocity $\mathbf{v}_s$ in Figure 7 clearly shows reflections from the free surface and scattering at the material interface. The detail of the grid in the right plot shows the disparity in scales between the two subdomains.

Seismograms for the solid velocity $\mathbf{v}_s$ are shown in Figure 8 at $(x,\ y) = (3.5,\ 3.3)$ km (top) and $(x,\ y) = (3.5,\ 3.1)$ km (bottom). Results shows that we get very good agreement for both numerical solutions. Again we note that the numerical accuracy of the DG solution is well controlled by selecting the basis order individually for each element of the computational grid.

Table 8: Values of the physical parameters for the poroelastic subdomain in the coupled poroelastic-elastic case in Section 6.2.2.

variable name	**symbol**	**upper**
solid density	ρ_{s} (kg/m^3)	2200
fluid density	ρ_{f} (kg/m^3)	950
fluid bulk modulus	κ_{f} (GPa)	2.0
frame bulk modulus	κ_{fr} (GPa)	6.5
solid bulk modulus	κ_{s} (GPa)	7.0
frame shear modulus	μ_{fr} (GPa)	3.0
tortuosity	τ	2.0
porosity	ϕ	0.2
permeability	k (m^2)	10^{-10}
viscosity	η (Pa·s)	0.001

Table 9: Derived wave speeds for upper and lower subdomains for the coupled poroelastic-elastic case in Section 6.2.2.

material	f_c (Hz)	c_p^{I} (m/s)	c_p^{II} (m/s)	c_s (m/s)
upper	167.53	2328	458	1241
lower	-	6000	-	3000

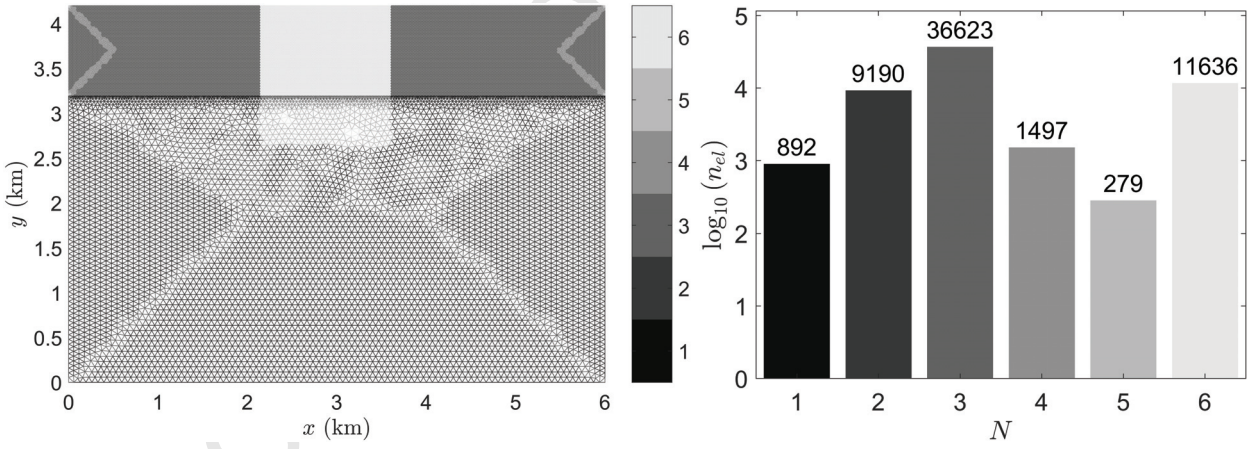

Figure 6: Discretisation of the computational domain Ω via irregularly refined triangular grid for the poroelastic-elastic case in Section 6.2.2. The colour bar shows the order of the basis functions chosen on each element. Right: The number of elements as a function of basis order.

6.3. Active seismic prospecting experiment

The following experiment is motivated by applications to groundwater tomography where the aim is to estimate aquifer features of interest (e.g. aquifer boundaries, porosity, and permeability). To do this in a

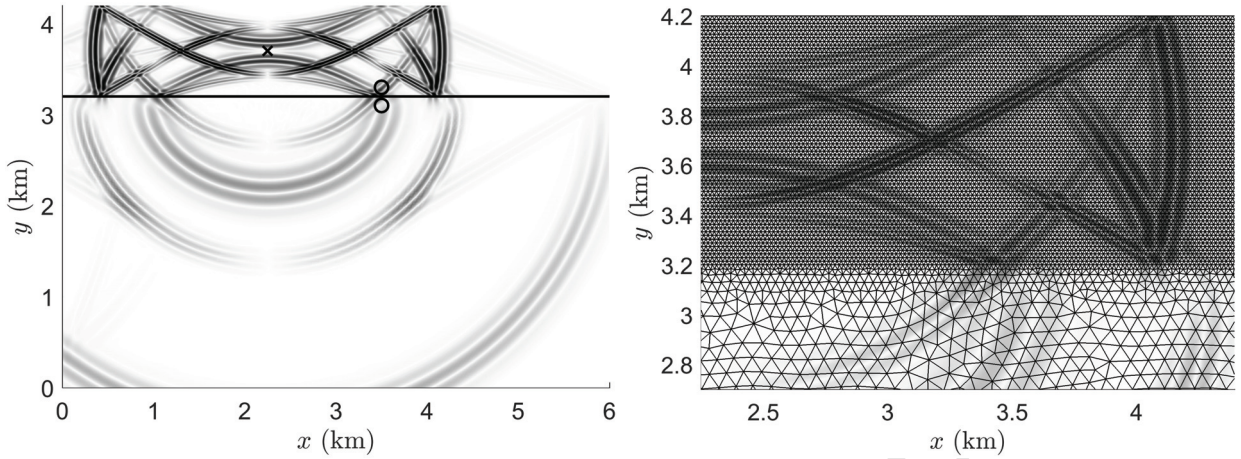

Figure 7: Snapshot of the solid velocity component $\|\mathbf{v}_s\|$ at time instant 0.897 s for the poroelastic-elastic simulation in Section 6.2.2. Figure on the left shows the full structure of the the wave field while the figure on right shows more detailed structure of the grid and one wave component on the material interface. The cross denotes the source location while circles are the receiver locations.

statistical (Bayesian) setting requires a framework for handling model and material uncertainty [9, 10]. One way to do this is to model the unknown parameters as realisations of Markov random fields (MRF).

We consider a case that consists of one elastic and two poroelastic subdomains. The upper poroelastic layer is air-saturated while the lower layer is water-saturated and so the interface corresponds to the water table. The computational domain is a rectangle $\Omega = [-0.4,\ 0.4] \times [-0.6,\ 0]$ km. The interface between the air- and water-saturated layers is at 10 metres while the interface between the aquifer and the rock basement is at 60 metres. Again, we set the free boundary condition (42) on the top surface while other boundaries are modelled as outflow boundaries.

The fluid parameters for the air-saturated part are given by: density $\rho_f = 1.2$ kg/m^3, fluid bulk modulus $\kappa_f = 1.4 \times 10^5$ Pa, and viscosity $\eta = 10^{-4}$ Pa·s. For the water-saturated part we set $\rho_f = 1040$ kg/m^3, $\kappa_f = 2.5$ GPa, and $\eta = 10^{-3}$ Pa·s.

The remaining material parameters are realisations of Gaussian MRF. The MRF's are generated using an anisotropic smoothness prior [59, 60]. For the rock medium we took correlation lengths of 300 m and 30 m in the horizontal and vertical directions while in the aquifer we chose 50 m and 5 m in the horizontal and vertical directions, respectively. These choices correspond to a stratification with a higher spatial smoothness in the x direction (horizontal) and a lower degree of smoothness in the y direction. The standard deviation was taken to be 15% from the mean value for solid material components which are shown in Table 10 (the fluid density ρ_f, fluid bulk modulus κ_f, and viscosity η are assumed to be constant). In the rock layer below the aquifer we assume very low porosity and hence the model is considered to be purely elastic with parameters $\lambda_e = 63$ GPa, $\mu_e = 31.5$ GPa, and $\rho_e = 3500$ kg/m^3. Figure 9 shows the distribution of the slow

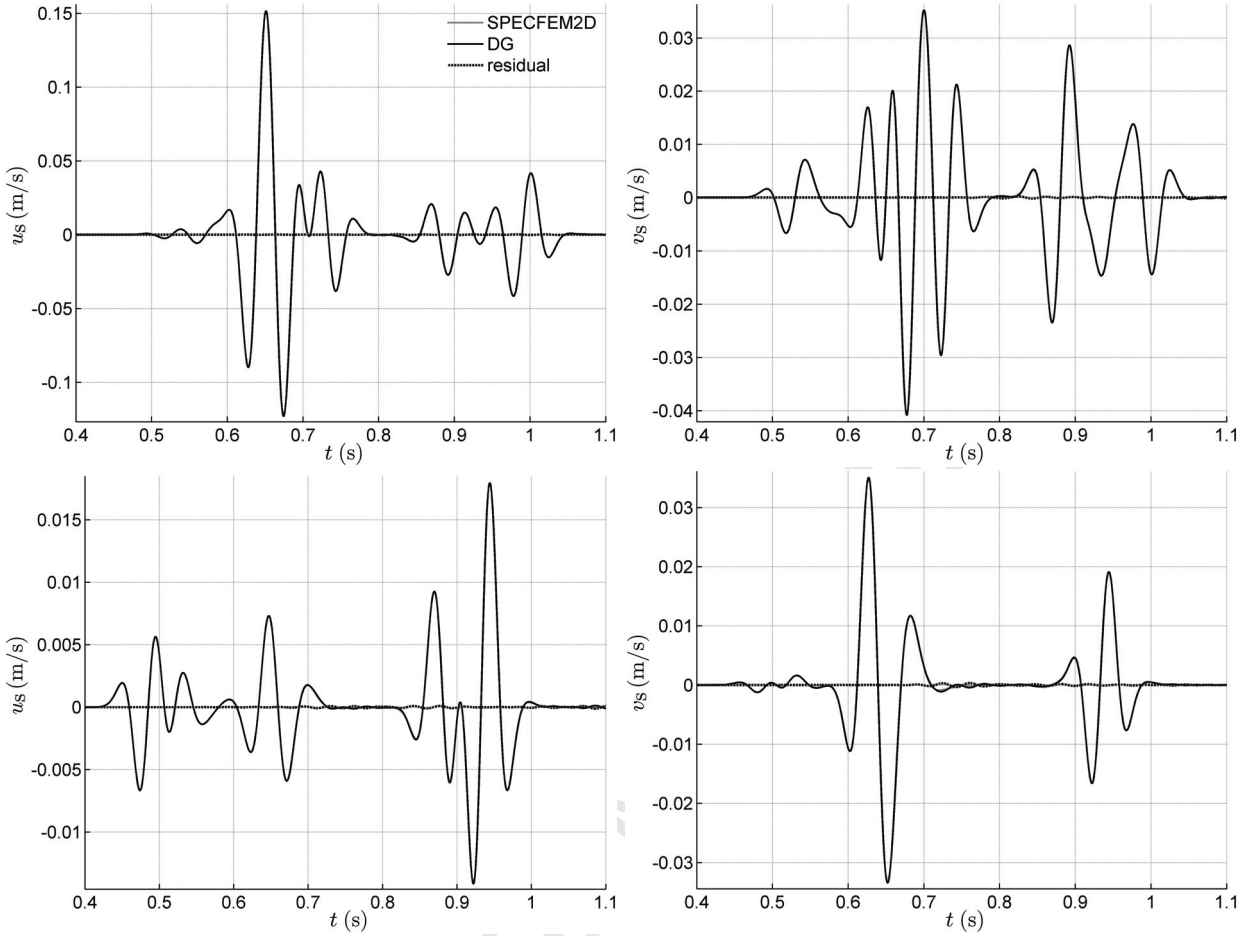

Figure 8: Coupled poroelastic-elastic simulation of wave propagation in the two layered model of Section 6.2.2. Figure shows time history of velocity component u_s (Left) and v_s (Right) at two locations. In the top row receiver location is $(x,\ y) = (3.5,\ 3.3)$ km and in bottom row $(x,\ y) = (3.5,\ 3.1)$ km, respectively. Seismograms are visualised for numerical solutions (DG and SPECFEM2D) and the residual between them.

pressure wave speeds c_p^{II} for the air- and water-saturated zones (left) while the shear speeds c_s are shown for the elastic rock layer (right).

The seismic source is a Ricker wavelet with peak frequency $f_0 = 40$ Hz, time delay $t_0 = 1.2/f_0$, and location $(x_s,\ y_s) = (0,\ -0.5)$ m. The source is introduced using the point source defined in (162) with the moment tensor values: $M_{xx} = M_{yy} = 1,\ M_{xy} = 0$.

In this example, we operate in Biot's high-frequency regime in the water-saturated subdomain (due to the relatively high aquifer permeability), while in the air-saturated subdomain we operate in the low-frequency regime (see Tables 10 and 11). In the high-frequency subdomain the quality factor Q_0 is set to 30.

The computational grid shown in Figure 10 consists of 43,962 triangular elements and 22,449 vertices ($h_{\min} = 0.9$ m and $h_{\max} = 21.2$ m). In this example, for the grid density we choose three elements per shortest

Table 10: Mean values of the physical parameters for the aquifer in the active prospecting experiment in Section 6.3.

variable name	**symbol**	**aquifer**
solid density	$\rho_{\rm s}$ (kg/m^3)	2650
frame bulk modulus	$\kappa_{\rm fr}$ (GPa)	0.3
solid bulk modulus	$\kappa_{\rm s}$ (GPa)	3.0
frame shear modulus	$\mu_{\rm fr}$ (GPa)	0.15
tortuosity	τ	2.0
porosity	ϕ	0.25
permeability	k (m^2)	8×10^{-9}

Table 11: Computed mean speeds in different subdomains for the active prospecting experiment in Section 6.3.

Subdomain	f_c (Hz)	$c_p^{\rm I}$ (m/s)	$c_p^{\rm II}$ (m/s)	c_s (m/s)
air-saturated	221.79	550	134	307
water-saturated	2.89	1242	259	282
rock	-	6014	-	3065

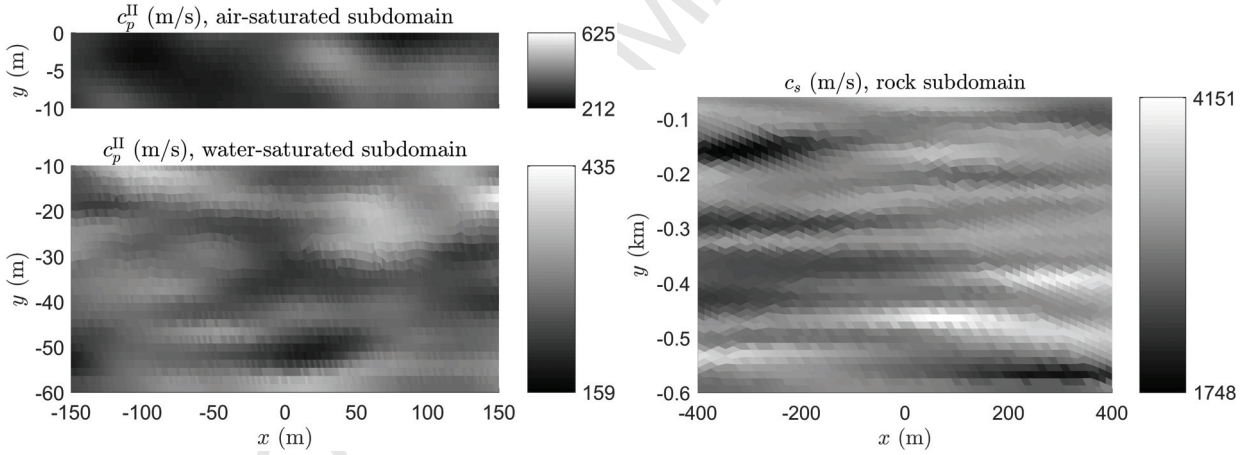

Figure 9: Slow pressure wave speed (left) and shear wave speed (right) in the active prospecting experiment in Section 6.3.

wavelength in the aquifer and four elements per wavelength in the rock subdomain, which is visually sufficient to capture the heterogeneous material structure shown in Figure 9. The region of interest is defined by the rectangle with opposite corners $(x_1,\ y_1) = (-250,\ 0)$ m and $(x_2,\ y_2) = (250,\ -120)$ m.

The snapshots of the norms $\|\mathbf{v}_{\rm f}\|$ and $\|\mathbf{v}_{\rm s}\|$ of the fluid and solid velocities in Figure 11 show more scattered wave fields than the previous examples due to the underlying heterogeneity of the material (see Figure 9). This is reflected in the seismograms in Figures 12 and 13 whose complexity makes them appear superficially

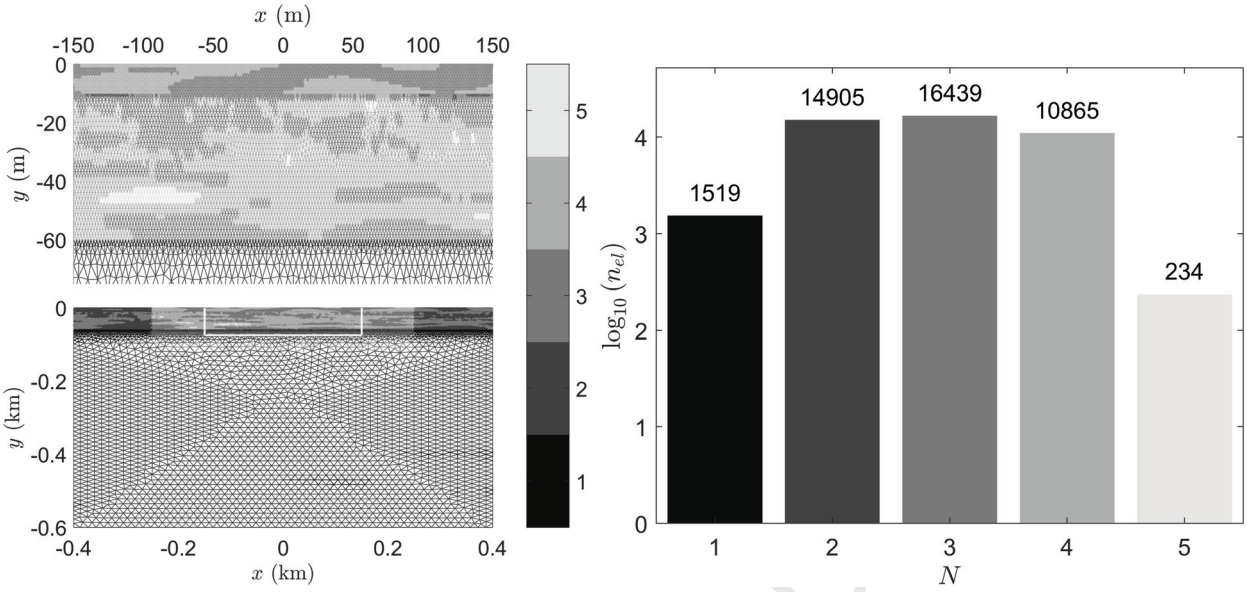

Figure 10: Discretisation of the computational domain Ω via irregularly refined triangular grid for the active prospecting example in Section 6.3. On the left we show a closeup that is highlighted by the white line in the middle picture. The colour bar shows the order of the basis functions chosen on each element. Right: The number of elements as a function of basis order.

more 'realistic'. It is evident that the amplitudes of velocity for the fluid components are somewhat smaller that the solid velocity components, as expected. The seismograms for the surface receivers shown in the upper plots in Figures 12 and 13 have the greatest amplitudes due to surface wave effects.

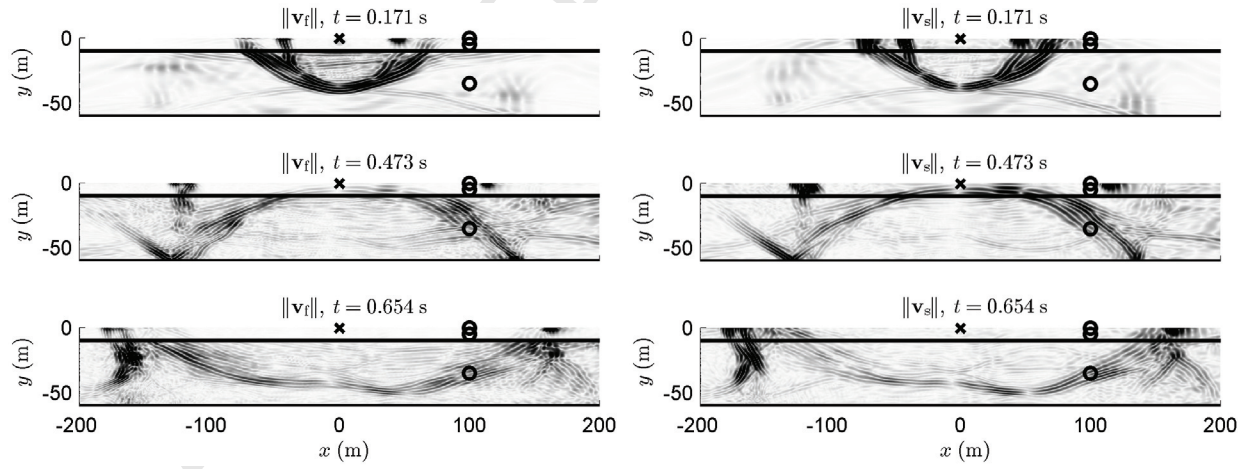

Figure 11: Snapshots of the fluid velocity component $\|\mathbf{v}_\mathrm{f}\|$ (Left) and solid velocity component $\|\mathbf{v}_\mathrm{s}\|$ (Right) at three time instants for the active prospecting example in Section 6.3. The cross denotes the source location while circles are the receiver locations.

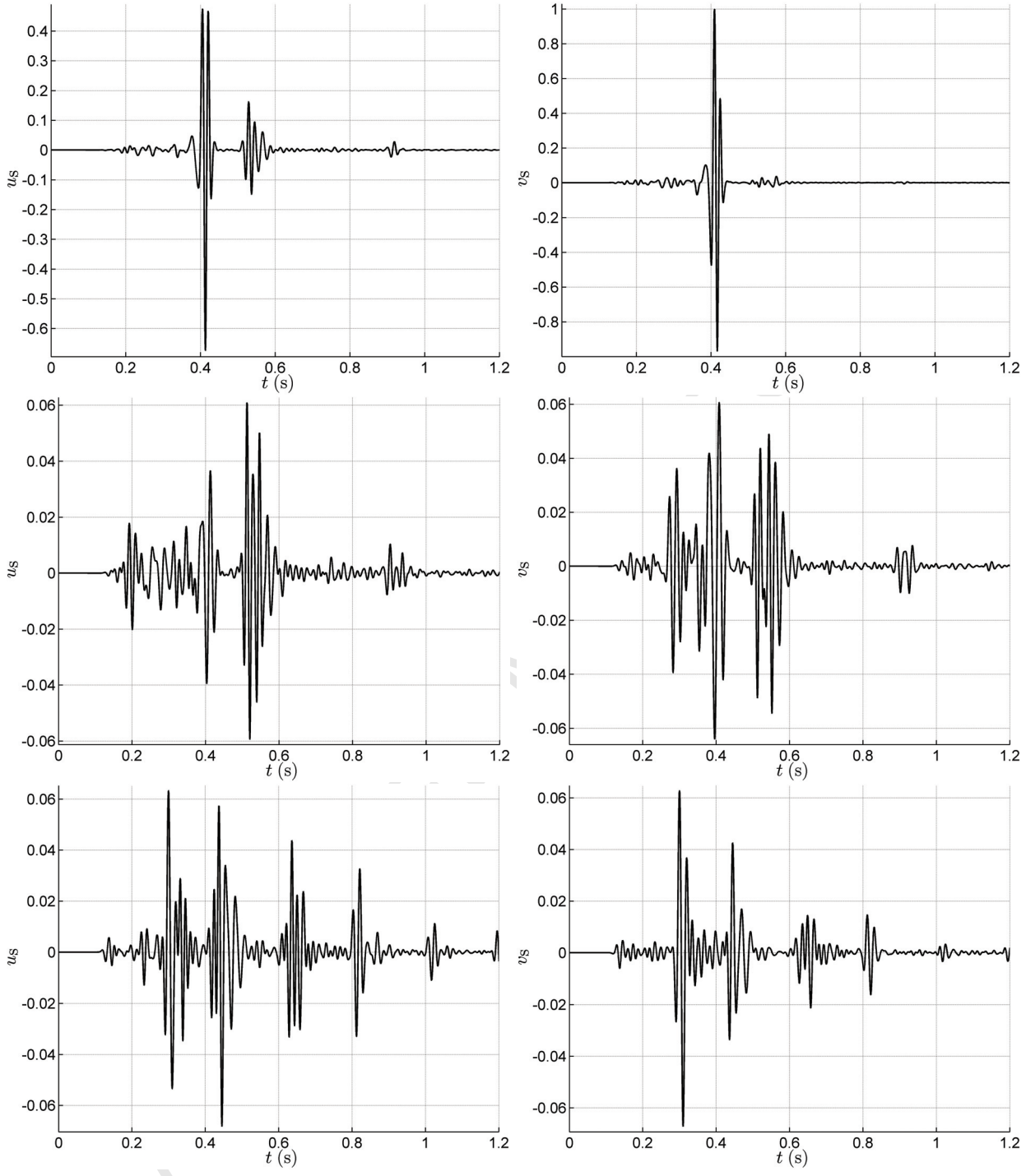

Figure 12: Time history of normalised velocity components u_s (Left) and v_s (Right) at two locations for the active prospecting example in Section 6.3, where the normalisation is taken with respect to the top right-hand plot. In the top row receiver location is $(x,\ z) = (100,\ 0)$ m, in the middle row $(x,\ z) = (100,\ -5)$ m, and the in bottom row $(x,\ y) = (100,\ -35)$ m, respectively.

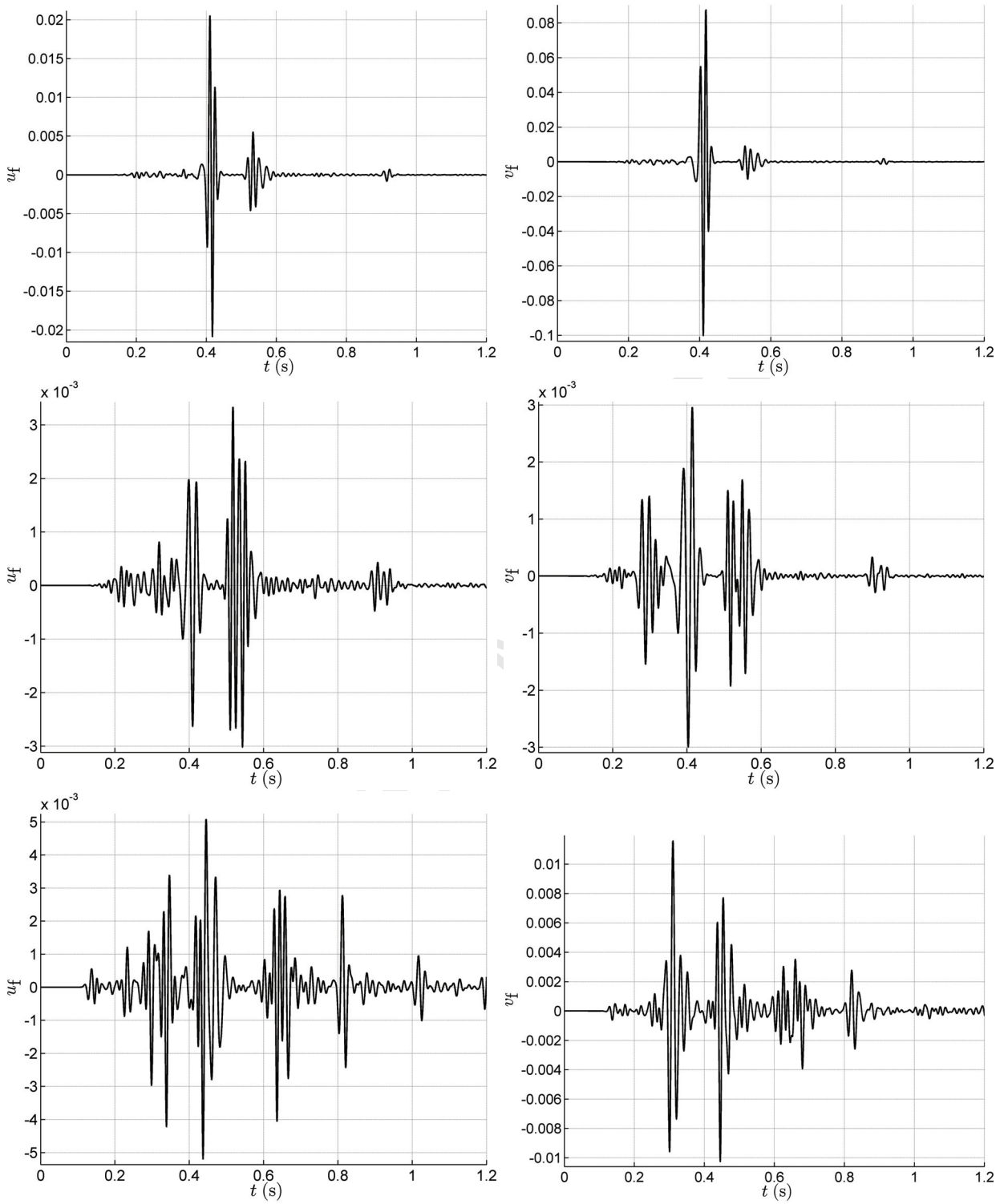

Figure 13: Time history of normalised velocity components u_{f} (Left) and v_{f} (Right) at two locations for the active prospecting example in Section 6.3. In the top row receiver location is $(x,\ z) = (100,\ 0)$ m, in the middle row $(x,\ z) = (100,\ -5)$ m, and in the bottom row $(x,\ y) = (100,\ -35)$ m, respectively.

7. Discussion

Our main motivation in this paper was to develop an accurate solver for poroelastic wave propagation in two dimensions in Biot's low and high-frequency regimes, coupled with elastic wave propagation for groundwater tomographic applications. (For application examples see [61, 62].) In applications to groundwater tomography where aquifer permeabilities can be quite large (up to $k \sim 10^{-7}$ m^2, [63]), one is forced to operate in the high- and low-frequency regimes for the water-saturated and air-saturated subdomains respectively (since the density of air forces that part of the domain to fall within Biot's low-frequency domain).

One of the requirements of our solver is that it can resolve material discontinuities. As we stated earlier and have shown in the numerical experiments, the discontinuous Galerkin method coupled with a full solution to the Riemann problem handles this naturally. The convergence test results indicate that the solver satisfies the theoretical convergence properties (convergence rate = polynomial order + 1) for typical parameter ranges one is likely to encounter in groundwater tomography. However, we note that when the wave is highly dissipative and slow in Biot's low-frequency regime (corresponding to very low permeabilities), it will be necessary to implement an operator splitting technique or IMEX scheme to deal with the diffusive part, which in certain circumstances can be quasi-static [43, 47, 13]. In any event, the slow P-wave can impose a significant restraint on the grid resolution or basis order, and hence the time step, in the poroelastic part. Usually this makes it impracticable to use a finely-resolved poroelastic model to invert data, even in a synthetic setting [9, 10], necessitating viscoelastic approximations [64].

To illustrate the use of non-uniform basis functions, we considered examples with two subdomains in which one subdomain's grid was chosen to be somewhat coarser than the other's. A stipulated level of accuracy was maintained by compensating the more coarsely resolved part of the grid by higher-order basis functions. While this has a degree of artificiality we remark that, particularly for more complex geometries, there is no a priori guarantee that the grid quality is uniformly good. The use of non-uniform basis functions is an effective way to deal with this. Moreover, another merit of taking a relatively coarse computational grid is that it is usually computationally cheaper to use higher-order basis functions than to resolve and use lower-order basis functions, [34]. There can also be a storage handling consideration to discourage very dense grids required for large-scale models when low-order bases are used (e.g. domain size is 'many' wavelengths) which require significant accuracy (e.g. ten elements per wavelength).

We remark that the importance of the slow P-wave is not entirely evident to us. In our previous studies [9, 10], we have have shown in the content of full wave inversion that one cannot ignore the slow P-wave without introducing unacceptable error in the prediction (albeit for synthetic data), although its existence in real situations is debated, [43]. One of the problems is that with scattering in heterogeneous media, it is very difficult to isolate the slow P-wave.

Regarding poroelastic inverse problems, our experience is that a deterministic approach to parameter

estimation will be particularly problematic given both the complex coupling between the solid and fluid parameters and the model uncertainties without significant prior information (e.g. from well logs or 'known' material properties, which allows one to reduce the problem to estimating essential parameters of interest). It is common statistical understanding that even small model error can result in large predictive error [65]. In our view the only feasible approach is to work in a statistical (Bayesian) framework in which the uncertainties are explicitly modelled as probability distributions, [9, 10], although this adds another layer to the overall computational burden. For this reason we need a solver that can resolve material heterogeneities modelled as random fields as in the active prospecting experiment. This is the topic of future studies.

We note that the outflow boundaries implemented here are only exact in the one-dimensional case and permit boundary artefacts in the two-dimensional situation considered in this paper. In applications to poroelastic inverse problems we think that this is not very important, and speculate that with realistic levels of noise encountered in practice that it probably does not significantly affect the inversion. We further remark that implementation of perfectly matched layers or high-order absorbing boundary conditions for a coupled elastic/poroelastic in all frequency regimes with comprehensive viscoelastic and poroelastic modelling is likely to be extremely challenging.

The formulation considered here for isotropic media can be extended with some loss of elegance to non-isotropic media, e.g. orthotropic media as in [13], since the eigenstructure now needs to be dealt with numerically.

8. Conclusions

In this paper we developed a DG solver for a coupled two-dimensional poroelastic/elastic isotropic model incorporating Biot's low- and high-frequency regimes in Hesthaven and Warburton's framework [34]. This formulation allows us to use different basis functions in different elements, so that numerical accuracy is controlled by both the grid resolution and the local basis order. Time integration was carried out using both an explicit low-storage Runge-Kutta scheme as well an implicit-explicit scheme for a stiff example. We considered free surface and absorbing boundary conditions, where the latter were modelled as outflows. Numerical experiments showed that the solver satisfied theoretical convergence rates for LSRK time integration, while the IMEX time integration gave suboptimal but consistent convergence rates, and that choosing higher-order basis functions on poorly resolved parts of the grid maintained accuracy. Furthermore, the exact Riemann-problem-based numerical flux implementation resolves naturally all material discontinuities. While two-dimensional poroelastic wave solvers are useful for theoretical studies, particularly inverse problems, genuine applications require three-dimensional solvers. This is the topic of a forthcoming paper.

Acknowledgements

This work has been supported by the Academy of Finland (projects 250215 and 257372), by the strategic funding of the University of Eastern Finland, and by the Väisälä-foundation.

In conclusion we express our thanks to Professor J.M. Carcione for some essential clarification on the modelling the the Biot high-frequency regime and to our colleagues Professors Roger Nokes and Gabriele Chiaro for some very helpful discussions.

Appendix

Appendix A. Derivation of the eigenstructure

Appendix A.1. 2×2 *scalar matrices*

All the eigenvalue calculations below ultimately decouple into 2×2 matrices, whose eigenvalues and eigenvectors can be found explicitly. For later use, we record the results of this simple calculation. Suppose we have a 2×2 matrix $M = (m_{jk})_{j,k=1}^{2}$. It turns out to be convenient to consider the characteristic polynomial of M, multiplied by some factor Z_1. Let a_2, a_1, a_0 be the coefficients of this polynomial, so $a_2 = Z_1$, $a_1 = -Z_1 \operatorname{trace}(M)$ and $a_0 = Z_1 \det(M)$. Now let $Z_2 = -a_1$ and $Z_3 = a_1^2 - 4a_0a_2$. In terms of these abbreviations, the quadratic formula gives us the eigenvalues:

$$\frac{Z_2 \pm \sqrt{Z_3}}{2Z_1}.$$

It is now a straightforward calculation to see that the eigenvectors are

$$(Z_5, Z_4 \pm \sqrt{Z_3})^{\mathsf{T}}$$

where

$$Z_4 = Z_2 - 2Z_1 m_{11}; \qquad Z_5 = 2Z_1 m_{12}.$$

Here, we have arbitrarily chosen to represent the eigenvectors in terms of the eigenvalues and the first row of the matrix; we could equally have used the second row.

Appendix A.2. 2×2 *block matrices*

In order to decouple our eigenproblems, we repeatedly find and exploit 2×2 block matrix structure. We record here some general results about 2×2 block matrices, all of which are easily verified. We consider 2×2 block matrices of the form

$$M = \left(\begin{array}{c|c} M_{\mathrm{UL}} & M_{\mathrm{UR}} \\ \hline M_{\mathrm{LL}} & M_{\mathrm{LR}} \end{array}\right)$$

where M_{UL} and M_{LR} are $m \times m$ and $n \times n$ matrices, which we refer to as an $m + n$ block decomposition of M. Suppose x and y are respectively m- and n-dimensional (column) vectors. Denote by

$$(x; y) = \left(\frac{x}{y}\right)$$

the $(m + n)$-dimensional column vector formed by stacking x on top of y. The matrix M acts on $(x; y)$ by

$$\left(\begin{array}{c|c} M_{\mathrm{UL}} & M_{\mathrm{UR}} \\ \hline M_{\mathrm{LL}} & M_{\mathrm{LR}} \end{array}\right) \left(\frac{x}{y}\right) = \left(\frac{M_{\mathrm{UL}}x + M_{\mathrm{UR}}y}{M_{\mathrm{LL}}x + M_{\mathrm{LR}}y}\right).$$

Appendix A.3. 2×2 *block triangular matrices*

If M has either of the block triangular forms

$$M = \left(\begin{array}{c|c} M_{\mathrm{UL}} & 0 \\ \hline M_{\mathrm{LL}} & M_{\mathrm{LR}} \end{array}\right); \qquad M = \left(\begin{array}{c|c} M_{\mathrm{UL}} & M_{\mathrm{UR}} \\ \hline 0 & M_{\mathrm{LR}} \end{array}\right)$$

then c is an eigenvalue of M if and only if c is an eigenvalue of either diagonal block, M_{UL} or M_{LR} (this can most easily be seen by putting the two blocks into triangular form using e.g. the Schur triangularisation theorem). These block forms include several useful special cases, notably the block diagonal case in which M_{LR} and M_{UL} are both zero and the cases in which both blocks in the same row or column are zero.

It is not difficult to describe the eigenvectors of M in terms of those of the diagonal blocks, although some care needs to be taken if the two blocks have a common eigenvalue. Here we note only that, in the special case of a block diagonal matrix, an eigenvector x of M_{UL} corresponds to an eigenvector $(x; 0)$ of M and an eigenvector y of M_{LR} corresponds to an eigenvector $(0; y)$ of M.

Appendix A.4. 2×2 *block antidiagonal matrices*

Here we consider the case

$$M = \left(\begin{array}{c|c} 0 & M_{\mathrm{UR}} \\ \hline M_{\mathrm{LL}} & 0 \end{array}\right).$$

Notice that M^2 is a block diagonal matrix, with diagonal blocks $M_{\mathrm{UR}}M_{\mathrm{LL}}$ and $M_{\mathrm{LL}}M_{\mathrm{UR}}$, which have the same non-zero eigenvalues. The non-zero eigenvalues of M are the square roots (both branches) of these. We can construct the associated eigenvectors of M from those of $M_{\mathrm{UR}}M_{\mathrm{LL}}$ and $M_{\mathrm{LL}}M_{\mathrm{UR}}$: if $M_{\mathrm{UR}}M_{\mathrm{LL}}x = c^2x$ then $(\pm cx; M_{\mathrm{LL}}x)$ are eigenvectors of M with eigenvalues $\pm c$ and if $M_{\mathrm{LL}}M_{\mathrm{UR}}y = c^2y$ then $(M_{\mathrm{UR}}y; \pm cy)$ are eigenvectors of M with eigenvalues $\pm c$.

The zero eigenvalue needs to be handled separately: its eigenspace, the nullspace of M, is spanned by vectors of the form $(x; 0)$ and $(0; y)$ where $M_{\mathrm{LL}}x = 0$ and $M_{\mathrm{UR}}y = 0$.

Appendix B. Wave speed and eigenvector computations

Appendix B.1. The inviscid case

Starting with the non-dissipative case, we have

$$Q = \left(\begin{array}{cccc|cccc} 1 & 0 & 0 & 0 & 0 & 0 & 0 & 0 \\ 0 & 1 & 0 & 0 & 0 & 0 & 0 & 0 \\ 0 & 0 & 1 & 0 & 0 & 0 & 0 & 0 \\ 0 & 0 & 0 & 1 & 0 & 0 & 0 & 0 \\ \hline 0 & 0 & 0 & 0 & \rho_{\mathrm{a}} & 0 & \rho_{\mathrm{f}} & 0 \\ 0 & 0 & 0 & 0 & 0 & \rho_{\mathrm{a}} & 0 & \rho_{\mathrm{f}} \\ 0 & 0 & 0 & 0 & \rho_{\mathrm{f}} & 0 & m & 0 \\ 0 & 0 & 0 & 0 & 0 & \rho_{\mathrm{f}} & 0 & m \end{array}\right)$$

and

$$A = \left(\begin{array}{cccc|cccc} 0 & 0 & 0 & 0 & -1 & 0 & 0 & 0 \\ 0 & 0 & 0 & 0 & 0 & 0 & 0 & 0 \\ 0 & 0 & 0 & 0 & 0 & -\frac{1}{2} & 0 & 0 \\ 0 & 0 & 0 & 0 & 0 & 0 & 1 & 0 \\ \hline -\lambda - 2\mu_{\mathrm{fr}} & -\lambda & 0 & M\alpha & 0 & 0 & 0 & 0 \\ 0 & 0 & -2\mu_{\mathrm{fr}} & 0 & 0 & 0 & 0 & 0 \\ -M\alpha & -M\alpha & 0 & M & 0 & 0 & 0 & 0 \\ 0 & 0 & 0 & 0 & 0 & 0 & 0 & 0 \end{array}\right).$$

We can see that Q and A are both 2×2 block matrices, with 4×4 blocks, and are respectively block diagonal and block antidiagonal. However, this is not the "best" block decomposition we can find. If we exchange rows 6 and 7 and columns 6 and 7 in both matrices, we obtain

$$Q' = \left(\begin{array}{cccc|cccc} 1 & 0 & 0 & 0 & 0 & 0 & 0 & 0 \\ 0 & 1 & 0 & 0 & 0 & 0 & 0 & 0 \\ 0 & 0 & 1 & 0 & 0 & 0 & 0 & 0 \\ 0 & 0 & 0 & 1 & 0 & 0 & 0 & 0 \\ \hline 0 & 0 & 0 & 0 & \rho_{\mathrm{a}} & \rho_{\mathrm{f}} & 0 & 0 \\ 0 & 0 & 0 & 0 & \rho_{\mathrm{f}} & m & 0 & 0 \\ 0 & 0 & 0 & 0 & 0 & 0 & \rho_{\mathrm{a}} & \rho_{\mathrm{f}} \\ 0 & 0 & 0 & 0 & 0 & 0 & \rho_{\mathrm{f}} & m \end{array}\right)$$

and

$$A' = \left(\begin{array}{cccc|cccc} 0 & 0 & 0 & 0 & -1 & 0 & 0 & 0 \\ 0 & 0 & 0 & 0 & 0 & 0 & 0 & 0 \\ 0 & 0 & 0 & 0 & 0 & 0 & -\frac{1}{2} & 0 \\ 0 & 0 & 0 & 0 & 0 & 1 & 0 & 0 \\ \hline -\lambda - 2\mu_{\mathrm{fr}} & -\lambda & 0 & M\alpha & 0 & 0 & 0 & 0 \\ -M\alpha & -M\alpha & 0 & M & 0 & 0 & 0 & 0 \\ 0 & 0 & -2\mu_{\mathrm{fr}} & 0 & 0 & 0 & 0 & 0 \\ 0 & 0 & 0 & 0 & 0 & 0 & 0 & 0 \end{array}\right).$$

Physically, this represents reordering the terms in the vector, grouping by dimension (x then y) instead of by medium (solid then fluid). In this form, the original zero blocks have been retained and the non-zero blocks have acquired their 2×2 structure: Q'_{LR} and A'_{LL} are respectively block diagonal and block triangular, both with 2×2 blocks. The blocks in Q'_{LR} are equal to each other so we can now find $Q'^{-1}A'$ by multiplying the inverse of this 2×2 block against the top and bottom halves of A'_{LL}.

$$Q'^{-1}A' = \left(\begin{array}{cccc|cccc} 0 & 0 & 0 & 0 & -1 & 0 & 0 & 0 \\ 0 & 0 & 0 & 0 & 0 & 0 & 0 & 0 \\ 0 & 0 & 0 & 0 & 0 & 0 & -\frac{1}{2} & 0 \\ 0 & 0 & 0 & 0 & 0 & 1 & 0 & 0 \\ \hline \star & \star & 0 & \star & 0 & 0 & 0 & 0 \\ \star & \star & 0 & \star & 0 & 0 & 0 & 0 \\ 0 & 0 & \star & 0 & 0 & 0 & 0 & 0 \\ 0 & 0 & \star & 0 & 0 & 0 & 0 & 0 \end{array}\right)$$

where the stars represent the block

$$(Q'^{-1}A')_{\mathrm{LL}} = \frac{1}{m\rho_{\mathrm{a}} - \rho_{\mathrm{f}}^2} \begin{pmatrix} M\alpha\rho_{\mathrm{f}} - m\left(\lambda + 2\mu_{\mathrm{fr}}\right) & M\alpha\rho_{\mathrm{f}} - \lambda m & 0 & M\left(\alpha m - \rho_{\mathrm{f}}\right) \\ -M\alpha\rho_{\mathrm{a}} + \rho_{\mathrm{f}}\left(\lambda + 2\mu_{\mathrm{fr}}\right) & -M\alpha\rho_{\mathrm{a}} + \lambda\rho_{\mathrm{f}} & 0 & M\left(-\alpha\rho_{\mathrm{f}} + \rho_{\mathrm{a}}\right) \\ 0 & 0 & -2m\mu_{\mathrm{fr}} & 0 \\ 0 & 0 & 2\mu_{\mathrm{fr}}\rho_{\mathrm{f}} & 0 \end{pmatrix}.$$

Because $(Q'^{-1}A')$ is block anti-diagonal, its eigenvalues are (Section Appendix A.4) the squares of those of $(Q'^{-1}A')_{\mathrm{LL}}(Q'^{-1}A)_{\mathrm{UR}}$: explicitly,

$$\frac{1}{m\rho_{\mathrm{a}} - \rho_{\mathrm{f}}^2} \left(\begin{array}{cc|cc} -M\alpha\rho_{\mathrm{f}} + m\left(\lambda + 2\mu_{\mathrm{fr}}\right) & M\left(\alpha m - \rho_{\mathrm{f}}\right) & 0 & 0 \\ M\alpha\rho_{\mathrm{a}} - \rho_{\mathrm{f}}\left(\lambda + 2\mu_{\mathrm{fr}}\right) & M\left(-\alpha\rho_{\mathrm{f}} + \rho_{\mathrm{a}}\right) & 0 & 0 \\ \hline 0 & 0 & m\mu_{\mathrm{fr}} & 0 \\ 0 & 0 & -\mu_{\mathrm{fr}}\rho_{\mathrm{f}} & 0 \end{array}\right).$$

In fact, we could have found this matrix without explicitly computing $Q'^{-1}A'$: because of the block nature of the matrices, we have

$$(Q'^{-1}A')_{\mathrm{LL}}(Q'^{-1}A)_{\mathrm{UR}} = (Q'_{\mathrm{LR}})^{-1}A'_{\mathrm{LL}}A'_{\mathrm{UR}}.$$

This is a block diagonal matrix so (Section Appendix A.3) its eigenvalues are the union of those of its two diagonal blocks.

The lower right block is easy: its eigenvalues are 0, with eigenvector $(0,1)^{\mathsf{T}}$, and $m\mu_{\mathrm{fr}}/(m\rho_{\mathrm{a}} - \rho_{\mathrm{f}}^2)$, with eigenvector $(-m, \rho_{\mathrm{f}})^{\mathsf{T}}$.

For the upper left block we use the formulae in Section Appendix A.1. Firstly, let $Z_1 = \det(Q'_{\mathrm{LR}}) = \det(Q')$ (which is a common denominator for the coefficients of the characteristic polynomial) and define $Z_2, \ldots, Z_5$ as in Section Appendix A.1. Explicitly,

$$\begin{aligned}
Z_1 &= m\rho_{\mathrm{a}} - \rho_{\mathrm{f}}^2 \\
Z_2 &= (\rho_{\mathrm{a}} - 2\alpha\rho_{\mathrm{f}})M + m(2\mu_{\mathrm{fr}} + \lambda) \\
Z_3 &= \rho_{\mathrm{a}}(4\alpha^2 m - 4\alpha\rho_{\mathrm{f}} + \rho_{\mathrm{a}})M^2 - 2(2\alpha m\rho_{\mathrm{f}} + m\rho_{\mathrm{a}} - 2\rho_{\mathrm{f}}^2)M(2\mu_{\mathrm{fr}} + \lambda) + m^2(2\mu_{\mathrm{fr}} + \lambda)^2 \\
Z_4 &= \rho_{\mathrm{a}}M - m(2\mu_{\mathrm{fr}} + \lambda) \\
Z_5 &= 2(\alpha m - \rho_{\mathrm{f}})M.
\end{aligned}$$

In terms of these, the eigenvalues are

$$\frac{Z_2 \pm \sqrt{Z_3}}{2Z_1}$$

and the eigenvectors are

$$(Z_5, Z_4 \pm \sqrt{Z_3})^{\mathsf{T}}.$$

Now, following Section Appendix A.3, we can assemble the eigenvectors $y^{(1)}, y^{(2)}, y^{(3)}, y^{(4)}$ of $(Q'^{-1}A)_{\mathrm{LL}}(Q'^{-1}A')_{\mathrm{UR}}$ with eigenvalues

$$c_1^2 = \frac{Z_2 + \sqrt{Z_3}}{2Z_1}; \qquad c_2^2 = \frac{Z_2 - \sqrt{Z_3}}{2Z_1}; \qquad c_3^2 = \frac{m\mu_{\mathrm{fr}}}{Z_1}; \qquad c_4^2 = 0$$

as

$$\begin{aligned}
y^{(1)} &= (Z_5, Z_4 + \sqrt{Z_3}, 0, 0)^{\mathsf{T}} \\
y^{(2)} &= (Z_5, Z_4 - \sqrt{Z_3}, 0, 0)^{\mathsf{T}} \\
y^{(3)} &= (0, 0, -m, \rho_{\mathrm{f}})^{\mathsf{T}} \\
y^{(4)} &= (0, 0, 0, 1)^{\mathsf{T}}.
\end{aligned}$$

Following Section Appendix A.4, we calculate

$$x^{(j)} = (Q'^{-1}A')_{\mathrm{UR}}x^{(j)} \qquad (j = 1, 2, 3)$$

$$x^{(1)} = (-Z_5, 0, 0, Z_4 + \sqrt{Z_3})^{\mathsf{T}}$$
$$x^{(2)} = (-Z_5, 0, 0, Z_4 - \sqrt{Z_3})^{\mathsf{T}}$$
$$x^{(3)} = (0, 0, m/2, 0)^{\mathsf{T}}$$

and note that

$$x^{(4)} = (-M\alpha^2 + \lambda, M\alpha^2 - \lambda - 2\mu_{\mathrm{fr}}, 0, -2\alpha\mu_{\mathrm{fr}})^{\mathsf{T}}$$

is a null vector of $(Q'^{-1}A')_{\mathrm{UR}}(Q'^{-1}A')_{\mathrm{LL}}$. Still following Section Appendix A.4, we can now write down eigenvectors of $Q'^{-1}A'$ corresponding to $\pm c_j$ as $(x^{(j)}; \pm c_j y^{(j)})$ $(j = 1, 2, 3)$ and $(x^{(4)}; 0)$ and $(0; y^{(4)})$ corresponding to $\pm c_4 = 0$. Finally, to return to the original ordering of the physical variables, we need to swap entries 6 and 7 in each of these vectors to give eigenvectors of $Q^{-1}A$.

Appendix B.2. The low-frequency dissipative case

Here we have a similar problem, but with somewhat more complicated formulae. Let E be the 8×8 matrix that is zero in all places except $(7, 7)$ and $(8, 8)$, which hold the value $-\eta/k$. We now repeat the earlier analysis but with Q replaced by $Q - \mathrm{i}E/\omega$. We can see from the structure of Q, E and A that this is equivalent simply to changing m to $m + \mathrm{i}\eta/(k\omega)$ throughout the problem, and hence throughout the solution. This leads to the following modified values of $Z_1, \ldots, Z_5$:

$$\begin{aligned}
Z_1^{\mathrm{d}} &= (m + \mathrm{i}\eta/(k\omega))\rho_{\mathrm{a}} - \rho_{\mathrm{f}}^2 \\
&= Z_1 + \mathrm{i}\frac{\eta\rho_{\mathrm{a}}}{k\omega} \\
Z_2^{\mathrm{d}} &= -2\rho_{\mathrm{f}}\alpha M + \rho_{\mathrm{a}} M + (m + \mathrm{i}\eta/(k\omega))(2\mu_{\mathrm{fr}} + \lambda) \\
&= Z_2 + \mathrm{i}\frac{\eta(2\mu_{\mathrm{fr}} + \lambda)}{k\omega} \\
Z_3^{\mathrm{d}} &= \rho_{\mathrm{a}}(4\alpha^2(m + \mathrm{i}\eta/(k\omega)) - 4\alpha\rho_{\mathrm{f}} + \rho_{\mathrm{a}})M^2 - 2((2\alpha\rho_{\mathrm{f}} + \rho_{\mathrm{a}})(m + \mathrm{i}\eta/(k\omega)) - 2\rho_{\mathrm{f}}^2)M(2\mu_{\mathrm{fr}} + \lambda) + \\
&\qquad (m + \mathrm{i}\eta/(k\omega))^2(2\mu_{\mathrm{fr}} + \lambda)^2 \\
&= \left[Z_3 - \frac{\eta^2(2\mu_{\mathrm{fr}} + \lambda)^2}{k^2\omega^2}\right] + \mathrm{i}\frac{2\eta}{k\omega}\left[2\alpha^2\rho_{\mathrm{a}}M^2 - (2\alpha\rho_{\mathrm{f}} + \rho_{\mathrm{a}})M(2\mu_{\mathrm{fr}} + \lambda) + m(2\mu_{\mathrm{fr}} + \lambda)^2\right] \\
Z_4^{\mathrm{d}} &= \rho_{\mathrm{a}} M - (m + \mathrm{i}\eta/(k\omega))(2\mu_{\mathrm{fr}} + \lambda) \\
&= Z_4 - \mathrm{i}\frac{\eta(2\mu_{\mathrm{fr}} + \lambda)}{k\omega} \\
Z_5^{\mathrm{d}} &= 2(\alpha(m + \mathrm{i}\eta/(k\omega)) - \rho_{\mathrm{f}})M \\
&= Z_5 + \mathrm{i}\frac{2\alpha\eta M}{k\omega}.
\end{aligned}$$

Notice that, except for $j = 3$, Z_j is a linear function of m, so we have $\mathrm{Re}(Z_j^{\mathrm{d}}) = Z_j$. The eigenvalues of $(Q - \mathrm{i}E/\omega)^{-1}A$ are complex but still occur in $\pm$ pairs with the following squares:

$$(c_1^{\mathrm{d}})^2 = 0$$

$$(c_2^{\mathrm{d}})^2 = \frac{(m + \mathrm{i}\eta/(k\omega))\mu_{\mathrm{fr}}}{Z_1^{\mathrm{d}}}$$
$$(c_3^{\mathrm{d}})^2 = \frac{1}{2Z_1^{\mathrm{d}}}\left(Z_2^{\mathrm{d}} + \sqrt{Z_3^{\mathrm{d}}}\right)$$
$$(c_4^{\mathrm{d}})^2 = \frac{1}{2Z_1^{\mathrm{d}}}\left(Z_2^{\mathrm{d}} - \sqrt{Z_3^{\mathrm{d}}}\right).$$

The expressions for the eigenvalues contain many square roots of complex numbers. Care must be taken, especially in computer implementation, with the two branches of the complex square root function. One way to do this is to use the formula

$$\sqrt{z} = \frac{\sqrt{2}}{2}\left(\sqrt{|z| + \mathrm{Re}(z)} - \mathrm{i}\,\mathrm{csgn}(\mathrm{i}z)\sqrt{|z| - \mathrm{Re}(z)}\right) \qquad (z \in \mathbb{C}, z \neq 0).$$

Here, the square roots are non-negative square roots of non-negative real numbers and

$$\mathrm{csgn}(z) = \begin{cases} \mathrm{sgn}(\mathrm{Re}(z)) & \text{if } \mathrm{Re}(z) \neq 0 \\ \mathrm{sgn}(\mathrm{Im}(z)) & \text{if } \mathrm{Re}(z) = 0. \end{cases}$$

This 'complex sign' partitions the complex plane into left and right half-planes. The formula above returns the unique square root $\sqrt{z}$ of $z \neq 0$ such that $\mathrm{csgn}(\sqrt{z}) > 0$. In particular, if z is real and positive then $\sqrt{z}$ is the positive real square root of z; if z is real and negative, then $\sqrt{z}$ is a positive multiple of i. Alternatively, this can be constructed by removing the negative real axis from the complex plane, analytically continuing the non-negative real square root to the cut plane and finally extending to a function continuous from above on the negative real axis.

Appendix B.3. The high-frequency dissipative case

Here we must deal with 10×10 matrices, closely related to the 8×8 matrices in the earlier sections. We are concerned with

$$Q_{\mathrm{hf}} = \left(\begin{array}{cccc|cccccc} 1 & 0 & 0 & 0 & 0 & 0 & 0 & 0 & 0 & 0 \\ 0 & 1 & 0 & 0 & 0 & 0 & 0 & 0 & 0 & 0 \\ 0 & 0 & 1 & 0 & 0 & 0 & 0 & 0 & 0 & 0 \\ 0 & 0 & 0 & 1 & 0 & 0 & 0 & 0 & 0 & 0 \\ \hline 0 & 0 & 0 & 0 & \rho_{\mathrm{a}} & 0 & \rho_{\mathrm{f}} & 0 & 0 & 0 \\ 0 & 0 & 0 & 0 & 0 & \rho_{\mathrm{a}} & 0 & \rho_{\mathrm{f}} & 0 & 0 \\ 0 & 0 & 0 & 0 & \rho_{\mathrm{f}} & 0 & m & 0 & 0 & 0 \\ 0 & 0 & 0 & 0 & 0 & \rho_{\mathrm{f}} & 0 & m & 0 & 0 \\ 0 & 0 & 0 & 0 & 0 & 0 & \tau_\epsilon/\tau_\sigma - 1 & 0 & -1 & 0 \\ 0 & 0 & 0 & 0 & 0 & 0 & 0 & \tau_\epsilon/\tau_\sigma - 1 & 0 & -1 \end{array}\right)$$

and

$$A_{\mathrm{hf}} = \left(\begin{array}{cccc|cccccc} 0 & 0 & 0 & 0 & -1 & 0 & 0 & 0 & 0 & 0 \\ 0 & 0 & 0 & 0 & 0 & 0 & 0 & 0 & 0 & 0 \\ 0 & 0 & 0 & 0 & 0 & -1/2 & 0 & 0 & 0 & 0 \\ 0 & 0 & 0 & 0 & 0 & 0 & 1 & 0 & 0 & 0 \\ \hline -\lambda - 2\mu_{\mathrm{fr}} & -\lambda & 0 & M\alpha & 0 & 0 & 0 & 0 & 0 & 0 \\ 0 & 0 & -2\mu_{\mathrm{fr}} & 0 & 0 & 0 & 0 & 0 & 0 & 0 \\ -M\alpha & -M\alpha & 0 & M & 0 & 0 & 0 & 0 & 0 & 0 \\ 0 & 0 & 0 & 0 & 0 & 0 & 0 & 0 & 0 & 0 \\ 0 & 0 & 0 & 0 & 0 & 0 & 0 & 0 & 0 & 0 \\ 0 & 0 & 0 & 0 & 0 & 0 & 0 & 0 & 0 & 0 \end{array}\right).$$

We also introduce the 10×10 matrix E_{hf} whose bottom right 4×4 submatrix is

$$\begin{pmatrix} -\eta/k & 0 & -\eta/k & 0 \\ 0 & -\eta/k & 0 & -\eta/k \\ 0 & 0 & 1/\tau_\sigma & 0 \\ 0 & 0 & 0 & 1/\tau_\sigma \end{pmatrix}$$

and which is zero in all other places. We seek the eigenvalues of $(Q_{\mathrm{hf}} - (\mathrm{i}/\omega)E_{\mathrm{hf}})^{-1}A_{\mathrm{hf}}$ and begin by considering

$$Q_{\mathrm{hf}} - (\mathrm{i}/\omega)E_{\mathrm{hf}} = \left(\begin{array}{cccc|cc|cccc} 1 & 0 & 0 & 0 & 0 & 0 & 0 & 0 & 0 & 0 \\ 0 & 1 & 0 & 0 & 0 & 0 & 0 & 0 & 0 & 0 \\ 0 & 0 & 1 & 0 & 0 & 0 & 0 & 0 & 0 & 0 \\ 0 & 0 & 0 & 1 & 0 & 0 & 0 & 0 & 0 & 0 \\ \hline 0 & 0 & 0 & 0 & \rho_{\mathrm{a}} & 0 & \rho_{\mathrm{f}} & 0 & 0 & 0 \\ 0 & 0 & 0 & 0 & 0 & \rho_{\mathrm{a}} & 0 & \rho_{\mathrm{f}} & 0 & 0 \\ 0 & 0 & 0 & 0 & \rho_{\mathrm{f}} & 0 & m + \mathrm{i}\eta/(\omega k) & 0 & \mathrm{i}\eta/(\omega k) & 0 \\ 0 & 0 & 0 & 0 & 0 & \rho_{\mathrm{f}} & 0 & m + \mathrm{i}\eta/(\omega k) & 0 & \mathrm{i}\eta/(\omega k) \\ 0 & 0 & 0 & 0 & 0 & 0 & \frac{\tau_\epsilon}{\tau_\sigma} - 1 & 0 & -1 - \mathrm{i}/(\omega\tau_\sigma) & 0 \\ 0 & 0 & 0 & 0 & 0 & 0 & 0 & \tau_\epsilon/\tau_\sigma - 1 & 0 & -1 - \mathrm{i}/(\omega\tau_\sigma) \end{array}\right).$$

As illustrated, we have a natural $4 + 6$ block structure. As in the low-frequency case, we can find a finer structure by permuting the variables to group terms by dimension instead of medium (this is evident from the chessboard pattern of zero and non-zero terms in the lower right 6×6 block). We make the following permutation of rows and columns to give Q'_{hf}, E'_{hf} and A'_{hf}:

$$\begin{pmatrix} 5 & 6 & 7 & 8 & 9 & 10 \\ 5 & 7 & 9 & 6 & 8 & 10 \end{pmatrix}$$

which leads to a block decomposition

$$Q'_{\mathrm{hf}} - (\mathrm{i}/\omega)E'_{\mathrm{hf}} = \left(\begin{array}{c|c|c} I & 0 & 0 \\ \hline 0 & C_0 & 0 \\ \hline 0 & 0 & C_0 \end{array}\right)$$

where I is the 4×4 identity matrix and C_0 is the 3×3 block

$$\begin{pmatrix} \rho_{\mathrm{a}} & \rho_{\mathrm{f}} & 0 \\ \rho_{\mathrm{f}} & m + \mathrm{i}\eta/(\omega k) & \mathrm{i}\eta/(\omega k) \\ 0 & \tau_\epsilon/\tau_\sigma - 1 & -1 - \mathrm{i}/(\omega\tau_\sigma) \end{pmatrix}.$$

The corresponding refined block structure on A'_{hf} is

$$A'_{\mathrm{hf}} = \left(\begin{array}{cccc|ccc|ccc} 0 & 0 & 0 & 0 & -1 & 0 & 0 & 0 & 0 & 0 \\ 0 & 0 & 0 & 0 & 0 & 0 & 0 & 0 & 0 & 0 \\ 0 & 0 & 0 & 0 & 0 & 0 & 0 & -1/2 & 0 & 0 \\ 0 & 0 & 0 & 0 & 0 & 1 & 0 & 0 & 0 & 0 \\ \hline -\lambda - 2\mu_{\mathrm{fr}} & -\lambda & 0 & M\alpha & 0 & 0 & 0 & 0 & 0 & 0 \\ -M\alpha & -M\alpha & 0 & M & 0 & 0 & 0 & 0 & 0 & 0 \\ 0 & 0 & 0 & 0 & 0 & 0 & 0 & 0 & 0 & 0 \\ \hline 0 & 0 & -2\mu_{\mathrm{fr}} & 0 & 0 & 0 & 0 & 0 & 0 & 0 \\ 0 & 0 & 0 & 0 & 0 & 0 & 0 & 0 & 0 & 0 \\ 0 & 0 & 0 & 0 & 0 & 0 & 0 & 0 & 0 & 0 \end{array}\right).$$

Because of the block diagonal structure of $Q'_{\mathrm{hf}} - (\mathrm{i}/\omega)E'_{\mathrm{hf}}$, we can find $(Q'_{\mathrm{hf}} - (\mathrm{i}/\omega)E'_{\mathrm{hf}})^{-1}A'_{\mathrm{hf}}$ by multiplying the second and third block rows of A by C_0^{-1}; the first row of $(Q'_{\mathrm{hf}} - (\mathrm{i}/\omega)E'_{\mathrm{hf}})^{-1}A'_{\mathrm{hf}}$ is the the same as that of A'_{hf}. We can see from this that $(Q'_{\mathrm{hf}} - (\mathrm{i}/\omega)E'_{\mathrm{hf}})^{-1}A'_{\mathrm{hf}}$ has a $4+6$ antidiagonal block decomposition. Following Section Appendix A.4, we need to consider the product of the lower left and upper right blocks. By associativity of matrix multiplication and because of the diagonal structure of $(Q'_{\mathrm{hf}} - (\mathrm{i}/\omega)E'_{\mathrm{hf}})^{-1}$, we can first find $(A'_{\mathrm{hf}})_{\mathrm{LL}}(A'_{\mathrm{hf}})_{\mathrm{UR}}$ and then multiply the top and bottom 3×6 blocks by C_0^{-1} (which is somewhat simpler because of the prevalence of zero terms in A'_{hf}). We have

$$(A'_{\mathrm{hf}})_{\mathrm{LL}}(A'_{\mathrm{hf}})_{\mathrm{UR}} = \left(\begin{array}{ccc|ccc} \lambda + 2\mu_{\mathrm{fr}} & M\alpha & 0 & 0 & 0 & 0 \\ M\alpha & M & 0 & 0 & 0 & 0 \\ 0 & 0 & 0 & 0 & 0 & 0 \\ \hline 0 & 0 & 0 & \mu_{\mathrm{fr}} & 0 & 0 \\ 0 & 0 & 0 & 0 & 0 & 0 \\ 0 & 0 & 0 & 0 & 0 & 0 \end{array}\right).$$

This is block diagonal, so when we multiply its top and bottom block rows by C_0^{-1}, we obtain another block diagonal matrix whose eigenstructure is determined by its two diagonal blocks, namely

$$C_1 = \begin{pmatrix} \rho_\mathrm{a} & \rho_\mathrm{f} & 0 \\ \rho_\mathrm{f} & m + \mathrm{i}\eta/(\omega k) & \mathrm{i}\eta/(\omega k) \\ 0 & \tau_\epsilon/\tau_\sigma - 1 & -1 - \mathrm{i}/(\omega\tau_\sigma) \end{pmatrix}^{-1} \begin{pmatrix} \lambda + 2\mu_\mathrm{fr} & M\alpha & 0 \\ M\alpha & M & 0 \\ 0 & 0 & 0 \end{pmatrix}$$

and

$$C_2 = \begin{pmatrix} \rho_\mathrm{a} & \rho_\mathrm{f} & 0 \\ \rho_\mathrm{f} & m + \mathrm{i}\eta/(\omega k) & \mathrm{i}\eta/(\omega k) \\ 0 & \tau_\epsilon/\tau_\sigma - 1 & -1 - \mathrm{i}/(\omega\tau_\sigma) \end{pmatrix}^{-1} \begin{pmatrix} \mu_\mathrm{fr} & 0 & 0 \\ 0 & 0 & 0 \\ 0 & 0 & 0 \end{pmatrix}.$$

The non-zero eigenvalues of $(Q_\mathrm{hf} - (\mathrm{i}/\omega)E_\mathrm{hf})^{-1}A_\mathrm{hf}$ are exactly the square roots of the non-zero eigenvalues of C_1 and of C_2.

Notice that the right-hand column of C_1 is zero. We can think of this as a $2+1$ block upper triangular matrix: one of its eigenvalues is zero, from the zero lower right 1×1 block, and the other two are eigenvalues of the upper left 2×2 block of C_1.

Similarly, the second and third columns of C_2 are zero, and we can think of this as a $1+2$ block lower triangular matrix with two zero eigenvalues from the zero lower right 1×1 block and one other eigenvalue, which is just the upper left entry of C_2.

This gives us an eigenvalue

$$\frac{\mu_\mathrm{fr}\left(\eta - km\omega^2\tau_\sigma - \mathrm{i}\omega\left(\eta\tau_\epsilon + km\right)\right)}{\eta\rho_\mathrm{a} - km\omega^2\rho_\mathrm{a}\tau_\sigma + k\omega^2\rho_\mathrm{f}^2\tau_\sigma - \mathrm{i}\omega\left(\eta\rho_\mathrm{a}\tau_\epsilon + km\rho_\mathrm{a} - k\rho_\mathrm{f}^2\right)}$$

and a 2×2 block too long to fit on the page: it consists of a factor

$$\frac{1}{\eta\rho_\mathrm{a} - km\omega^2\rho_\mathrm{a}\tau_\sigma + k\omega^2\rho_\mathrm{f}^2\tau_\sigma - \mathrm{i}\omega\left(\eta\rho_\mathrm{a}\tau_\epsilon + km\rho_\mathrm{a} - k\rho_\mathrm{f}^2\right)}$$

multiplied by two columns:

$$\begin{pmatrix} M\alpha k\omega^2\rho_\mathrm{f}\tau_\sigma + \left(\eta - km\omega^2\tau_\sigma\right)\left(\lambda + 2\mu_\mathrm{fr}\right) + \mathrm{i}\left(M\alpha k\omega\rho_\mathrm{f} - \omega\left(\lambda + 2\mu_\mathrm{fr}\right)\left(\eta\tau_\epsilon + km\right)\right) \\ k\omega\left(-M\alpha\omega\rho_\mathrm{a}\tau_\sigma + \omega\rho_\mathrm{f}\tau_\sigma\left(\lambda + 2\mu_\mathrm{fr}\right)\right) + \mathrm{i}k\omega\left(-M\alpha\rho_\mathrm{a} + \rho_\mathrm{f}\left(\lambda + 2\mu_\mathrm{fr}\right)\right) \end{pmatrix}$$

and

$$\begin{pmatrix} M\left(\alpha\eta - \alpha km\omega^2\tau_\sigma + k\omega^2\rho_\mathrm{f}\tau_\sigma\right) - \mathrm{i}M\omega\left(\alpha\eta\tau_\epsilon + \alpha km - k\rho_\mathrm{f}\right) \\ Mk\omega^2\tau_\sigma\left(\alpha\rho_\mathrm{f} - \rho_\mathrm{a}\right) + \mathrm{i}Mk\omega\left(\alpha\rho_\mathrm{f} - \rho_\mathrm{a}\right) \end{pmatrix}$$

and its eigenvalues can be found using the formulae in Section Appendix A.1.

References

[1] R. Dann, M. Close, L.Pang, M. Flintoft, R. Hector, Complementary use of tracer and pumping tests to characterize a heterogenous channelized aquifer system in New Zealand, Hydrogeol. J. 16 (2008) 1177–1191.

[2] I. Haycock, Personal communication, 2015. McMillan Drilling Group.

[3] T. Cui, N. D. Ward, J. Kaipio, Characterisation of parameters for a spatially heterogenous aquifer from pumping test data, J. Hydrol. Eng. 19 (2014) 1203–1213.

[4] T. Cui, N. D. Ward, S. Eveson, T. Lähivaara, Pragmatic approach to calibrating distributed parameter groundwater models from pumping test data using adaptive delayed acceptance MCMC, J. Hydrol. Eng. 21 (2016) 06015011.

[5] A. Gulley, N. D. Ward, S. Cox, J. Kaipio, Groundwater responses to the recent Canterbury earthquakes: a comparison, J. Hydrol. 504 (2013) 171–181.

[6] N. Dudley Ward, On the mechanism of earthquake induced groundwater flow, J. Hydrol. 530 (2015) 561–567.

[7] M. Biot, Theory of propagation of elastic waves in a fluid saturated porous solid. I. Low frequency range, J. Acoust. Soc. Am. 28 (1956) 168–178.

[8] M. Biot, Theory of propagation of elastic waves in a fluid saturated porous solid. II. Higher frequency range, J. Acoust. Soc. Am. 28 (1956) 179–191.

[9] T. Lähivaara, N. Dudley Ward, T. Huttunen, J. Koponen, J. Kaipio, Estimation of aquifer dimensions from passive seismic signals with approximate wave propagation models, Inverse Problems 30 (2014) 015003.

[10] T. Lähivaara, N. Dudley Ward, T. Huttunen, Z. Rawlinson, J. Kaipio, Estimation of aquifer dimensions from passive seismic signals in the presence of material and source uncertainties, Geophys. J. Int. 200 (2015) 1662–1675.

[11] C. Morency, J. Tromp, Spectral-element simulations of wave propagation in porous media, Geophys. J. Int. 175 (2008) 301–345.

[12] J. Carcione, C. Morency, J. Santos, Computational poroelasticity - A review, Geophysics 75 (2010) 229–243.

[13] G. Lemoine, M. Yvonne Ou, R. LeVeque, High-resolution finite volume modeling of wave propagation in orthotropic poroelastic media, SIAM J. Sci. Comput 35 (2013) B176–B206.

[14] J. de la Puente, Seismic Wave Simulation for Complex Rheologies on Unstructured Meshes, Ph.D. thesis, Ludwig-Maximilians-Universität München, 2008.

[15] J. de la Puente, M. Dumbser, M. Käser, H. Igel, Discontinuous Galerkin methods for wave propagation in poroelastic media, Geophysics 73 (2008) T77–T97.

[16] G. Gabard, O. Dazel, A discontinuous Galerkin method with plane waves for sound-absorbing materials, Int. J. Numer. Meth. Eng. 104 (2015) 1115–1138.

[17] L. Wilcox, G. Stadler, C. Burstedde, O. Ghattas, A high-order discontinuous Galerkin method for wave propagation through coupled elastic-acoustic media, J. Comput. Phys. 229 (2010) 9373–9396.

[18] M. Käser, M. Dumbser, A highly accurate discontinuous Galerkin method for complex interfaces between solids and moving fluids, Geophysics 73 (2008) T23–T35.

[19] G. Lemoine, M. Yvonne Ou, Finite volume modeling of poroelastic-fluid wave propagation with mapped grids, SIAM J. Sci. Compu.t 36 (2014) B396–B426.

[20] G. Lemoine, Three-dimensional mapped-grid finite volume modeling of poroelastic-fluid wave propagation, SIAM J. Sci. Comput. 38 (2016) B808–B836.

[21] W. Reed, T. Hill, Triangular mesh methods for the neutron transport equation, Technical report, Los Alamos National Laboratory, USA, 1973.

[22] P. LeSaint, P. Raviart, On a finite element method for solving the neutron transport equation, in: Mathematical Aspects of Finite Element Methods in Partial Differential Equations, Academic Press, New York, 1974, pp. 89–123.

[23] C. Johnson, J. Pitkäranta, An analysis of the discontinuous Galerkin method for a scalar hyperbolic equation, Math. Comput. 46 (1986) 1–26.

[24] G. Richter, An optimal-order error estimate for the discontinuous Galerkin method, Math. Comput. 50 (1988) 75–88.

[25] F. Hu, M. Hussaini, P. Rasetarinera, An analysis of the discontinuous Galerkin method for wave propagation problems, J. Comput. Phys. 151 (1999) 921–946.

[26] M. Ainsworth, Dispersive and dissipative behaviour of high order discontinuous Galerkin finite element methods, J. Comput. Phys. 198 (2004) 106–130.

[27] M. Ainsworth, P. Monk, W. Muniz, Dispersive and dissipative properties of the discontinuous Galerkin finite element methods for second-order wave equation, J. Sci. Comput. 27 (2006) 5–40.

[28] J. Hesthaven, T. Warburton, Nodal high-order methods on unstructured grids I. Time-domain solution of Maxwell's equations, J. Comput. Phys. 181 (2002) 186–221.

[29] B. Cockburn, F. Li, C.-W. Shu, Locally divergence-free discontinuous Galerkin methods for the Maxwell equations, J. Comput. Phys. 194 (2004) 588–610.

[30] M. Käser, M. Dumbser, An arbitrary high-order discontinuous Galerkin method for elastic waves on unstructured meshes - I. The two-dimensional isotropic case with external source terms, Geophys. J. Int. 166 (2006) 855–877.

[31] H. Egger, F. Kretzschmar, S. Schnepp, T. Weiland, A space-time discontinuous Galerkin Trefftz method for time dependent Maxwell's equations, SIAM J. Sci. Comput. 37 (2015) B689–B711.

[32] M. Dumbser, M. Käser, An arbitrary high-order discontinuous Galerkin method for elastic waves on unstructured meshes - II. The three-dimensional isotropic case, Geophys. J. Int. 167 (2006) 319–336.

[33] P. Monk, G. Richter, A discontinuous Galerkin method for linear symmetric hyperbolic systems in inhomogeneous media, J. Sci. Comput. 22-23 (2005) 443–477.

[34] J. Hesthaven, T. Warburton, Nodal Discontinuous Galerkin Methods: Algorithms, Analysis, and Applications, Springer, 2007.

[35] R. Leveque, Finite Volume Method for Hyperbolic Problems, Cambridge University Press, 2002.

[36] M. Carpenter, C. Kennedy, Fourth-order 2N-storage Runge-Kutta schemes, Technical report, NASA-TM-109112, 1994.

[37] S. Petersen, C. Farhat, R. Tezaur, A space-time discontinuous Galerkin method for the solution of the wave equation in the time domain, Int. J. Numer. Meth. Eng. 78 (2009) 275–295.

[38] E. Toro, R. Millington, L. Nejad, Towards very high order Godunov schemes, in: E. Toro (Ed.), Godunov Methods: Theory and Applications, Kluwer Academic Publishers, 2001.

[39] V. Titarev, E. Toro, ADER: Arbitrary high order Godunov approach, J. Sci. Comput. 17 (2002) 609–618.

[40] T. Schwartzkopff, C. Munz, E. Toro, ADER: A high-order approach for linear hyperbolic systems in 2D, J. Sci. Comput. 17 (2002) 231–240.

[41] A. Taube, M. Dumbser, C.-D. Munz, R. Schneider, A high-order discontinuous Galerkin method with time-accurate local time stepping for the Maxwell equations, International Journal of Numerical Modelling: Electronic Networks, Devices and Fields 22 (2009) 77–103.

[42] B. Cockburn, G. Karniadakis, C.-W. Shu (Eds.), Discontinuous Galerkin Methods Theory, Computation and Applications, Springer, 2000.

[43] J. Carcione, Wave Fields in Real Media: Wave propagation in anisotropic, anelastic and porous media, Elsevier, 2015.

[44] M. Biot, D. Willis, The elastic coefficients of the theory of consolidation, J. Appl. Mech. 24 (1957) 594–601.

[45] M. Biot, Mechanics of deformation and acoustic propagation in porous media, J. Appl. Phys. 33 (1962) 1482–1498.

[46] M. Biot, Generalized theory of acoustic propagation in porous dissipative media, J. Acoust. Soc. Am. 34 (1962) 1254–1264.

[47] J. Carcione, G. Quiroga-Goode, Some aspects of the physics and numerical modeling of Biot compressional waves, J. Comput. Acoust. 3 (1995) 261–280.

[48] C. Kennedy, M. Carpenter, Additive Runge-Kutta schemes for convection-diffusion-reaction equations, Appl. Numer. Math. 44 (2003) 139–181.

[49] A. Kanevsky, M. Carpenter, D. Gottlieb, J. Hesthaven, Application of implicit-explicit high order Runge-Kutta methods to discontinuous-Galerkin schemes, J. Comput. Phys. 225 (2007) 1753–1781.

[50] P. Cazeaux, J. Hesthaven, Multiscale modelling of sound propagation through the lung parenchyma, ESAIM: M2AN 48 (2014) 27–52.

[51] L. Pareschi, G. Russo, Implicit-explicit Runge-Kutta schemes and applications to hyperbolic systems with relaxation, J. Sci. Comput. 25 (2005) 129–155.

[52] S. Boscarino, L. Pareschi, G. Russo, Implicit-explicit Runge-Kutta schemes for hyperbolic systems and kinetic equations in the diffusion limit, SIAM J. Sci. Comput. 35 (2013) A22–A51.

[53] D. Cavaglieri, T. Bewley, Low-storage implicit/explicit Runge-Kutta schemes for the simulation of stiff high-dimensional ODE systems, J. Comput. Phys. 286 (2015) 172–193.

[54] A. Patera, A spectral element method for fluid dynamics - Laminar flow in a channel expansion, J. Comput. Phys. 54 (1984) 468–488.

[55] D. Komatitsch, J. Vilotte, The spectral-element method: an efficient tool to simulate the seismic response of 2D and 3D geological structures, Bull. Seismol. Soc. Am. 88 (1998) 368–392.

[56] J. Diaz, A. Ezziani, Analytical solution for wave propagation in stratified poroelastic medium. Part I: the 2D case, Technical Report, INRIA, 2008.

[57] T. Lähivaara, T. Huttunen, A non-uniform basis order for the discontinuous Galerkin method of the acoustic and elastic wave equations, Appl. Numer. Math. 61 (2011) 473–486.

[58] T. Lähivaara, T. Huttunen, A non-uniform basis order for the discontinuous Galerkin method of the 3D dissipative wave equation with perfectly matched layer, J. Comput. Phys. 229 (2010) 5144–5160.

[59] J. Kaipio, V. Kolehmainen, M. Vauhkonen, E. Somersalo, Inverse problems with structural prior information, Inverse Problems 15 (1999) 713.

[60] J. Kaipio, E. Somersalo, Statistical and Computational Inverse Problems, Springer-Verlag, 2005.

[61] A. Adamczyk, M. Malinowski, A. Malehmir, High-resolution near-surface velocity model building using full-waveform inversion - a case study from southwest Sweden, Geophys. J. Int. (2014).

[62] M. Giustiniani, F. Accaino, S. Picotti, U. Tinivella, 3D seismic data for shallow aquifers characterisation, J. Appl. Geophys. 68 (2009) 394–403.

[63] J. Bear, Hydraulics of Groundwater, Dover, 1979.

[64] J. Rubino, C. Ravazzoli, J. Santos, Equivalent viscoelastic solids for heterogeneous fluid-saturated porous rocks, Geophysics 74 (2009) N1–N13.

[65] N. Dudley Ward, J. Kaipio, Uncertainty, decision and control: issues and solutions, New Zealand Journal of Hydrology 53 (2014) 53–91.